Delft University of Technology | Faculty of Aerospace Engineering

Characterisation of the Dicke-Switch Chopper System and AGPM Coronagraph for the NEAR Experiment at the ESO-VLT

Serban Leveratto

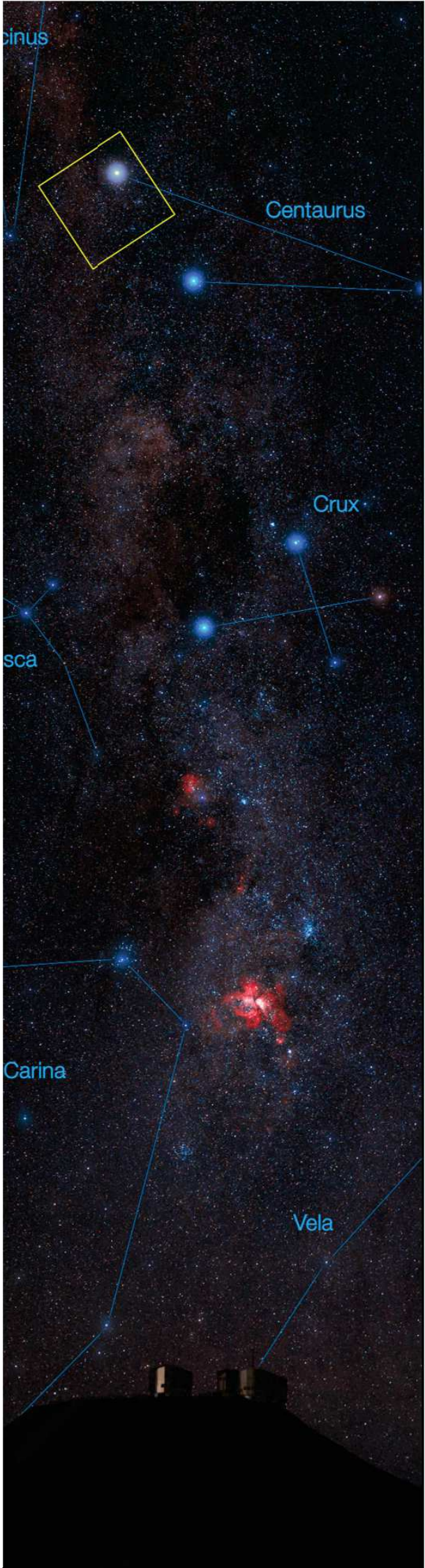

TU Delft

Characterisation of the Dicke-Switch Chopper System and AGPM Coronagraph for the NEAR Experiment at the ESO-VLT

by

Serban Leveratto

to obtain the degree of Master of Science

at the Delft University of Technology,

to be defended publicly on Monday December 17, 2018 at 11:00 AM.

Student number:	4632508	
Project duration:	May 2, 2018 – December 17, 2018	
Thesis committee:	Prof. dr. B. R. Brandl,	TU Delft, supervisor
	Ir. G. Jakob	ESO, supervisor
	Dr. ir. J. M. Kuiper,	TU Delft, supervisor
	Dr. S. M. Cazaux	TU Delft

An electronic version of this thesis is available at `http://repository.tudelft.nl/`.

Cover photo is adapted from *The Alpha Centauri star system*, PR Image eso1702b, courtesy of ESO

TU Delft

Acknowledgements

This thesis report concludes my Master in Space Engineering at the Delft University of Technology. The last two years have been absolutely fantastic. Besides learning many things about space engineering, I was also able to meet and work with people coming from literally all over the world. It is also thank to many of them if I am about to finish my studies.

First of all, I would like to thank Bernhard Brandl, my main supervisor at TU Delft, for introducing me to the NEAR projet and for his constant guidance. I also would like to thank Stéphanie Cazaux for the feedbacks provided during the main review meetings of the thesis.

I also would like to express my deepest gratitude to all the members of the NEAR team, in particular Gerd Jakob, Ulli Kaeufl, Markus Kasper and Robin Arsenault for giving me the possibility to join this project and for their constant support. I am really looking forward to the next phase of NEAR.

Furthermore, I would like to thank my colleagues and friends from Delft for the great time spent together. Last but not least, I would like to thank my family and friends from home, who constantly supported me, even from distance.

Serban Leveratto
Garching bei Muenchen, December 2018

Abstract

As part of the New Earths in the Alpha Cen Region (NEAR) experiment, VISIR, an imager and spectrometer for the mid-infrared at the Very Large Telescope (VLT) of the European Southern Observatory, will be soon upgraded to improve its performance in terms of high contrast and sensitivity for the detection of Earth-like planets in the Alpha Centauri star system, the closest to the Sun. Part of the VISIR upgrade consists in a novel chopper system based on the Dicke-switch concept to suppress the excess low frequency noise (ELFN) suffered by the detector array. The ELFN is a form of temporally correlated noise and can be mitigated by modulating the incident light at high enough frequency. The other main challenge of the NEAR experiment is the need of high contrast to image the circumstellar environment, and it will be achieved with the implementation of an annular groove phase mask (AGPM) coronagraph for the suppression of the starlight.

The main goals of the thesis project were the validation of the Dicke-switch chopper systems to assess its ability to mitigate background level and ELFN, and the characterisation of the performance of the AGPM coronagraph in terms of null depth and contrast level.

The first part of the laboratory characterisation of the Dicke-switch chopper system focused on the verification of the radiometric flux level achievable by its internal blackbody unit and by the so called artificial sky, a cold blackbody needed to reproduce the background level typical at the VLT, where the combined sky and telescope thermal radiation is the same as the one of a greybody at $280\,K$ and 10% emissivity. After the completion of the radiometric tests and mitigation of parasitic light effects caused by reflection of internal and external thermal radiation, the tests to validate the ability of the Dicke-switch chopper system to remove background level and suppress the ELFN started. The obtained results confirm that the Dicke-switch chopper system mitigate the ELFN as done also with pseudo-chopping, with reduction in noise $> 50\%$ when the chop frequency increases from $\sim 1\,Hz$ to $\sim 10\,Hz$. This was verified also for large offsets between the flux level of internal blackbody unit and artificial sky, up to at least $\sim 1600\,ADU$.

Similarly, the characterisation of the AGPM coronagraph started with the preparation of the laboratory setup, in particular design of the optical setup, alignment of all the optical components and measurement of the optical quality of the system to limit residual aberrations and vignetting. The results of the coronagraphic tests revealed that the two candidate AGPMs for the NEAR campaign, both optimised for wavelengths between 10 and 12.5 μm, are not able to provide the required contrasts level of 10^{-5} at $3\lambda/D$ and null depth of 10^{-3}. On the contrary, an older AGPM, spare part of the one currently mounted in VISIR, and thus optimised for wavelengths between 11 and 13.1 $\mu\,m$, provided better coronagraphic performance, and even though it is still not compliant with the requirements, at present it represents the baseline for the NEAR experiment.

Contents

List of Figures xi

List of Tables xvii

List of Abbreviations xix

Preface xxi

1 Introduction 1

2 NEAR experiment: scientific drivers and technical challenges 3

2.1 Scientific drivers for exoplanet exploration . . . 3

2.1.1 Overview on the Alpha Centauri region . . . 4

2.2 Observations in the MIR spectral regime . . . 5

2.2.1 Main challenges for the NEAR experiment . . . 6

2.3 Design description of the VISIR flange module . . . 8

2.3.1 Wave front sensor unit . . . 9

2.3.2 Calibration unit . . . 9

2.4 TIMMI2: the MIR detector test facility . . . 9

3 Characterisation of the Dicke-switch chopper system to mitigate the ELFN: laboratory tests and results 11

3.1 Limited sensitivity of the AQUARIUS detector . . . 11

3.1.1 Physical structure of IBC photodetectors . . . 11

3.1.2 Characteristics of the ELFN . . . 13

3.1.3 ELFN of the AQUARIUS detector . . . 14

3.2 Mitigation of the ELFN . . . 15

3.2.1 Chopping and nodding . . . 15

3.2.2 Chopping with the secondary mirror . . . 17

3.2.3 Dicke-switch concept . . . 18

3.3 Description of the VOU design. 19
3.3.1 Vacuum housing 20
3.3.2 Chopper mechanism 20
3.3.3 Blackbody unit 21
3.4 Overview on the upgrade of TIMMI2 to include the thermo-mechanical interface for the VOU. 22
3.5 Radiometric tests for the characterisation of internal blackbody unit and artificial sky . . 25
3.5.1 Background radiance and radiometric requirement 26
3.5.2 Artificial sky flux level 26
3.5.3 Parasitic light caused by reflections of internal and external thermal radiation . . . 30
3.5.4 Internal blackbody flux level 32
3.5.5 Internal blackbody uniformity 35
3.5.6 Overall radiometric flux level 35
3.6 Synchronisation of VOU and detector readout controller to perform ELFN noise measurements in chopping mode 36
3.7 Test methodologies for the ELFN measurements 37
3.8 Test results of the ELFN measurements. 38

4 Characterisation of the AGPM for high contrast imaging: laboratory tests and results 41

4.1 AGPM coronagraph: theoretical background, working principle and manufacturing 41
4.2 Laboratory setup for the coronographic measurements 44
4.2.1 Alignment of the optical setup using optical light 46
4.2.2 Verification of the alignment with the IR beam 52
4.3 Alignment of AGPM coronagraph and Lyot stop 55
4.4 Test methodologies for the coronagraphic measurements 57
4.4.1 Measurements of null depth and contrast profile 58
4.4.2 Measurements of the transmission 59
4.5 Data analysis 59
4.5.1 Background substraction and determination of the PSF's centre 59
4.5.2 Null depth. 59
4.5.3 Contrast profile 59
4.5.4 Off-axis transmission and stability of the CO_2 laser intensity 60

4.6 Results of the tests for the coronagraphic measurements 60
4.6.1 Overall results of the transmission measurements 60
4.6.2 Results of the coronagraphic measurements 61

5 Summary and conclusions of the results of the laboratory tests 67

5.1 Conclusions on the validation of the Dicke-switch chopper system 67
5.1.1 Future tests with the Dicke-switch chopper system 68
5.2 Conclusions on the characterisation of the AGPM coronagraphs 68
5.2.1 Future work on the laboratory setup for the coronagraphic measurements 69

Bibliography 71

List of Figures

2.1 Number of discovered exoplanets for each year from 1989 to 2018 grouped depending on the detection method used. . . . 4

2.2 Distribution of exoplanets with respect to their orbital period and mass grouped depending on the detection method used. . . . 4

2.3 Planetary-star flux ratio in the N-band regime for Eart-like planets located within 10 pc. The size of the dots indicates the apparent brightness of the planet, while the colours resembles the ones of the parent stars. . . . 5

2.4 Simulation of the sky background level using the ESO SKYCALC Sky Model Calculator and telescope contribution to the background level (mirrors at 280 K and combined emissivity of 0.07). . . . 5

2.5 Schematisation of a typical AO concept for the real time correction of atmospheric fluctuations. . . . 7

2.6 Complete assembly of the VFM. . . . 8

2.7 Cross-sectional view of VISIR. . . . 8

2.8 TIMMI2 optical layout. . . . 9

2.9 TIMMI2 cryostat and entrance window. . . . 9

3.1 *a)* Cross-sectional schematisation of the structure of a back-illuminated IBC detector, where the upper metallised region is the contact for a pixel *b)* Application of the detector bias voltage for the collection of photogenerated free electrons *c)* Electric field and extension of the depleted region. . . . 12

3.2 Variation of the ELFN as a function of the detector bias. . . . 13

3.3 Variation of the ELFN as a function of the the flux level impinging on the detector. . . . 13

3.4 Variation of the noise in the AQUARIUS detector as a function of the chop frequency for different flux levels, derived with pseudo-chopping from frames recorded in burst mode. 14

3.5 Variation of the noise in the AQUARIUS detector as a function of the total number of co-added frames for high and low flux levels. . . . 15

3.6 Schematisation of chopping and nodding for background removal in MIR observations. Both the angles of chopping and nodding are exaggerated for a better understanding of the diagram. . . . 16

3.7 Variation of the AQUARIUS detector sensitivity as a function of the chop frequency of the secondary mirror at the UT3. . . . 17

3.8 Laboratory test set-up used to assess the ability of the Dicke-switch chopper system to mitigate the ELFN of the AQUARIUS detector during the phase-A analysis. . . . 18

3.9 Results of the test performed during the phase-A analysis to assess the effectiveness of the ELFN mitigation with the Dicke-switch chopper system, derived with pseudo-chopping from frames recorded in burst mode. 18

3.10 Internal details of the VOU assembly. The vacuum housing hosts the Dicke-switch chopper system, which comprises a D-shape rotating mirror and the BBU for the suppression of background level and ELFN. The ZnSe dichroic window, coated to transmit between 10 and 12.5 μm, reflects light at optical wavelength towards the WFS for real-time correction of atmospheric fluctuations with AO. When the D-shape mirror is in open position, the beam coming from the telescope is able to reach the detector, while in the closed position the detector receives the signal from the BBU, whose temperature is regulated so that its radiation matches the background level typical at Paranal. 19

3.11 Exploded view of the vacuum housing. 20

3.12 Detailed view of the D-shape chopper mirror and of the mechanism for its actuation. . . 21

3.13 Section of the top view of the BBU assembly. The copper thermal straps are connected to the $\sim 40\,K$ cold shield of VISIR to cool the BBU down to $\sim 128\,K$. 22

3.14 Blackbody unit assembly. The copper thermal straps are connected to the $\sim 40\,K$ cold shield of VISIR to cool the BBU down to $\sim 128\,K$. 22

3.15 CAD model of the VOU integrated on the front flange of TIMMI2. The three-quarter section view shows the details of the different components and subsystems. The CAD models of the VOU assembly were realised by Kampf Telescope Optics GmbH (KTO), contractor responsible for the design of the VFM. 23

3.16 VOU during the integration on TIMMI2. 24

3.17 CAD model of the VOU integrated on the front flange of TIMMI2. This cross section highlights the fact that the imaging plane of the D-shape mirror is defocused with respect to the cold focal plane of TIMMI2. The CAD models of the VOU assembly were realised by KTO, contractor responsible for the design of the VFM. 25

3.18 Spectral radiance at $10.4\,\mu m$ for different blackbody temperatures normalised with respect to the spectral radiance of a two blackbodies emitting at $280\,K$ and $295\,K$. The graph shows the required flux level of artificial sky and BBU of the VOU at the VLT and in the laboratory in order to match the one of the background. 27

3.19 Variation of the flux level produced by the LN_2 normalised to the thermal radiation of the laboratory. The curve corresponds to the average signal value calculated at different time and was derived from a sequence of 2000 frames, each having $5\,ms$ of integration time. All frames were dark corrected, and only a square window of 25×25 pixels was considered. The background level was calculated by averaging 2000 frames, each having $5\,ms$ of integration time, while for the dark level 100 frames were averaged. 27

3.20 Variation of the dark level measured by the detector. The curve corresponds to the average signal value calculated at different time and was derived from a sequence of 2000 frames, each having $5\,ms$ of integration time, for which only a square window of 25×25 pixels was considered. Each data point of the graph was normalised with respect to the first frame of the sequence. 28

3.21 Variation of the flux level produced by the laboratory. The curve corresponds to the average signal value calculated at different time and was derived from a sequence of 2000 frames, each having $5\,ms$ of integration time. All frames were dark corrected, and only a square window of 25×25 pixels was considered. Each data point of the graph was normalised with respect to the first frame of the sequence. The dark level was calculated by averaging 100 frames. 28

3.22 Artificial sky used to reproduce in the laboratory the background level typical at the VLT. 29

3.23 Variation of the flux level produced by the artificial sky in the configuration with a single layer of plastic foil normalised to the thermal radiation of the laboratory. The curve corresponds to the average signal value calculated at different time and was derived from a sequence of 60 images, recorded after averaging 250 frames each having $4\,ms$ of integration time. All frames were dark corrected, and only a square window of 25×25 pixels was considered. Both background and dark level were recorded after averaging 250 frames, each having $4\,ms$ integration time. 30

3.24 Left: view of the detector when looking into a container filled with LN_2. Right: linecut of the uneven field seen by the detector when looking into a container filled with LN_2 normalised to the thermal radiation of the laboratory. Both background level and artificial sky images were dark corrected, and all frames were recorded after averaging 100 frames, each having $10\,ms$ integration time. The images were recorded in June 2018. . . 31

3.25 Schematisation of the reflections of internal and external thermal radiation which caused the non-flatness of the field seen by the detector. 31

3.26 Left: artificial sky with single plastic foil as seen by the detector after the implementation of the new baffle and D-shape mirror to mitigate parasitic light effects. Right: comparison of the linecuts of the field seen by the detector when looking at the artifcial sky through one layer of plastic foil after the implementation of the new baffle and D-shape mirror to mitigate parasitic light effects (orange continue curve) and into a container filled with LN_2 before the modifications (blue dash curve). Both background level and artificial sky images were dark corrected, and all frames that shows the residual parasitic light level were recorded after averaging 250 frames, each having $4\,ms$ integration time. The images showing the effects of the implemented modifications were recorded in August 2018 . . . 32

3.27 Total intensity of the thermal radiation for different temperature of the BBU, calculated for a square window of 25×25 pixels. Both background level and artificial sky images were dark corrected, and all frames were recorded after averaging 250 frames, each having $4\,ms$ integration time. The positive offset between the curves plotted with data from the first and second tests is caused by a temperature increment of the IR source, which in TIMMI2 cannot be cooled down rapidly by the blackbody housing. 34

3.28 Variation of the flux level of the BBU at $223\,K$ normalised to the thermal radiation of the laboratory, calculated for a square window of 25×25 pixels. Both background level and BBU images were dark corrected, and all frames were recorded after averaging 250 frames, each having $4\,ms$ integration time. 34

3.29 Raw linecut of the field seen by the detector when looking at the artificial sky with double plastic foil (blue, continue curve) and at the BBU at a temperature of $223\,K$ (orange, dash curve). Both frames were recorded after averaging 250 frames, each having $4\,ms$ integration time. The large offset in the central part is due to the fixed pattern produced by the detector. 35

3.30 Overall radiometric flux level of internal blackbody of the VOU and artificial sky, measured with the VOU not in its final configuration (as of August 2018). All images were recorded after averaging 250 frames, each having $4\,ms$ integration time. Before the normalisation, all images were dark corrected. For each data point, also the one standard deviation value is included. 36

3.31 Schematisation of the chopping scheme implemented in the detector readout controller. During the ELFN measurements, the VOU was connected to the readout controller and the trigger signal was given when the motor driving the D-shape mirror was passing through the homing position. The D-shape mirror was manually oriented so that when the motor was passing through the homing position, the D-shape mirror was starting to close the FoV of the instrument, allowing for correct integration of chopped images. . . 37

3.32 Left: image recorded at $9.6\,Hz$ in pseudo-chopping mode. Right: image recorded at $9.6\,Hz$ in real-chopping mode. 39

3.33 ELFN measurements in pseudo- and real-chopping mode. Data point collected in real chopping mode were plotted after nodding correction. It is important to note that measurements performed in pseudo- and real chopping are almost identical, as to validate the ability of the VOU to mitigate the ELFN of the AQUARIUS detector. 39

3.34 ELFN measurements in real-chopping mode without nodding correction. 40

4.1 Typical geometry of an AGPM coronapgraph, for which the following parameters are defined: depth of the grooves h, period of the grooves Λ, filling factor F, defined as the ratio of the width of the grooves over their period, and slope of the walls a. 42

4.2 Optical scheme of the AGPM coronagraph. The image contains the results of numerical simulations to show the effects of the AGPM coronagraph. 42

4.3 AGPM-BT1 coronagraph for the NEAR experiment. 43

4.4 Front side of the AGPM-BT1, where the rotationally symmetric subwavelength grating was produced. 43

4.5 Detailed view of the central core of the rotationally symmetric subwavelength grating of AGPM-BT1. 43

4.6 Back side of the AGPM-BT1, where the anti-reflective grating was produced. Due to a bit of astigmatism in the laser writer, the anti-reflective grating etched on the back side of the component has rectangular asperities (instead of square). This gives slightly different transmissions for different polarizations of light. 44

4.7 Front-end optics of the laboratory setup designed to test the AGPM coronagraphs. . . . 44

4.8 Back-end optics of the laboratory setup designed to test the AGPM coronagraphs. . . . 45

4.9 Laboratory setup designed to characterise the AGPM coronagraph. 47

4.10 Schematisation of the setup used to determine the optical axis of TIMMI2 at IR wavelengths. The $f = 750\,mm$ Ge lens is positioned as in the classic imaging mode of the optical setup designed to characterise the AGPM coronagraphs. 48

4.11 View of the TIMMI2 detector when looking at the flat mirror through the $f = 750\,mm$ Ge lens after its alignment with the optical axis. The region labelled *flat mirror* is the sum of different contribution that together generate a signal lower than the background level of the *laboratory*, and therefore clearly visible on the detector. 48

4.12 View of the TIMMI2 detector when looking at the laboratory after that two paper strips were placed in front of the dichroic window of the VOU in order to physically determine the optical axis. 49

4.13 Two paper strips were used to cut the FoV of TIMMI2 both horizontally and vertically in order to physically determine its optical axis. The source of the optical beam was directed towards the dichroic window of the VOU by using two folding mirrors, and then reflected back towards the setup. The path of the optical beam is shown in red. The image illustrates also the $f = 750\,mm$ Ge lens, positioned as in the classic imaging mode of the optical setup, and the flat mirror used to determine the optical axis at IR wavelengths. 49

4.14 The optical beam had to be reflected back by the flat mirror at exact the same location on the dichroic window to ensure that it was parallel to the optical axis of TIMMI2. . . 50

4.15 To ensure that the optical beam reflected by the dichroic window was aligned with the optical axis, it had also to pass through the centre of the $f = 750\,mm$ Ge lens, already aligned with the optical axis, which for convenience was replaced with a $\sim 1\,mm$ circular aperture. 50

4.16 PSF at the level of the coronagraphic plane at optical light $\sim 650\,nm$ for an $F_{\#} \simeq 30$ beam imaged with a CCD camera. 51

4.17 Pupil image for a $17.5\,mm$ aperture stop at $10.5\,\mu m$. Right: horizontal (up) and vertical (bottom) cut levels of the pupil image. 52

4.18 Left: pupil image for a $10\,mm$ aperture stop when illuminating a $500\,\mu m$ input pinhole using an external blackbody set at $110\,°C$. Right: horizontal (up) and vertical (bottom) cut levels of the pupil image. 53

4.19 Left: pupil image for a $10\,mm$ aperture stop when illuminating the $20\,\mu m$ input pinhole located at the coronagraphic image plane with the CO_2 laser. Right: horizontal (up) and vertical (bottom) cut levels of the pupil image. 53

4.20 Left: pupil image for a $10\,mm$ aperture stop when illuminating the $20\,\mu m$ input pinhole located at the AGPM location with the CO_2 laser and collimating the beam with a re-imaging $f = 200\,mm$ Ge lens. Right: horizontal (up) and vertical (bottom) cut levels of the pupil image. 54

4.21 Modified front-end optics of the laboratory setup designed to test the AGPM coronagraph after the replacement of the re-imaging $f = 250\,mm$ Ge lens with an $f = 200\,mm$ ZnSe lens. In order to limit degrading effects due to aberrations and vignetting, the beam was reduced to an $F_{\#} = 20$. All the modifications done are indicated by red bold labels. . . 55

4.22 Left: PSF recorded at $10.220\,\mu m$ after decentring AGPM-N3 of $\sim 3\,mm$ ($> 10\lambda/D$). The second peak on the right side of the image is most likely a filter ghost in TIMMI2. Right: coronagraphic PSF recorded at $10.220\,\mu m$ with AGPM-N3, obtained by minimising the flux and keeping a symmetric circular shape. 55

4.23 Pupil image for different axial position of AGPM-BT1. The image in the centre is the closest to the best focus, while top-left and bottom-right are respectively $4\,mm$ before and after it. Offset position with respect to the best focus (Z), residual total intensity of the pupil (I) and background level subtracted (B) are listed on top of each image. . . . 56

4.24 Sequence of coronagraphic pupil images recorded for AGPM-N3 during the centring of the Lyot stop with the aperture stop. Left: the aperture stop was reduced in size to clearly show the annular region. Centre: the aperture stop diameter was slowly increased again and the Lyot stop was adjusted in X and Y in order to obtain a symmetric image. Right: the aperture stop was further enlarged, and slightly oversized with respect to the 10 mm Lyot stop, to completely block the light of the annular region. 57

4.25 Fluctuation of the CO_2 laser intensity over a period of 4.5 min for three different wavelengths. The total intensity was calculated for pixels located within the FWHM of each PSF. Each curve was normalised with respect to the first measured value of the series. The two regions at 10.551 and 10.675 μm between 2.5 and 3.5 min where both curves shows a very steep variation are caused by the phase shift between the mechanical chopper and the detector readout controller. 58

4.26 Theoretical and measured off-axis transmissivity of an AGPM as a function of the angular separation between the optical axis and the centre of an AGPM, expressed in units of λ/D. 58

4.27 Theoretical transmission of AGPM-BT2. 61

4.28 Theoretical transmission of AGPM-N3. 61

4.29 Coronagraphic performance of the three AGPMs measured at a wavelength of 10.220 μm. The error bars in the contrast profiles represent one standard deviation. 62

4.30 Coronagraphic performance of the three AGPMs measured at a wavelength of 10.551 μm. The error bars in the contrast profiles represent one standard deviation. 63

4.31 Coronagraphic performance of the three AGPMs measured at a wavelength of 10.675 μm. The error bars in the contrast profiles represent one standard deviation. 64

4.32 Comparison between the theoretical and measured null depth for AGPM-BT2. 65

4.33 Comparison between the theoretical and measured null depth for AGPM-N3. 65

List of Tables

2.1 Comparison between the stars of the Alpha Centauri triple system and the Sun. 5

3.1 Nominal configuration of TIMMI2 used for all the tests performed. 25

3.2 Average temperature of the subsystems of TIMMI2 calculated over a period of five days. For each set of data, also the one standard deviation value is included. 29

3.3 Summary of the temperature levels of the BBU after each modification of the thermal interface between TIMMI2 and the VOU. In the calculation of the flux levels, both images of BBU and laboratory thermal radiation were dark corrected. The normalisation was done with respect to the laboratory flux level. 33

3.4 List of parameters chosen to record the various images depending of the chop frequency used. 38

3.5 ELFN measurements in pseudo- and real chopping mode for two different regions of the detector of size 25×25 pixels. It is important to note that measurements performed in pseudo- and real chopping are almost identical, as to validate the ability of the VOU to mitigate the ELFN of the AQUARIUS detector. For real chopping, ELFN measurements without nodding correction are also reported. 40

4.1 Simulation of the RMS WFE induced by the chosen elliptical mirror for a beam size of $F_{\#} = 13.4$. 51

4.2 Transmission of the three AGPMs at the different wavelengths tested. Results are expressed in terms of mean and one standard deviation value. 61

List of Abbreviations

ADI	Angular Differential Imaging
ADU	Analog-to-Digital Units
AGPM	Annular Groove Phase Mask
AO	Adaptive Optics
BBU	Blackbody Unit
CAD	Computer-Aided Design
BLIP	Background Limited Performance
CCD	Charge-Coupled Device
CU	Calibration Unit
DRS	Diagnostic/Retrieval System, Inc
ELFN	Excess Low Frequency Noise
ESO	European Southern Observatory
FoV	Field of View
FWHM	Full-Width-Half-Maximum
Ge	Germanium
HeNe	Helium-Neon
IBC	Impurity Band Conduction
IR	Infrared
KTO	Kampf Telescope Optics GmbH
LED	Light Emitting Diode
LN_2	Liquid Nitrogen
MIR	Mid-Infrared
NEAR	New Earths in the Alpha Cen Region
OTS	Off-The-Shelves
PSF	Point-Spread-Function
RMS	Root Mean Square
QE	Quantum Efficiency
QSS	Quasi-Static Speckle
S/N	Signal-to-Noise Ratio
TIMMI2	Thermal IR Multi-Mode Instrument 2
TSRQ	Technical System Requirement
UT	Unit Telescope
VFM	VISIR Flange Module
VISIR	VLT Imager and Spectrometer for the Mid-Infrared
VLT	Very Large Telescope
VOU	Vacuum Optics Unit
WFE	Wave Front Error
WFS	Wave Front Sensor
WFSU	Wave Front Sensor Unit
ZnSe	Zinc Selenide

Preface

The New Earths in the Alpha Cen Region (NEAR) experiment started back in 2016, and during the past couple of years many experts in different fields worked together to bring the project to its current status: ready to be shipped to the Paranal observatory for the final integration and commissioning.

My involvement in the project started in January 2018 with a four-months internship to modify the mid-infrared detector test facility in order to provide the required thermo-mechanical interface for the upcoming acceptance tests of the Dicke-switch chopper system. I decided to briefly summarise the main results of this internship in Section 3.4 of this thesis report, since they help to understand the reasons of few fundamental activities needed later in the project, but also of some final considerations.

The thesis started officially on 2$^{\text{nd}}$ May 2018, date in which part of the new hardware for the NEAR experiment was delivered to ESO. The main goals of this thesis project were the validation of the Dicke-switch chopper system for the mitigation of background and excess low frequency noise (ELFN), and also the characterisation of the new annular groove phase mask (AGPM) coronagraph, especially in terms of null depth and contrast level. The main activities in which I was involved during the past seven months of the thesis project are listed below, but their definition will be clear after reading the thesis report:

- Mechanical integration of the Dicke-switch chopper system with the mid-infrared detector test facility
- Verification of the radiometric requirement to characterise the Dicke-switch chopper system and the artificial sky to reproduce in the laboratory the background level typical at Paranal
- Evaluation of the parasitic light effects visible on the detector and caused by internal and external thermal radiation
- Measurements of the ELFN in pseudo- and real chopping mode
- Selection and integration of the opto-mechanical components for the setup designed to evaluate the coronagraphic performance of the AGPM
- Alignment of the setup at infrared wavelengths and verification of optical quality of the beam at both optical and infrared wavelengths
- Measurements of the AGPM transmission
- Measurements of the coronagraphic performance of the AGPM
- Data analysis for the characterisation of Dicke-switch chopper system and AGPM coronagraph

The successful completion of the activities listed above was also possible thanks to the support received from the other members of the NEAR team.

Serban Leveratto
Garching bei Muenchen, December 2018

1 Introduction

In 2016, Breakthrough Initiatives [1] and the European Southern Observatory (ESO) [2] signed an agreement to use the instrumentation available at the Very Large Telescope (VLT) of ESO at Cerro Paranal in Chile to investigate on the presence of potentially habitable worlds in the Alpha Centauri star system, the closest to the Sun [3]. More specifically, the New Earths in the Alpha Cen Region (NEAR) experiment involves the upgrade of the VLT imager and spectrometer for the mid-infrared (VISIR) [4] to improve its performance for the detection of Earth-like planets [3]. Indeed, although VISIR operates at a range of wavelength suitable for the detection and characterisation of exoplanets [5], in its current state it still does not have the required performance in terms of high contrast and sensitivity for the science goal of the NEAR experiment [6]. Part of the VISIR upgrade consists in a novel chopper system based on the Dicke-switch concept to suppress the excess low frequency noise (ELFN) suffered by the AQUARIUS detector array. The ELFN is a form of temporally correlated noise [5] characteristic of a specific type of devices, the impurity band conduction (IBC) detectors [7], and can be mitigated by modulating the incident light at high enough frequency [5]. Besides the mitigation of the ELFN to achieve the required sensitivity, the other main challenge of the NEAR experiment is the need of high contrast to image the circumstellar environment, where habitable planets, if present, are expected to orbit. This will be achieved through the implementation of an annular groove phase mask (AGPM) coronagraph for the suppression of the central peak of the star's point-spread-function (PSF)[6].

This thesis report describes in details the laboratory test phase completed at ESO Headquarters to validate the Dicke-switch chopper system and characterise the AGPM coronagraph. Chapter 2 presents the scientific drivers of the NEAR experiment and also the main technical challenges, especially in terms of high contrast and sensitivity, required to detect potentially habitable planets in the Alpha Centauri region at mid-infrared (MIR) wavelengths. The main hardware modifications to be implemented in VISIR and the MIR detector test facility where all the tests were performed are also described.

Chapter 3 focuses on the validation of the Dicke-switch chopper system to assess its ability to remove the background level and mitigate the ELFN which limits the sensitivity achievable with VISIR. After providing background information about the AQUARIUS detector, the chapter explains the concept of chopping and nodding, a method typically used for background correction for observations at IR wavelengths. Then, an overview on the design of the Dicke-switch chopper system and on the modifications required to implement the required thermo-mechanical interface in the mid-IR detector test facility are given. The discussion of the actual laboratory characterisation and the obtained results conclude the chapter. All the main tests to verify the achievable radiometric level and validate the ability of the system to suppress the ELFN are presented.

The characterisation of the AGPM coronagraph is described in Chapter 4. After a general introduction on the physical structure of an AGPM coronagraph and its working principle, the laboratory setup designed for the laboratory characterisation is presented in details, together with the alignment procedure followed to ensure a good optical quality in order to limit the influence of residual aberrations and vignetting on the coronagraphic performance. Test methodologies and data analysis are then reported. The chapter ends with a discussion of the test results.

Chapter 5 summarises all the activities performed during the laboratory characterisation of both Dicke-switch chopper system and AGPM coronagraph. Based on the obtained results, current status of the project and future work are also discussed.

2

NEAR experiment: scientific drivers and technical challenges

The NEAR experiment is part of Breakthrough Watch [8], a project whose goal is to detect and eventually characterise Earth-like planets orbiting around Alpha Centauri and other stars located within 20 light years from Earth, in search for traces of oxygen and other potential biosignatures [8].

More details about the NEAR experiment are given in this chapter. First of all, Section 2.1 presents the main scientific drivers of the project, and more in general of the field of exoplanet exploration. Section 2.2 explains the motivations and the main challenges of detecting exoplanets at MIR wavelengths and then justifies the selection of VISIR for the NEAR campaign, which sets strict requirements in terms of sensitivity and high contrast. As a matter of fact, few modifications in the current design of the instrument are needed. As discussed in Section 2.3, most of the new hardware has been implemented on the so called VISIR flange module (VFM), formed by three main subsystems: vacuum optics unit (VOU), wave front sensor unit (WFSU) and calibration unit (CU). After briefly introducing these three subsystems, an overview on the MIR detector test facility used to perform all the tests is provided in Section 2.4.

2.1. Scientific drivers for exoplanet exploration

The exploration of exoplanets started only in the late 1980s with the first candidate exoplanet detected in 1987, but confirmed only at a later time [9]. As shown in the diagram of Figure 2.1 (as of 18$^{\text{th}}$ October 2018), the first discoveries raised rapidly the interest in this new research field among all the astronomical community, and in the following years many exoplanet detection methods were developed [9]. Despite the short history, in thirty years the number of known exoplanets has increased exponentially, and at present (as of 22$^{\text{nd}}$ October 2018) there are 3791 confirmed exoplanets, 155 of which are terrestrial, in 2828 solar systems and additional 2919 candidate exoplanets [10].

One of the main reasons to study exoplanets is that extrasolar planetary systems can provide key information on the planetary formation process [12], especially considering their diversity in terms of planetary environments and stage of development. [13]. The ultimate goal of exoplanet research is the detection of forms of extra-terrestrial life, therefore the step following the detection of potentially habitable planets is their characterisation. According to the current knowledge, based only on the organisms living on Earth, the main requirement for life is liquid water. At a first approach, those conditions limits the planets expected to be habitable to the ones that are orbiting within the habitable zone of their parent star [13–15], defined as the region in which the flux of a parent star is enough to allow liquid water on the surface of a planet [13, 14].

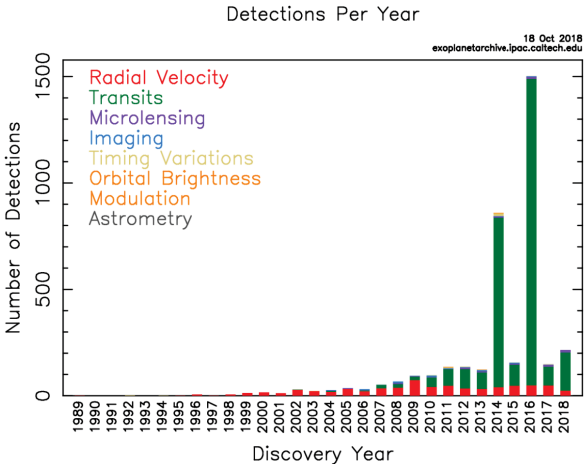

Figure 2.1: Number of discovered exoplanets for each year from 1989 to 2018 grouped depending on the detection method used (as of 18$^{\text{th}}$ October 2018) [11].

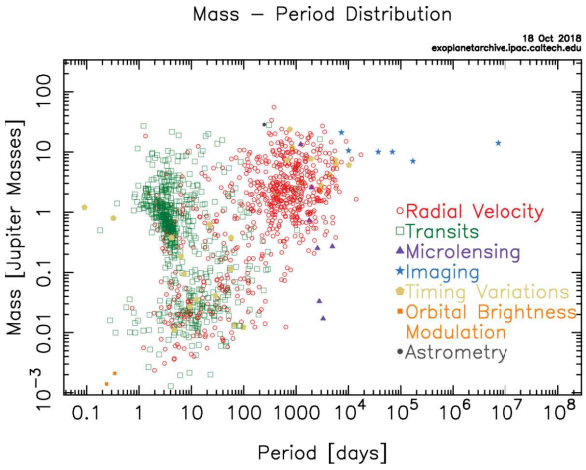

Figure 2.2: Distribution of exoplanets with respect to their orbital period and mass, grouped depending on the detection method used (as of 18$^{\text{th}}$ October 2018) [11].

However, the fact that a planet orbits within the habitable zone of its parent star does not ensure that the planet is habitable, but other conditions in terms of surface pressure and temperature have to be verified [14].

Unfortunately, for exoplanets it is not possible to directly detect gaseous or liquid water [14] using ground based telescope because of the absorption variations of telluric H_2O which dominates at wavelengths longer than $\sim 600\,nm$ [9], while currently available space based telescopes are limited in size and not equipped with sufficiently sophisticated instrumentation. Therefore, a possible way to assess their habitability from remote observations is through the detection of biosignature gases in their atmosphere [13, 14], products associated with biological processes [9, 13, 14]. Instruments that combine imaging and spectroscopy modes have the advantage that they can be used at first to detect an exoplanet through direct imaging to eventually perform spectroscopic analyses to look for biosignatures in its atmosphere [9]. However, Figures 2.1 and 2.2 highlight two important aspects of detecting exoplanets using direct imaging. First, from Figure 2.1 it is quite clear that this method is not the most efficient. Indeed, so far (as of 22$^{\text{th}}$ October 2018) only 44 confirmed exoplanets were detected through direct imaging ($\sim 1\%$) [11]. Second, Figure 2.2 shows that most of them are Jupiter-size planets orbiting at a much larger distance from their parent star than typically expected for Earth-like planets. This is a consequence of the difficulties in imaging Earth-size exoplanets at small angular separation from their parent star [14], a fact that, as discussed in Section 2.2, sets the main technical requirements for the NEAR experiment.

2.1.1. Overview on the Alpha Centauri region

The primary target of the NEAR campaign is Alpha Centauri, the nearest star system to the Sun, located at 4.36 light-years distance and formed by three components. Alpha Centauri A and B are the two main stars of the system and they both have characteristics analogous to the Sun. The third star of the system, called Proxima Centauri, is a red dwarf, considerably smaller and colder than its companions [16].

Because of their significant similarities to the Sun, as highlighted in Table 2.1, Alpha Centauri A and B are extremely attractive for their possibility to host potentially habitable Earth-like planets. This hypothesis has been strengthen by the announcement of two recent discoveries in the Alpha Centauri region: the nearest terrestrial exoplanet to Earth having a mass of 1.3 Earth-masses and orbiting within the habitable zone of Proxima Centauri [17] and a dust ring located around the same red dwarf, which may indicate the existence of a more extended planetary system [18].

Table 2.1: Comparison between the stars of the Alpha Centauri triple system and the Sun [16].

Parameter	**Alpha Cen A**	**Alpha Cen B**	**Proxima**	**Sun**	*Unit*
Age	4850	4850	4850	4650	million years
Mass	1.100	0.907	0.123	1.000	solar mass
Radius	1.227	0.865	0.145	1.000	solar radius
Temperature	5790	5260	3040	5770	Kelvin
Luminosity	1.519	0.500	0.000138	1.000	solar luminosity
Hydrogen	71.5	69.4	69.5	73.7	percent
Helium	25.8	27.7	27.8	24.5	percent
Heavier elements	2.74	2.89	2.90	1.81	percent

1 solar mass = 1.989 x 10^{33} g
1 solar radius = 6.96 x 10^{5} km
1 solar luminosity = 3.827 x 10^{26} watts

The indicated chemical composition is that at the surface of the star.

2.2. Observations in the MIR spectral regime

In Section 2.1 it was already discussed that direct imaging is not a common method for exoplanets detection, and the few exoplanets successfully detected with this technique are primarily Jupiter-size. Indeed, the closer vicinity of an Earth-like planet to its parent star, together with the fact that stars can be billions of times brighter, makes direct imaging a very challenging method for the detection of smaller exoplanets [14].

Observations of potentially habitable planets are recommended in two ranges of wavelength of the spectrum: the near-infrared and the N-band in the MIR. In the near-infrared, the spectrum of the starlight reflected by a planet, whose atmosphere is characterised by peculiar absorption bands, contains potential biosignatures of O_2 and O_3, while the blackbody emission spectrum of a planet in the N-band encompasses potential biosignatures of O_3 [5].

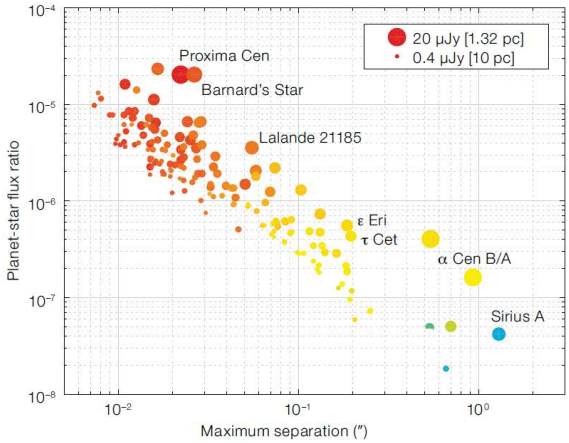

Figure 2.3: Planetary-star flux ratio in the N-band regime for Eart-like planets located within 10 pc. The size of the dots indicates the apparent brightness of the planet, while the colours resemble the ones of the parent stars [5].

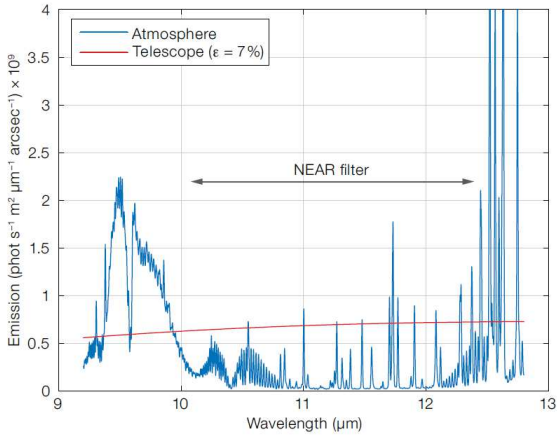

Figure 2.4: Simulation of the sky background level using the ESO SKYCALC Sky Model Calculator and telescope contribution to the background level (mirrors at 280 K and combined emissivity of 0.07) [5].

Compared to visible wavelengths, in the MIR, even though the star can still be millions of times brighter than a planet [3], the thermal radiation of the planet reduces the brightness gap with respect to its parent star [3, 9], as the thermal radiation emitted by the planet increases, while the star flux is reduced. On the other hand, longer wavelengths imply a lower diffraction-limited angular resolution of the telescope [9]. Earth-like planets are expected to orbit closer to their parent star, and therefore at a lower angular separation from it. In the MIR, the contrast required for the detection of similar objects has an order of magnitude between 10^{-5} and 10^{-7}, as shown in Figure 2.3. With existing 8-meter-class telescopes it is generally not possible to image Earth-size planets in the habitable zone of solar type stars for lack of sensitivity and angular separation. However, the angular separation between Alpha Centauri A and B and their habitable zone is $\sim 1''$, large enough to meet the stringent requirements at N-band wavelengths in terms of spatial resolution, high contrast and sensitivity using advanced ground-based observatories [5]. Moreover, in the N-band, extended from 8 to 13 μm, the atmospheric spectrum presents a high level of transmissivity, in particular between 10.5 and 12.5 μm. The main limit of ground-based instruments for MIR observations is the high background level produced by the atmosphere and the warm optics of the telescope, thus their sensitivity is often not comparable to the one of space-based observatories [19]. Yet, a second advantage of operating in the N-band is that at this wavelengths the atmospheric emission spectrum is attenuated, and the telescope emission is the dominant source of background radiation, as illustrated in Figure 2.4 [5].

2.2.1. Main challenges for the NEAR experiment

The selection of VISIR for the NEAR experiment is a result of the above considerations. The instrument operates in the three atmospheric windows of the MIR regime: the M-band at $5\,\mu m$, the N-band, and the Q-band between 17 and 20 μm [19].

The primary targets of MIR astronomy are circumstellar environments for the study of stars and planets formation through the analysis of the thermal emission of dust or warm molecular hydrogen. Considering the close vicinity of these regions to the star, their observations require high angular resolution, and therefore image quality was a major driver requirement of the VISIR design. At MIR wavelengths, the angular resolution of a ground-based instrument is limited by the aperture of the telescope [20], hence VISIR has diffraction-limited performance of $\sim 0.3''$ in the N-band, an order of magnitude better than the Spitzer Space Telescope [19]. On the other hand, ground-based instruments cannot compete in terms of sensitivity with their space-based analogues due to the high background level caused by atmospheric and telescope emissions [20]. Any state-of-the-art MIR instrument has to be cooled down so that the internal background generated by the thermal radiation of optics and mechanics become negligible as compared to the unavoidable thermal radiation from sky and telescope. For VISIR, cooling the optical bench and the structure to $\sim 29\,K$ and to $\sim 15\,K$ for the components closer to the detectors [19] allows to limit the background produced by the optics emission to less than 1% [21]. Similarly, both detectors of VISIR are cooled to $\sim 9\,K$ [19] in order to avoid excessively high levels of dark current [20].

The characteristics of VISIR, the only instrument at the VLT operating in the MIR regime [22], are better exploited in combination with other instruments. It can be used together with other ground-based instruments to cover a larger spectral domain or with space-based instruments for follow-up observations. Nonetheless, its high spatial and spectral resolution [23] allows to make use of VISIR for the NEAR experiment, but high contrast and sensitivity are still the major challenges that have to be overcome, and thus they drive the main modifications of the instrument [6].

High contrast

The minimum contrast level for the NEAR experiment at a wavelength of $11.25\,\mu m$ is dictated by the Alpha Centauri A component, which sets the required value of the contrast to $\sim 6 \cdot 10^{-7}$ at a separation of $2.8 - 3.8\,\lambda/D$ or $0.8'' - 1.1''$, compared to the $\sim 1.5 \cdot 10^{-6}$ for Alpha Centauri B at a separation of $2\,\lambda/D$ or $0.5'' - 0.65''$ (see also Figure 2.3). However, in its present state VISIR provides a contrast level of $\sim 10^{-5}$ at $\sim 1''$.

From the phase-A analysis of the campaign it was concluded that three complementary improvements have to be implemented to enhance the seeing limited PSF and attain high contrast images: adaptive optics (AO), AGPM coronagraph to suppress the star's PSF peak, and presented more extensively in Chapter 4, and angular differential imaging (ADI) post-processing technique [6].

AO is a technique which is used for real time compensation of atmospheric fluctuations with a time scale of the order of $1\,ms$ in order to achieve a diffraction-limited angular resolution. A wave front sensor (WFS) measures continuously the wave front of a reference guiding star, or alternatively of an artificial laser guide star, and then the wave front error (WFE) is corrected by deforming a mirror using actuators which typically operate at frequency of the order of $1\,kHz$. A schematisation of this concept is reported in Figure 2.5.

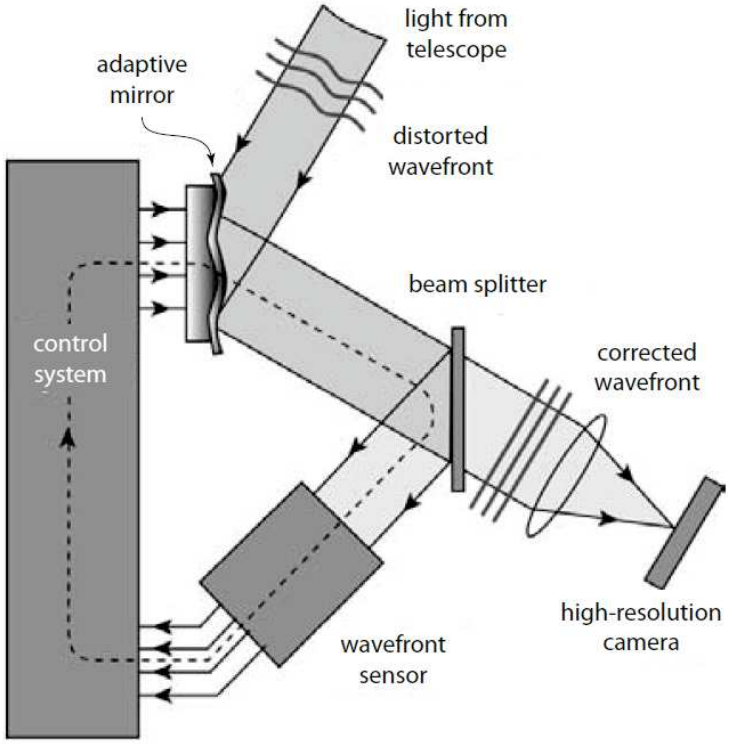

Figure 2.5: Schematisation of a typical AO concept for the real time correction of atmospheric fluctuations [9].

Imperfections in the telescope mirrors and in the instrument optics create quasi-static speckle (QSS) patterns and the noise associated to this effects can be larger than the residual shot noise [9]. The ADI technique is used to calibrate the QSS.

At an altazimuth telescope, like the VLT, in order to follow an object on the sky the telescope needs to move in altitude and azimuth. Without the addition of a third movement, in the focal plane the image would still rotate. Supposing to look at the celestial pole, the telescope would stand in a fixed position, but still the sky would rotate. So normally, the third movement consists in rotating the instrument. ADI replaces the mechanical rotation of the instrument with rotating the image in post processing software. A sequence of frames is captured with the rotator of the telescope switched off, so that instrument and telescope optics are aligned, and the stability of the QSS is enhanced. As mentioned above, without rotating the instrument, the field of view (FoV) between consecutive images rotates. After that the entire sequence is captured, a reference model associated to the effect of QSS is calculated and eventually removed from each frame. All the QSS-corrected images are then rotated to align the FoV and co-added to improve the signal-to-noise ratio (S/N) [24].

Sensitivity

The goal sensitivity for the NEAR experiment is $\sim 80\,\mu Jy$[1], which corresponds to the brightness of a two Earth-radius planet in the Alpha Centauri region ($\sim 1.25\,pc$) at a wavelength of $11\,\mu m$. This is only an indicative value, since the surface temperature of the planet and the presence of clouds in its atmosphere can increase or decrease by a factor of two the brightness level specified above. By using AO, the Strehl ratio can be improved close to the unit value. Besides that, an optimised filter for the N-band can enhance the S/N and reduce its dependency on the atmospheric condition [6], avoiding in particular O_3 absorption features below $10\,\mu m$ and degrading atmospheric window longwards $13\,\mu m$ [5, 6]. In addition, a freshly coated or wet cleaned mirror would allow to further improve the BLIP sensitivity [6].

The estimation of the instrument performance after the upgrade has been scaled from real data of VISIR observations, and considering all the above improvements the expected BLIP sensitivity is $\sim 700\,\mu Jy$, still one order of magnitude larger than the $\sim 80\,\mu Jy$ required. However, if the noise scales proportionally to the inverse of the exposure time, a final BLIP sensitivity of $\sim 70\,\mu Jy$ ($5\,\sigma$/100h) can be achieved through the co-addition of consecutive frames[5], a technique largely used for MIR observations [25]. Indeed, exposure shorter than $10\,ms$ [26] are necessary to reduce the risk of saturation caused by the high background level, and thus the S/N is enhanced co-adding multiple images [25].

It is noteworthy that the noise reduction by means of co-addition is effective only if the consecutive frames are spatially and temporally uncorrelated. In principle, this is not the case for the VISIR detector since it is affected by the ELFN, a form of temporally correlated noise characteristic of IBC detectors, which however can be mitigated by chopping the incident flux at a sufficiently high frequency [5], as discussed in details in Chapter 3.

2.3. Design description of the VISIR flange module

Most of the modifications required for the NEAR experiment have been implemented on a non-cryogenic flange [5]. The VFM is shown in Figure 2.6 and will be placed between the VISIR cryostat and the VISIR telescope mounting flange, a space currently occupied by the star simulator, also known as calibration unit, as shown in the VISIR assembly of Figure 2.7, which will be dismounted and partially refurbished. As illustrated in Figure 2.6, the VFM comprises three main subsystems. This section provides only an overview of the main functions of WFSU and CU, while the VOU design is described in details in Section 3.3.

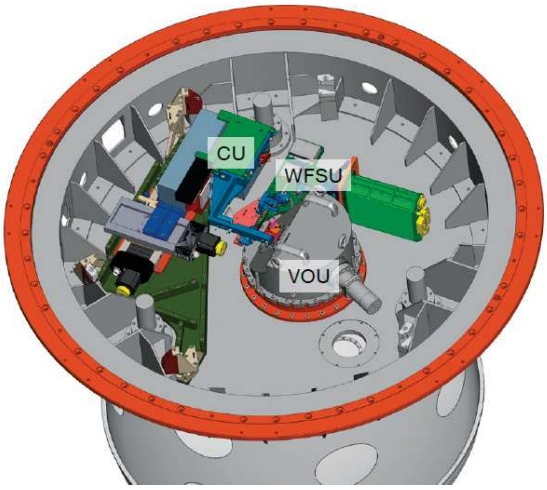

Figure 2.6: Complete assembly of the VFM [5].

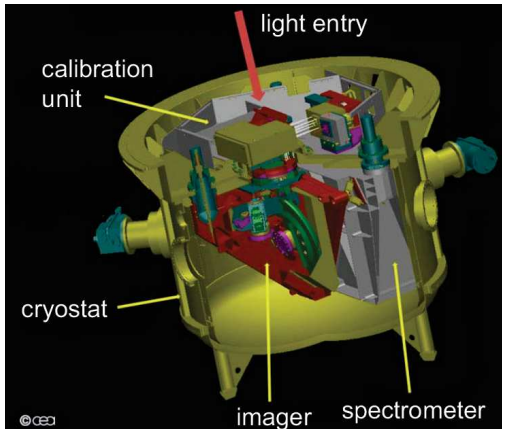

Figure 2.7: Cross-sectional view of VISIR [27] .

[1] $1\,Jy = 10^{-26}\,W/(m^2\,Hz)$

2.3.1. Wave front sensor unit

As already presented in Section 2.2, the main function of the WFSU is to measure the distortion of the incoming wave front caused by atmospheric turbulences. The VOU mounts a coated zinc-selenide (ZnSe) vacuum window, tilted at 45° with respect to the telescope beam, that acts as a dichroic filter. More specifically, the visible wavelengths of the light are reflected towards the WFS, while between 10 an 12.5 μm light can pass and reach the VISIR cold stop. The working principle is the same as the beam splitter illustrated in Figure 2.5. The difference in the WFE measured at the VISIR cold stop and at the WFSU is compensated including an offset value in the WFS, so that the AO facility can properly correct the WFE through the controlled deformation of the secondary mirror of the unit telescope 4 (UT4) [28].

2.3.2. Calibration unit

The CU consists of a 50 μm pinhole placed at the output of a monochromator [28] in order to simulate an IR point-like source and verify the performance of VISIR and calibrate it [29]. Two motorised stages allow to position the point-like source over the complete FoV of the instrument [29] along the horizontal and vertical directions, while a third motorised stage is used to move the entire CU along the optical path of the beam [28].

2.4. TIMMI2: the MIR detector test facility

For the first characterisation of the new AQUARIUS detector of VISIR, implemented during the first upgraded of the instrument started in 2010, a test facility able to provide the required temperature level, low thermal background and cryogenic optics to homogeneously illuminate the detector array was needed. To avoid a new complex design, and also contain development costs and limit the risk of delays, the decommissioned thermal IR multimode instrument (TIMMI2), previously operating at the 3.6-metre-telescope on La Silla observatory, was converted to a test facility, since its characteristics make it appropriate to meet the requirements of the new AQUARIUS detector [23].

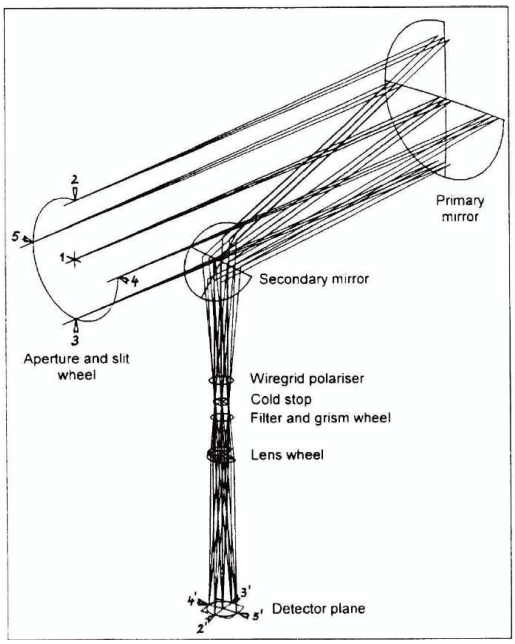

Figure 2.8: TIMMI2 optical layout [30].

Figure 2.9: TIMMI2 cryostat and entrance window [23].

TIMMI2 was a focal reducer of variable magnification with front-end and back-end optics. The complete optical layout is shown in Figure 2.8. After passing through the entrance window, the light beam encounters the cryogenic aperture wheel, where various field masks and slits are mounted. Two off-axis spherical mirrors form the front-end optics, whose main function is to fold the optical beam of 90° in order to limit the instrument size and provide a compact design. The first element of the back-end optics is a retractable and rotatable wiregrid polariser, followed by cold stop, filter and grism wheel, lens wheel and eventually the IR detector array, thermally isolated from the rest of the optics [30].

All the optical elements of the instrument are mounted on an aluminium cold structure, which has to be cooled down to cryogenic temperatures in order to provide BLIP in all the main observing modes. Two fibre glass laminate wheels provide the required thermal isolation and stability to the cold structure and connect it to the cryostat, shown in Figure 2.9, which provides all the necessary interfaces, in particular to cold head, vacuum gauges, vacuum pump, motors, electrical feedthroughs for sensors, heaters and acquisition electronic. A radiation shield surrounds all the optical elements to minimise the radiation heat transfer [30].

3

Characterisation of the Dicke-switch chopper system to mitigate the ELFN: laboratory tests and results

The commissioning of the first VISIR upgrade took place in 2012. The upgrade should have improved the performance of the instrument, providing in particular BLIP for imaging and low resolution spectroscopy thanks to the new AQUARIUS detector array, the main cornerstone of the upgrade. Surprisingly, even though the laboratory testing phase to characterise the detector had confirmed the expected performance, the on-sky sensitivity measured during the first observations was 2-3 times smaller than the previous detector from Diagnostic/Retrieval System (DSR). As a result, VISIR was not considered ready for on-sky science operations and a new testing phase to disclose the causes of the lower sensitivity was planned. The conclusion was that the ELFN was the cause of the degraded sensitivity[31]. In Section 2.2 it was already mentioned that co-addition of consecutive frames is needed to improve of a factor 10 the sensitivity of VISIR in order to achieve the $\sim 70\,\mu Jy$ (5 σ/100h) required for the NEAR experiment. To effectively do so, the co-added frames have to be spatially and temporally uncorrelated, thus the ELFN has to be suppressed.

One of the available options for the NEAR experiment to mitigate the effects of the ELFN consists of a chopper system based on the Dicke-switch concept. The laboratory characterisation of this new system to assess its ability to suppress background level and ELFN is described in this chapter. After providing an overview on the performance of the AQUARIUS detector of VISIR and effects of the ELFN in Section 3.1, possible methods to mitigate the ELFN are discussed in Section 3.2, with a particular focus on the Dicke-swich chopper system for the NEAR experiment, whose designed is described in Section 3.3. The laboratory activities to implement the Dicke-switch with the mid-IR detector test facility of ESO, verify the radiometric requirements, and prepare the setup for the final tests are reported from Section 3.4 to 3.6. Sections 3.7 and 3.8 discusses respectively test methodologies and final results of the tests for the ELFN mitigation.

3.1. Limited sensitivity of the AQUARIUS detector

3.1.1. Physical structure of IBC photodetectors

For extrinsic photoconductors the value of the absorption coefficient is proportional to the concentration of atoms of the doping element, which for conventional architectures is limited by two factors: the solubility of the doping element into the intrinsic crystal and hopping, a phenomenon for which the conduction of electrons can take place from one impurity atom to another without the necessity to

provide the needed band gap energy to the electrons. In order to compensate for these limitations and enhance the quantum efficiency (QE), extrinsic photoconductors require a larger active volume, and thus a thickness of the order of 1 mm [32]. Nevertheless, an excessively large thickness generates other undesired issues such as large electrical crosstalk, transient response problems and sensitivity to high energetic particles [33].

On the contrary, the higher doping level characteristic of IBC detectors, at least two order of magnitude larger than traditional solutions, allows to obtain a higher QE at a reduced volume [33]. Referring to Figure 3.1.a, the flow of dark current generated by hopping in the heavily doped IR-active layer is interrupted by a high-purity layer of intrinsic material, the blocking layer, which increases the electrical resistance of the detector, permitting only the transit of electrons of the conduction band. Because the conduction band is the same for both the IR-active layer and the blocking layer, once that an incoming photon raises an electron to the conduction band, this can move undisturbed to the electric contact [32]. The IR-active layer can have a thickness between 25 and 35 μm, while the intrinsic layer is between 3 to 4 μm thick.

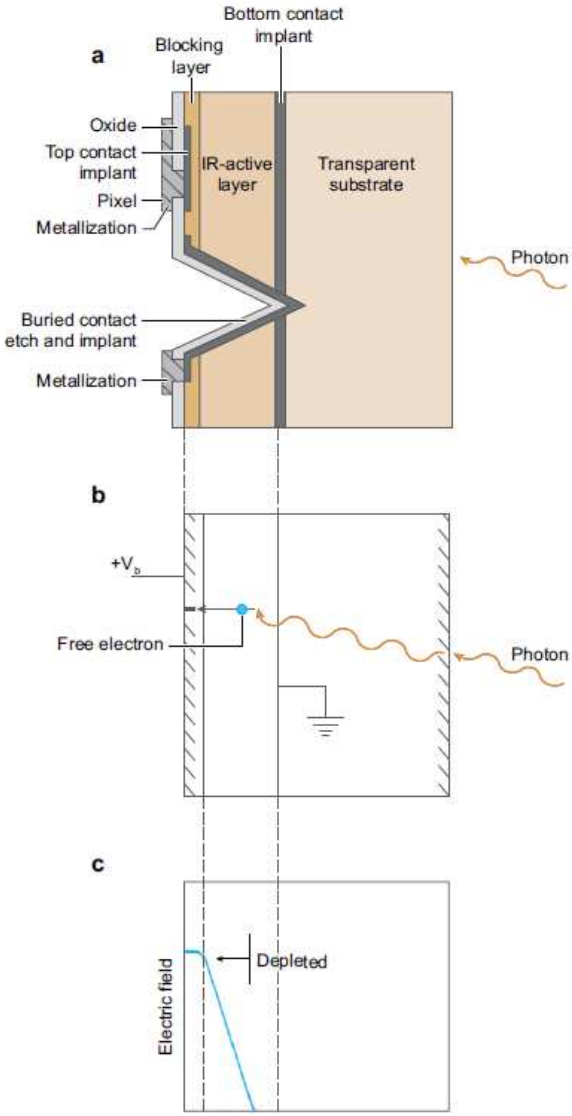

Figure 3.1: *a)* Cross-sectional schematisation of the structure of a back-illuminated IBC detector, where the upper metallised region is the contact for a pixel *b)* Application of the detector bias voltage for the collection of photogenerated free electrons *c)* Electric field and extension of the depleted region [34].

This process is possible only if a bias is applied across the detector in order to suppress the high conductivity of the IR-active layer and collect the electron generated by the incoming photons [34]. In particular, as shown in Figure 3.1.b, the contact on the blocking layer requires a positive bias, with respect to the one of the IR-active layer, in order to avoid a high level of dark current through the detector which would be generated by a negative bias [32]. Because of this positive bias, a concentration of negative carriers is formed at the interface between the IR-active layer and the blocking layer, while the positive ones move away from it. As shown in Figure 3.1.c, this causes a high-resistance region depleted of free carriers of charge. The application of a larger detector bias allows to achieve higher efficiency extending the depleted region across the whole IR-active layer [34].

3.1.2. Characteristics of the ELFN

The ELFN is a phenomenon which was described for the first time more than 30 years ago by Stapelbroek et al [7], who showed how the ELFN for IBC detectors operating at intermediate IR background greater than $\sim 10^{12}\, ph\, cm^{-2}\, s^{-1}$ and at a frequency lower than $10\, Hz$ is approximately 5-10 times larger than at higher frequencies. Referring again to Figure 3.1.a, the ELFN is caused by the fluctuations of electric charges generated through consecutive ionisations and recombinations in the blocking layer due to the absorption of photons by residual impurity atoms. This implies a fluctuation of the potential across the IR-active layer, and therefore a randomly modulated response. According to existing theoretical models, the ELFN acts as a high gain, low QE photoconductor in series with the IBC detector considered [7].

The main characteristics of the ELFN noise are shown in the two graphs reported in the Figures 3.2 and 3.3. According to Figure 3.2, the ELFN noise increases with the detector bias, and it does not show 1/f characteristics for values larger than $0.25\, V$. The noise increases also for higher flux levels, implying a lower S/N, as reported in Figure 3.3. In both figures, the ELFN shifts towards higher frequency of the signal [7]. To explain this, it is necessary to introduced τ, the dielectric relaxation constant, defined as the time scale required to neutralise the field created by the charge separation in a photoconductor [32] and inversely proportional to the electron current. The low impurity level of the blocking layer implies that the ELFN is characterised by large values of τ. However, the current generated in the blocking layer increases with both the detector bias and the flux impinging on the detector area, which contributes to reduce τ, shifting the cut-off frequency of the ELFN at higher values [7].

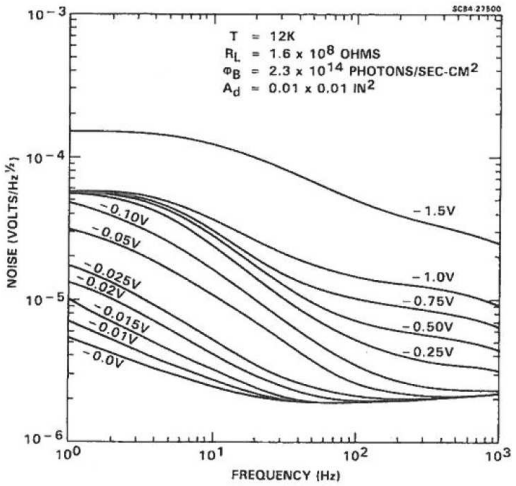

Figure 3.2: Variation of the ELFN as a function of the detector bias [7].

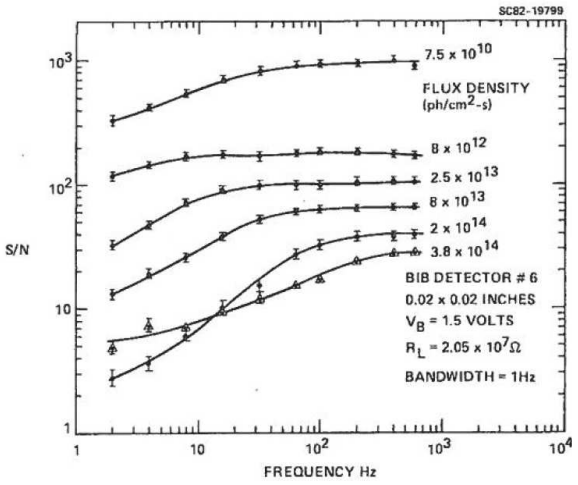

Figure 3.3: Variation of the ELFN as a function of the flux level impinging on the detector [7].

3.1.3. ELFN of the AQUARIUS detector

The ELFN was identified to be the main cause of the much lower performance showed by VISIR after the commissioning in 2012, but due to ITAR regulations it is not allowed to investigate on the structure of the detector [25]. However, the AQUARIUS detector was initially developed for space-based observations in low background level environments, and therefore its thick blocking layer might support this hypothesis [31]. As a matter of fact, similar characteristics with respect to the ones shown in Figures 3.2 and 3.3 were detected after the second run of laboratory tests.

It was confirmed that high flux levels induce a larger ELFN, as illustrated in Figure 3.4, where the variation of the detector noise with the chop frequency is plotted for different values of the input flux. Another conclusion derived from this graph is that the noise factor, defined as the ratio between the noise at $0.25\,Hz$, the typical chop frequency of the secondary mirror of the UT3, and the noise measured at $100\,Hz$, is ~ 4, and thus the measured noise is four times higher than expected. This aspect is very important when the co-addition of consecutive frames is used for noise mitigation. Indeed, for the AQUARIUS detector this reduction is four time lower due to the autocorrelation of up to few hundreds milliseconds between consecutive frames. The effect of the temporal autocorrelation on the co-addition of consecutive frames are visible in Figure 3.5, which reports the theoretical and experimental variation of the noise for both the readout noise and the shot noise limited regimes. Before the commissioning phase in 2012, only the tests in the readout noise regime were conducted, while the ones in the shot noise regime were performed afterwards. This decision was based on the assumption that the read noise regime was considered to be the worst operating condition for the detector, and since the measured data were in accordance with the expectation, measurements at high flux level were not assessed [25].

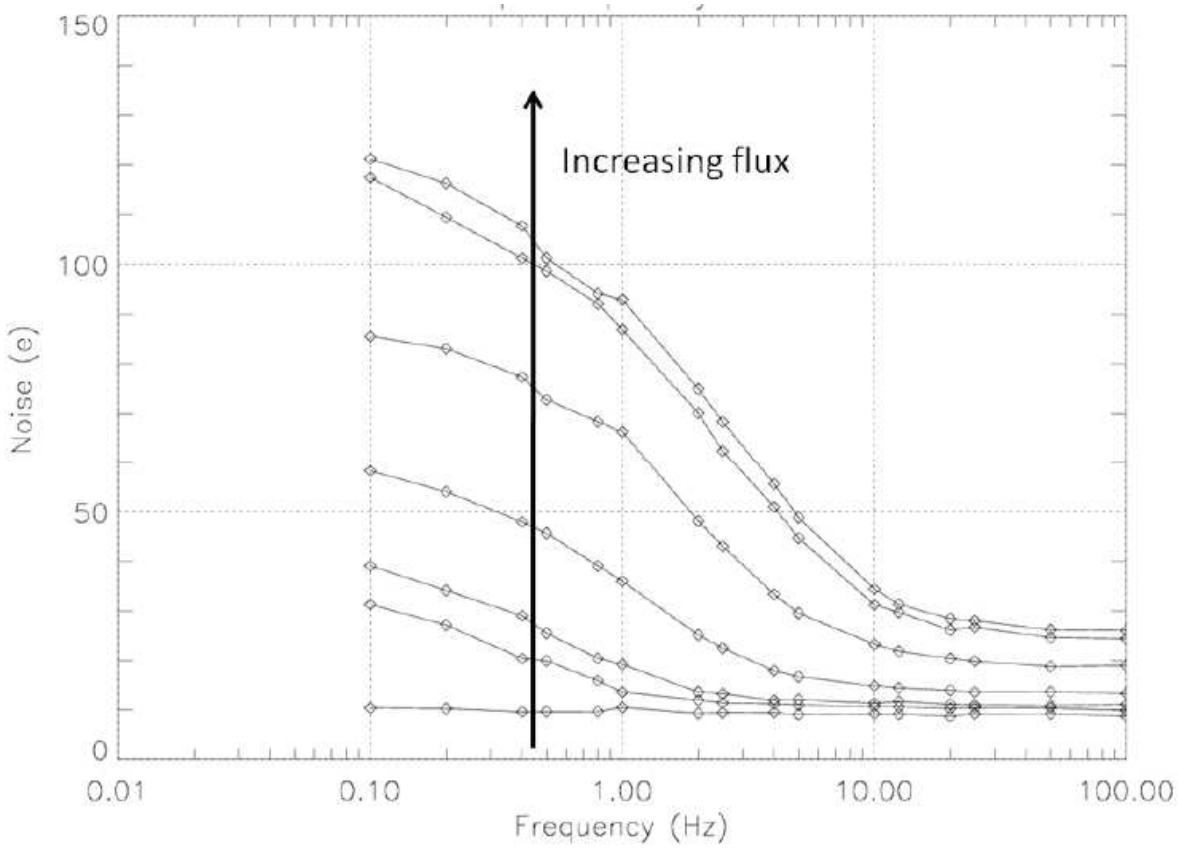

Figure 3.4: Variation of the noise in the AQUARIUS detector as a function of the chop frequency for different flux levels, derived with pseudo-chopping from frames recorded in burst mode [25].

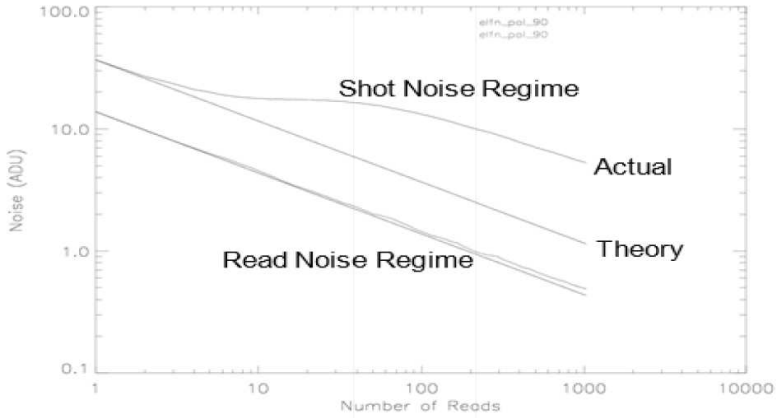

Figure 3.5: Variation of the noise in the AQUARIUS detector as a function of the total number of co-added frames for high and low flux levels [25].

3.2. Mitigation of the ELFN

In their work [7], Stapelbroek et al identified two possibles ways to mitigate the ELFN, both at the level of the detector structure: a thinner blocking layer, which has been experimentally demonstrated to be effective, and a sharper interface, in terms of doping concentration, between the IR-active layer and the blocking layer [7]. The development of the AQUARIUS detector was done with a contract on a 'best effort basis'. Due to financial and managerial constraints, ESO could not launch a second try to arrive at a better detector, and therefore different alternatives had to be considered to mitigate the ELFN. Internal chopping mechanisms are not feasible due to their high risk in terms of performance and development schedules. Limiting some operational parameters of the instrument can also contribute to mitigate the ELFN, like for example decreasing the flux impinging on the detector, increasing the integration time and including a dead-time between consecutive frames. However, considering the short exposure time required for MIR observations in order to avoid saturation in high background environments, this is again not feasible. Chopping the incident flux at high enough frequency is therefore the only feasible option [25], thanks to the fact that the AQUARIUS detector can operate at high frame rates and the available processor can address the increased level of data flow [35].

The phase-A analysis of the NEAR experiment concluded that for VISIR chopping can be implemented in two different ways in order to suppress the ELFN of the AQUARIUS detector: chopping using the secondary mirror of the UT4 or using a chopper system based on the Dicke-switch concept [6].

3.2.1. Chopping and nodding

Astronomical observations in the MIR are characterised by high level of background radiation, normally several order of magnitude brighter then the target object. In order to avoid the detector saturation, the frames are captured at a high speed rate [25]. The background is then removed through differential observation technique, such as chopping and nodding. An example of this technique is shown in the schematisation of Figure 3.6.

Chopping consists in observing two different portion of the sky, one including the source to be observed and the other one containing only the background radiation, sum of atmospheric and telescope emissions. The variation in the background level has a time-scale of few seconds, thus modulating the incoming flux at a frequency faster than the fluctuation between the on-source and off-source positions and computing the difference of the two frames results in a background free observation. To compensate for the background residual due to the difference in the optical path between the on- and off-source orientations, the telescope is also nodded, which means that it oscillates between two different pointing positions. Since the time-scale associated to the background residual is longer than the background fluctuations, nodding occurs at frequency lower than for chopping [19].

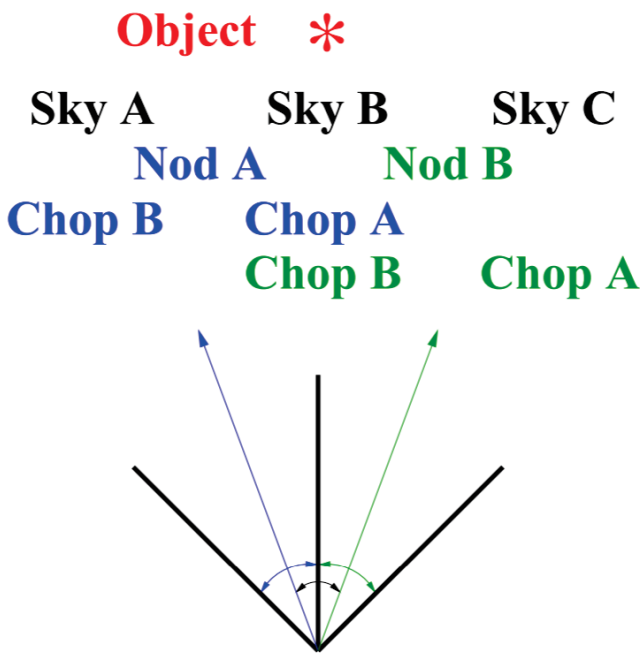

Figure 3.6: Schematisation of chopping and nodding for background removal in MIR observations. Both the angles of chopping and nodding are exaggerated for a better understanding of the diagram [36].

A simplified demonstration of the effectiveness of chopping and nodding for background removal taken from [36] is given below. With reference to Figure 3.6, at the time t_A the telescope is pointing towards the nod position $Nod\,A$ and is chopping between $Nod\,A\,(Chop\,A)$ and $Nod\,A\,(Chop\,B)$. Similarly, at the time t_B the telescopes is aligned with $Nod\,B$ and is chopping between $Nod\,B\,(Chop\,A)$ and $Nod\,B\,(Chop\,B)$. For the sake of simplicity, it is assumed that source, sky and telescope signals are constant with time. Therefore, the signals at the nod position $Nod\,A$ and $Nod\,B$ are

$$Nod\,A = Nod\,A\,(Chop\,A) - Nod\,A\,(Chop\,B) = Source + Sky\,B + Tel\,A - (Sky\,A + Tel\,B) \tag{3.1}$$

$$Nod\,B = Nod\,B\,(Chop\,A) - Nod\,B\,(Chop\,B) = Sky\,C + Tel\,A - (Source + Sky\,B + Tel\,B) \tag{3.2}$$

where $Tel\,A$ and $Tel\,B$ are the contribution of the telescope emission as seen respectively in the chop positions $Chop\,A$ and $Chop\,B$. The signal is then computed taking the difference between Equations (3.1) and (3.2), so that

$$Signal = Nod\,A - Nod\,B = 2\,Source + 2\,Sky\,B - Sky\,A - Sky\,C = 2\,Source \tag{3.3}$$

The last equality holds if $Sky\,B = (Sky\,A + Sky\,C)/2$, an assumptions close to reality considering that usually chop and nod angles are small, and therefore positions A, B and C are close to each other. It is emphasised once again that the one presented here is just a simplified demonstration of the chopping and nodding technique, since in reality it is necessary to take into account the variations with time of the signal, especially the thermal emission of sky and telescope. A more extensive analysis is reported in [36].

3.2.2. Chopping with the secondary mirror

Chopping at the VLT is done by tilting the secondary mirror of the UTs at a frequency between 0.1 and 5 Hz [37]. The results of the on-sky tests made at the UT3 are reported in Figure 3.7, where the error bars and the grey shaded area reflect the 1σ uncertainties and are derived from the noise variance. The star symbol is referred to the sensitivity of the old DRS detector at the typical chop frequency of $0.25\,Hz$ of the secondary mirror. The white squares represents the sensitivity of the AQUARIUS detector, which at $0.25\,Hz$ is approximately twice as large as the one of the DRS detector, and thus worse than expected [25]. At higher chop frequencies the sensitivity is enhanced, especially if also shift-and-add techniques are used to improve the detector performance, as shown by the black squares. In particular, the sensitivity of both detectors is approximately equal at a frequency of 2-3 Hz if no additional correction methods are used. The results obtained estimating the noise from the background level, represented by the grey circles, are the closest to the theoretical sensitivity for diffraction-limited observations. The graphs also includes the BLIP sensitivity for a seeing of $0.5''$ [31].

The drift-scanning technique was also tested with good results, as shown by the grey diamonds on the bottom right part of the graph [31]. It consists in modulating the incident signal by moving the field across the detector so that the source is observed by multiple pixels. To break the correlation between adjacent pixels, the controlled motion of the source has to occur at a speed faster than the ELFN time-scale. Considering that most of the pixels receive only signal from off-source area of the observed field, the background is calculated as the median of the pixel value of all the captured frames, and once that it is removed the consecutive frames can be aligned and then co-added [38]. Despite its effectiveness in suppressing the ELFN, the drift-scanning technique is not a preferable solution because it would require a modification of the telescope control system [31].

The main advantage of chopping with the secondary mirror is that it could reduce the loss in the observing efficiency of the Dicke-switch, whose value is limited to only 50% (see Sections 3.2.3 and 3.3) [6]. However, since as part of the upgrade VISIR will be moved from the UT3 to the UT4 for observations using the AO facilities, chopping and nodding for background removal and ELFN mitigation had to be integrated with AO operations [6]. Chopping at a frequency of $10\,Hz$ during AO operations was successfully tested in April 2018, and therefore it represents the baseline for the observing campaign of the NEAR experiment.

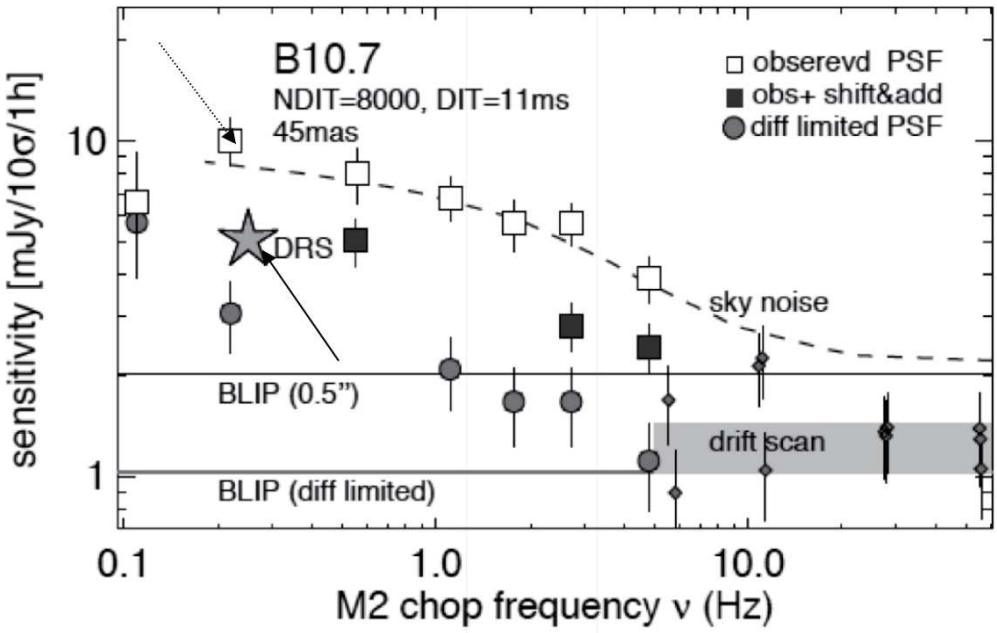

Figure 3.7: Variation of the AQUARIUS detector sensitivity as a function of the chop frequency of the secondary mirror at the UT3 [25].

3.2.3. Dicke-switch concept

Besides chopping with the secondary mirror, a chopper system based on the Dicke-switch concept is an available options to mitigate the ELFN of the AQUARIUS detector for the NEAR experiment [6]. Its name comes from the Dicke-radiometer, invented by Robert Henry Dicke during War World II to measure the atmospheric absorption that was limiting the radar resolution. At a later time, he used the same radiometer to evaluate the thermal radiation from the Moon and to prove that the cosmic background radiation at 1-1.5 cm is less than $20\,K$ [39, 40]. The Dicke-radiometer is basically a classic radiometer with a switch to regularly alternate the input of a receiver between the radiation of a source at an unknown temperature T_1 and a source at a known temperature T_2, which is controlled in such a way to match T_1 [41].

The Dicke-switch chopper system used for MIR applications is based on an analogous concept, and it has already been used for Solar spectroscopy [42, 43]. It consists of a mirror which regularly reflects on the detector the IR emission of a blackbody, whose temperature is regulated so that its emission match the background flux, sum of sky and telescope emissions [6]. For VISIR, the main advantage of this system is that it is located behind the deformable secondary mirror of the UT4, avoiding any interference with the AO operations. Yet, it has a 50% observing efficiency, since for half of the chop cycle the instruments receives the signal from the blackbody.

During phase A analysis of the project, a test was done in order to assess the performance of a Dicke-switch chopper system depending on the offset between blackbody and background fluxes. A schematisation of the test set-up is given in Figure 3.8. The AQUARIUS detector received alternatively the infrared radiation from a blackbody and a chopper wheel, with flux levels of $\sim 1.6 \cdot 10^6\, e^-$, five times higher then during typical VISIR observations. The tests was repeated for different temperatures of the blackbody between 20℃ and 21℃, and for each test a series of 2000 frames was captured with a detector integration time of $4\,ms$ at a $10\,Hz$ chop frequency [6]. The best match between the blackbody and the chopper wheel flux occurred for a blackbody temperature of 20.8℃. The related results are reported in Figure 3.9, in which different frames recorded in burst mode, from 1 to 1000, have been added together to simulate different chop frequency between 0.125 and 125 Hz. As expected, the ELFN was reduced at higher frequency.

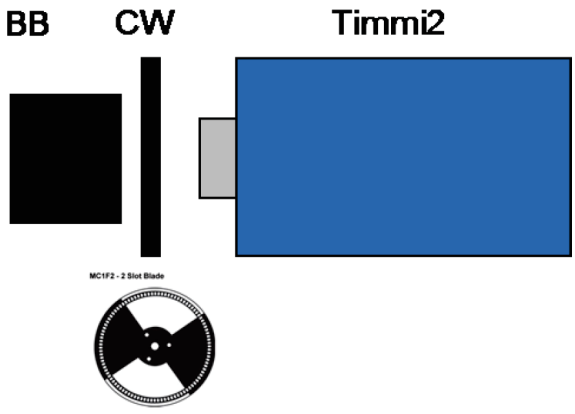

Figure 3.8: Laboratory test set-up used to assess the ability of the Dicke-switch chopper system to mitigate the ELFN of the AQUARIUS detector during the phase-A analysis [6].

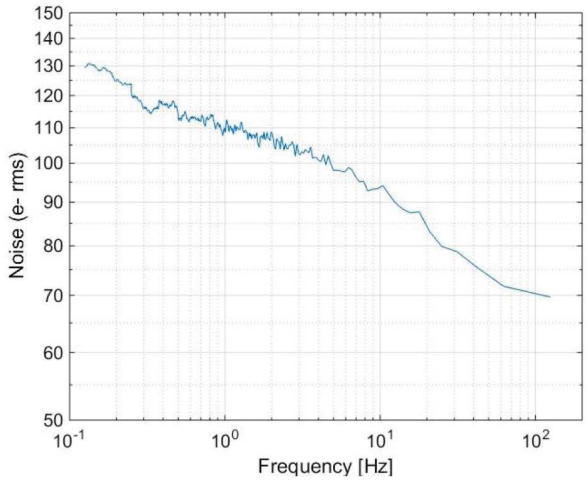

Figure 3.9: Results of the test performed during the phase-A analysis to assess the effectiveness of the ELFN mitigation with the Dicke-switch chopper system, derived with pseudo-chopping from frames recorded in burst mode [6].

A second test was done to determine the ability of the system to mitigate the ELFN even for a larger offset between blackbody and chopper wheel fluxes. The blackbody was stabilised at a temperature of 20°C, which corresponds to a flux offset of approximately 200 ADU, but also a theoretical perfect match, realised measuring only the radiation of the blackbody with no physical chopping, was considered. The chop frequency was set at 10 Hz. The on- and off-source frames were distinguished based on their flux level. For each chop cycle, the average flux level over the whole sequence of on- and off-source frames were subtracted from the single frames, similarly to a nodding correction. After that, the on-source frames were subtracted from the subsequent off-source frames. The same procedure was repeated also for the ideal case. The average of the chopping corrected frames gave a standard deviation of the incident flux of $\sim 1.0045\,ADU$ and $\sim 1.0082\,ADU$ for the non-ideal and ideal case respectively. This result demonstrates the ability of the Dicke-switch chopper system to suppress the ELFN even for large offset in the flux levels, which therefore has been selected as possible mitigation method for the NEAR experiment [6].

3.3. Description of the VOU design

A brief overview of the VFM has already been given in Section 2.3. The next sections complete the description of its design presenting in details the VOU, illustrated in Figure 3.10. Its main function is to suppress the ELFN of the AQUARIUS detector. To do so, three main components are needed: vacuum housing, chopper mechanism and blackbody unit (BBU) [28].

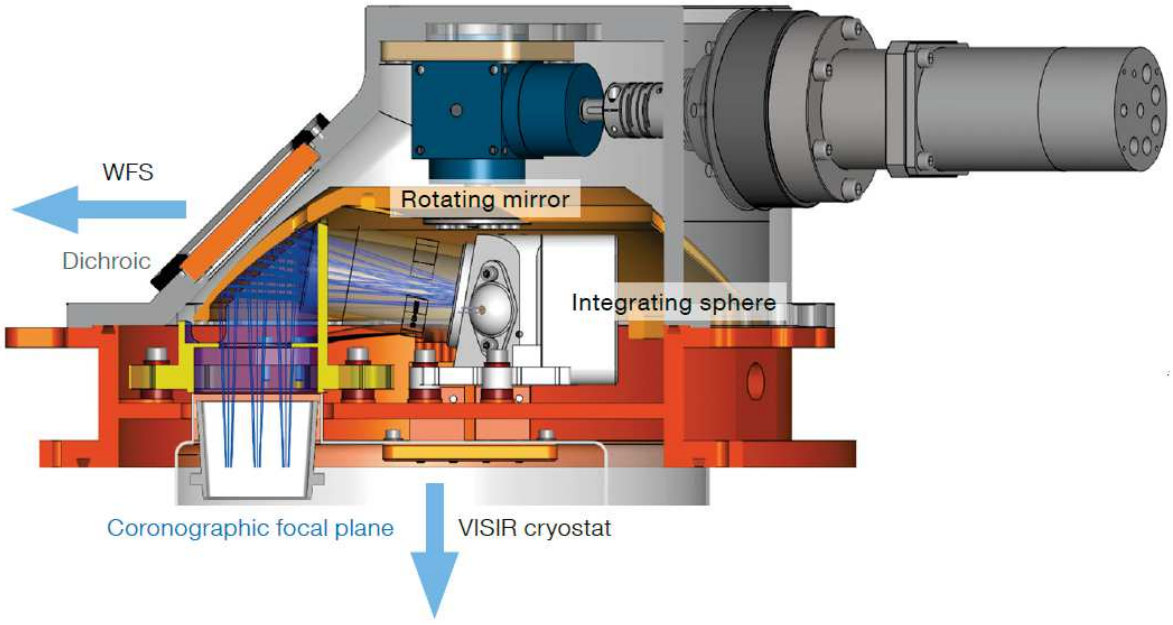

Figure 3.10: Internal details of the VOU assembly. The vacuum housing hosts the Dicke-switch chopper system, which comprises a D-shape rotating mirror and the BBU for the suppression of background level and ELFN. The ZnSe dichroic window, coated to transmit between 10 and 12.5 μm, reflects light at optical wavelength towards the WFS for real-time correction of atmospheric fluctuations with AO. When the D-shape mirror is in open position, the beam coming from the telescope is able to reach the detector, while in the closed position the detector receives the signal from the BBU, whose temperature is regulated so that its radiation matches the background level typical at Paranal [5].

3.3.1. Vacuum housing

The vacuum housing of Figure 3.11 provides low vacuum conditions to chopper mechanism and BBU. Viton O-rings are placed at all the vacuum interfaces for proper sealing. The vacuum housing provides also all the required electrical connections thanks to the implementation of two vacuum feedthroughs: the upper one, based on ferrofluidics, allows to leave the actuator of the chopper mechanism outside the vacuum housing, while the lower one is used to connect the wire of the BBU sensors. As already explained in Section 2.3, the coated ZnSe window, tilted at 45° with respect to the telescope beam, acts as a dichroic filter and is secured to the housing wall by a metal ring [28].

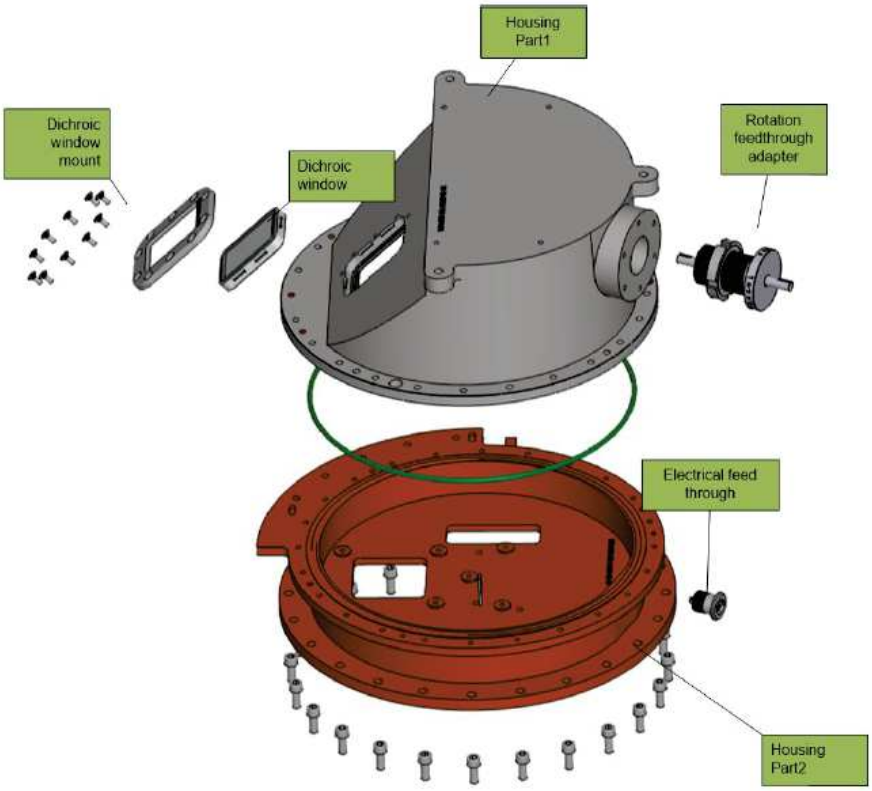

Figure 3.11: Exploded view of the vacuum housing [28].

3.3.2. Chopper mechanism

The complete chopper mechanism is shown in Figure 3.12. The rotating mirror, made of aluminium and gold coated, is a D-shape parabolic mirror with a radius of curvature of 119.5 mm and a diameter of 260 mm. It is light-weighted in order to reduce the torque demanded from the motor and is dynamically balanced to diminish vibrations. The mirror, extended for 180° and opened on the other side, periodically reflects to the VISIR cold stops the IR radiation of a blackbody for the real time simulation of the sky background, depending on whether it faces or not the output port of the BBU. The rotatory motion is transferred to the chopper mirror through a spiral bevel gearbox, which required few modifications before the implementation in the VOU, in particular grease and bearings for vacuum applications. With respect to spur gears, spiral bevel gears have the advantage that noise and vibrations are reduced. A rotation coupling connects the spiral bevel gearbox to the vacuum ferrofluidic feedthrough mounted on the housing, allowing to compensate errors deriving from manufacturing and alignment processes. For the same reason, the motor is connected from the outside to the feedthrough using another rotation coupling [28].

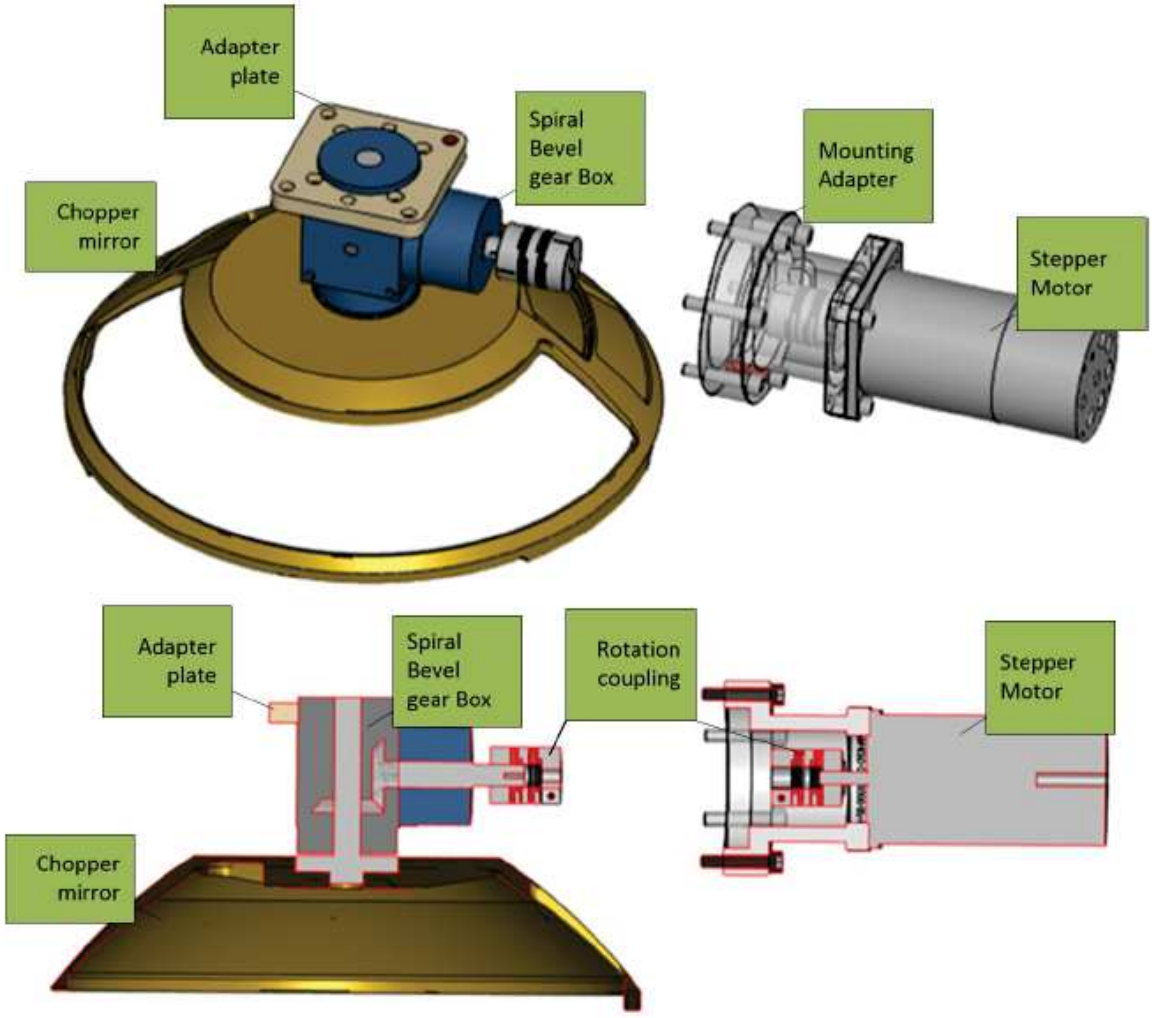

Figure 3.12: Detailed view of the D-shape chopper mirror and of the mechanism for its actuation. [28].

3.3.3. Blackbody unit

The main function of the BBU illustrated in Figures 3.13 and 3.14 is to provide a lambertian illumination over the VISIR focal plane for the real time simulation of background sky and telescope emissions. The IR radiation is emitted by an aluminium source and is reflected by a gold coated integrating sphere having a radius of $60\,mm$ towards its output port. Two Pt100 sensor are used to heat the IR source in a closed-loop: one provides heating to the source, while the other one measures its temperature. A fast cooling of the IR source is possible due to the high thermal connectivity between the blackbody housing and the IR source itself. Two baffles have been included for the shielding from stray light. The baffle on the sphere output port blocks the stray light coming from the integrating sphere, while the one placed after the chopper mirror blocks the stray light produced by the warm components inside the vacuum housing. Their inner and outer surfaces are respectively black and gold coated. The BBU, except for the IR source, has an operating temperature of $\sim 128\,K$ to reduce the presence of unwanted stray light and is cooled down by copper thermal straps connected to the $\sim 40\,K$ cold shield of VISIR. Considering the high temperature difference between the BBU and the vacuum housing, thermal blades have been implemented at their interface for compensation of thermal expansion[28].

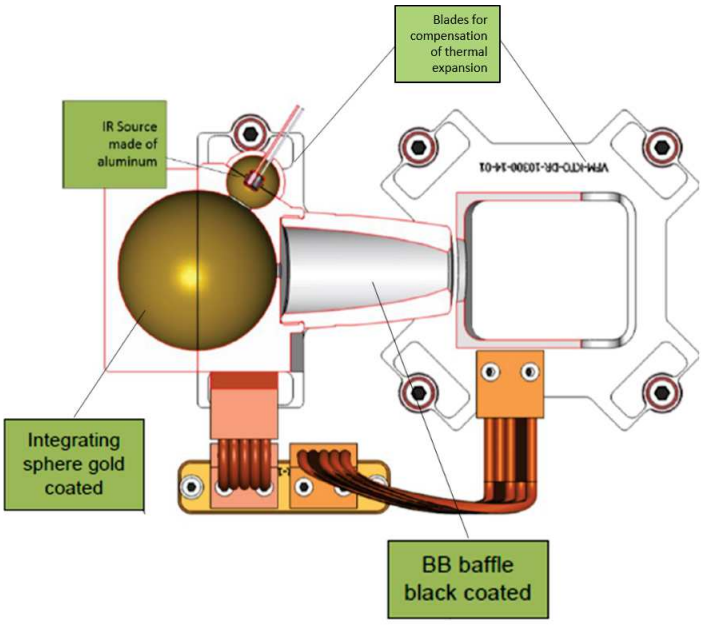

Figure 3.13: Section of the top view of the BBU assembly, adapted from [28]. The copper thermal straps are connected to the $\sim 40\,K$ cold shield of VISIR to cool the BBU down to $\sim 128\,K$.

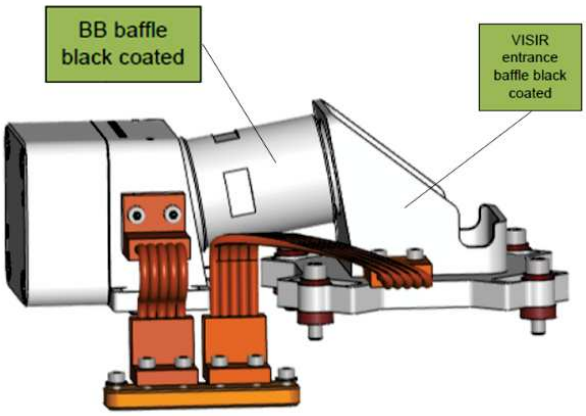

Figure 3.14: Blackbody unit assembly, adapted from [28]. The copper thermal straps are connected to the $\sim 40\,K$ cold shield of VISIR to cool the BBU down to $\sim 128\,K$.

3.4. Overview on the upgrade of TIMMI2 to include the thermo-mechanical interface for the VOU

TIMMI2 was recently upgraded in order to include the thermo-mechanical interface required for the implementation of the VOU for the acceptance tests. It was decided to include in this chapter a description of this thermo-mechanical interface since it limits the achievable flux levels of the system, as described more in details in Section 3.5.4.

The design process was based on some preliminary considerations:

- It was necessary to ensure that the thermo-mechanical interface is able to guarantee to the VOU the required vacuum and thermal level using the same vacuum pumps and cooling system of TIMMI2, since the VOU itself does not have a dedicated pump nor a cooling system, as already described in Section 3.3

- While the telescope beam enters and leaves the VOU vertically (Figure 3.10), the entrance window of TIMMI2 requires a horizontal beam (Figure 2.9). It was therefore decided to modify the front flange of TIMMI2 in order to be able to mount the VOU directly on it (vertically)
- Because the front flange presents numerous ribbon-like structures disposed radially at regular intervals (Figure 2.9), a new plate was clearly necessary to seal the entire system using O-rings, which need to be located in dedicated grooves and compressed when two sealing surfaces are closed, and thus cannot be applied to hollow surfaces similarly to the front flange
- With respect to the thermal connection between the cold structure of the instrument and the BBU, at first it was considered to pass the thermal straps through the entrance window of the TIMMI2 front flange (Figure 2.9), which in any case would have had to be removed as its function is replaced by the dichroic window of the VOU (Figure 3.10). However, due to the limited space available, it was decided to pass the thermal connections from the centre of the front flange, which means that a hole was needed on both the front flange itself and the new interface plate to allow the passage of the copper thermal straps.

All the considerations above resulted in the modification of the existing front flange and the design and manufacturing of few additional components. A CAD model of the thermo-mechanical interface between TIMMI2 and the VOU is reported in Figure 3.15. A smooth interface plate, i.e. without the ribbon like structures similar to the ones of the TIMMI2 front flange, provides mechanical interface and also sealing for low vacuum conditions to the entire VOU. A copper thermal interface is placed on the fibre glass laminate spider structure and is fixed with two screws to the radiation shield, which has a temperature of about $90\,K$ when the VOU is mounted. An S-shape copper bracket extend the thermal interface in order to easily mount the copper thermal straps to cool down the BBU of the VOU.

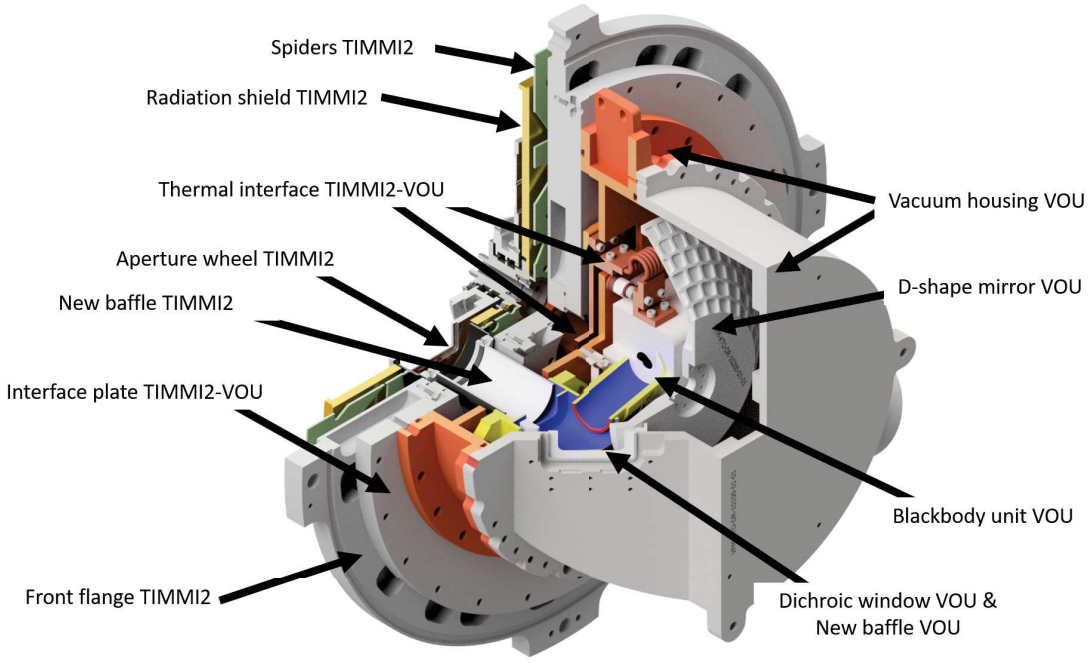

Figure 3.15: CAD model of the VOU integrated on the front flange of TIMMI2. The three-quarter section view shows the details of the different components and subsystems. The CAD models of the VOU assembly were realised by Kampf Telescope Optics GmbH (KTO), contractor responsible for the design of the VFM.

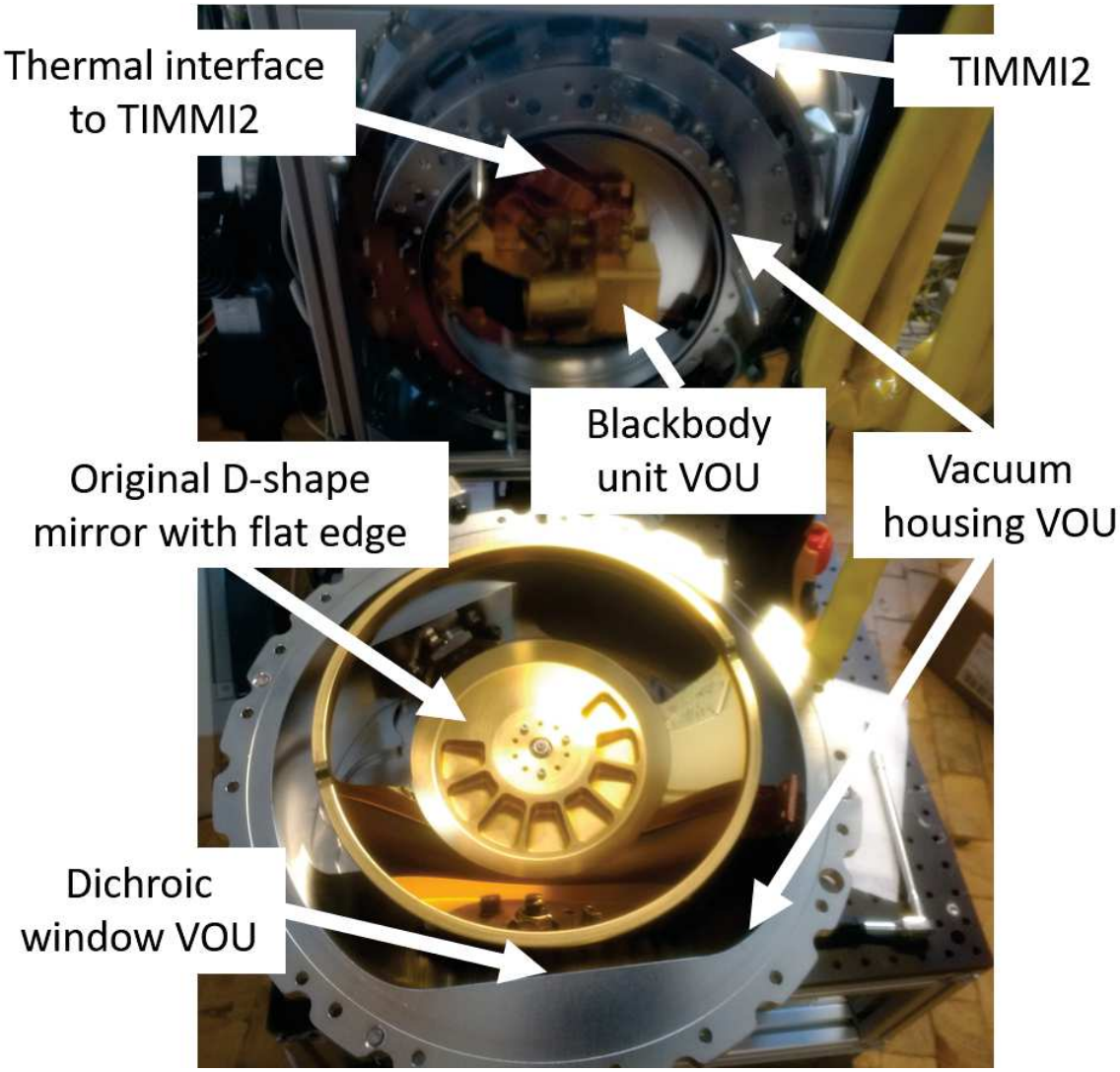

Figure 3.16: VOU during the integration on TIMMI2.

The real hardware implemented with TIMMI2 is shown in Figure 3.16. Section 3.5.4 describes additional modifications of the thermal interface based on radiometric tests and needed in order to provide the required flux level to the BBU to simulate the background emission typical at the VLT.

The mechanical interface of the VOU with the test facility described above does not allow the D-shape mirror to produce a focused image at the level of the TIMMI2 cold focal plane. This is illustrated in Figure 3.17, which shows that the image plane is defocused of about $32\,mm$. However, since the thermal radiation of the BBU is actually a flat field, this does not cause any problem for the final validation of the VOU.

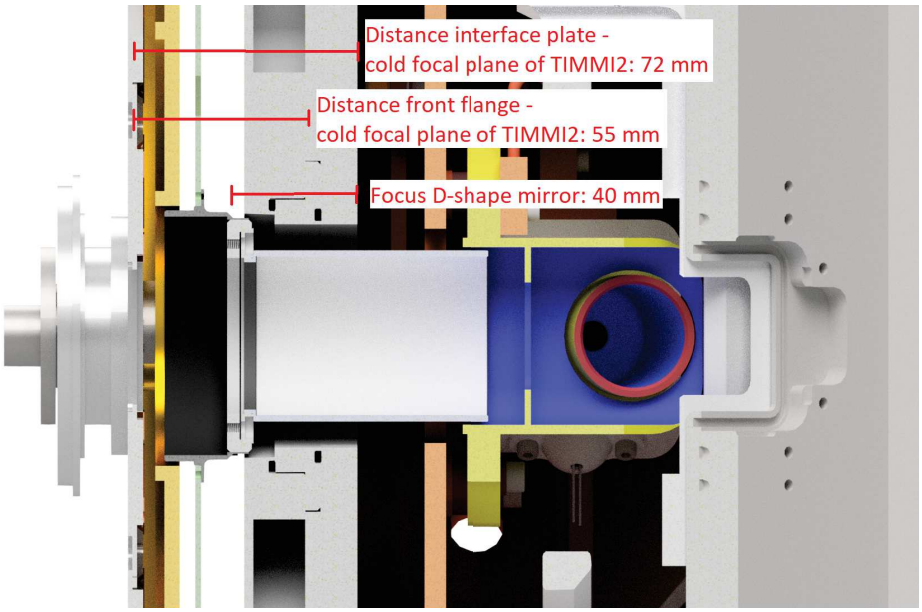

Figure 3.17: CAD model of the VOU integrated on the front flange of TIMMI2. This cross section highlights the fact that the imaging plane of the D-shape mirror is defocused with respect to the cold focal plane of TIMMI2. The CAD models of the VOU assembly were realised by KTO, contractor responsible for the design of the VFM.

3.5. Radiometric tests for the characterisation of internal blackbody unit and artificial sky

This section describes in details the tests performed to assess the radiometric flux level needed to validate the Dicke-switch chopper system. Referring to Sections 3.2.3 and 3.3, the thermal radiation of two different blackbodies had to be characterised: the one of the so called artificial sky, which is basically a laboratory representation of the background level typical at Paranal, and the one emitted by the internal BBU of the VOU. After an introduction on the typical background flux level at Paranal, which sets the main radiometric requirement for the VOU, characterisations of artificial sky and internal BBU are presented separately. This section also discusses about the parasitic light effects that cause a non-flatness of the FoV of the detector and required the implementation of a new design of the D-shape mirror of the Dicke-switch.

For all the tests performed, TIMMI2 was used in a nominal configuration to avoid vignetting the FoV of the VOU. More details are given in Table 3.1. Moreover, all the radiometric measurements were done with the AQUARIUS detector in low gain mode. This choice was based on the fact that for the radiometric tests the flux levels of artificial sky and internal BBU were normalised with respect to the background level of the laboratory, therefore to avoid non-linear response or saturation of the detector the low gain mode was preferred. The detector was always used in its linear response regime between 15 000 and 40 000 $ADUs$ [33].

Table 3.1: Nominal configuration of TIMMI2 used for all the tests performed.

Nominal TIMMI2 Configuration	
Aperture	$0.3''/pixel$
Filter	$10.4 \pm 0.5\,\mu m$
Lens	N-band, $0.3''/pixel$

3.5.1. Background radiance and radiometric requirement

A model of the combined sky and telescope thermal radiation typical at the VLT was already reported in Figure 2.4. Based on that, the following technical system requirement (TSRQ) shall be satisfied in terms of radiometric flux level produced by the BBU:

> **TSRQ17:** The blackbody unit must feed the VISIR beam in the same way as the sky from the telescope and with a spatially flat intensity distribution at a flux level as close as possible to that of the sky seen through the telescope mirrors (∼10% of 280 K blackbody) and within the field of view of VISIR as close as possible to a Lambertian radiator [44].

While during the actual observations at the VLT the flux level produced by the BBU will be compared with the combined sky and telescope thermal radiation, during the acceptance tests this was done with respect to the thermal radiation of the laboratory, assumed to be a blackbody emitting at about 295 K (see Section 3.2.3). In order to scale the required value of the background flux level, it shall be considered that the spectral radiance of a blackbody, expressed in $Wm^{-2}\,Hz^{-1}\,sr{-}1$, is described by the Planck's radiation law as

$$B(\nu, T) = \frac{2h\nu^3}{c^2}\,\frac{1}{e^{\frac{h\nu}{kT}} - 1}$$

in which h is the Planck's constant, ν the frequency, c the speed of light in vacuum and k the Boltzmann's constant. Since $c = \lambda\nu$, where λ is the wavelength, the normalised radiation of a blackbody at a variable temperature T with respect to the one of a blackbody emitting at a reference temperature T_{ref} is

$$B_{norm}(\lambda, T) = (e^{\frac{hc}{k\lambda T_{ref}}} - 1)/(e^{\frac{hc}{k\lambda T}} - 1) \tag{3.4}$$

Figure 3.18 shows two curves plotted using Equation (3.4) normalised with respect to blackbodies at a reference temperature T_{ref} of 280 K and 295 K, which, as mentioned above, corresponds to the estimated background radiation at Paranal and in the laboratory. The graph shows that in the laboratory BBU and artificial sky shall produce ∼ 7.8% of the thermal radiation of the laboratory itself.

3.5.2. Artificial sky flux level

A cold blackbody had to be used for the so called artificial sky, needed to reproduce in the laboratory the typical background level at Paranal, sum of sky and telescope emission.

Initially, it was considered to use a layer of thick black carton placed on the bottom of a container, cool it down with liquid nitrogen (LN_2), which has a temperature of about 77 K at ambient pressure, and reflect its thermal emission towards TIMMI2 by using a folding mirror and a germanium (Ge) lens. In terms of radiometric level, this solution provided a thermal emission of about ∼ 8.5% of the one produced by the laboratory, which even though was higher than the required ∼ 7.8% reported in Figure 3.18, it was actually acceptable considering that the minimum emission of the BBU was about at the same level, as discussed later in Section 3.5.4. However, this solution was discarded due to its instability. Indeed, once in the container, the LN_2 starts to boil and a cold layer of gas forms on its surface, making the generated signal varying faster than the background emission at the VLT, where, as reported in Section 3.2.1 and Figure 3.7, the changes occur on a timescale of few seconds. This can be seen in Figure 3.19, which shows the variation of the flux level produced by the LN_2 normalised to the thermal radiation of the laboratory. To prove that these fluctuations are in fact caused by the LN_2, Figures 3.20 and 3.21 report the dark and laboratory flux levels, both normalised to the first frame of the respective recorded sequence.

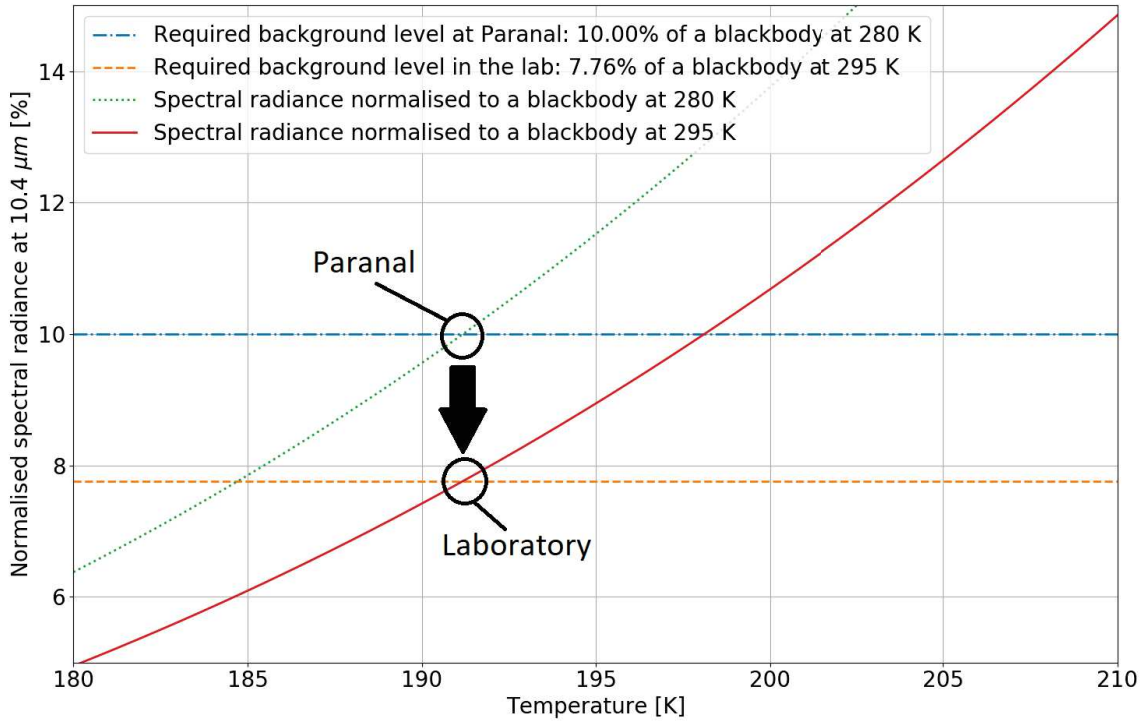

Figure 3.18: Spectral radiance at $10.4\,\mu m$ for different blackbody temperatures normalised with respect to the spectral radiance of a two blackbodies emitting at $280\,K$ and $295\,K$. The graph shows the required flux level of artificial sky and BBU of the VOU at the VLT and in the laboratory in order to match the one of the background.

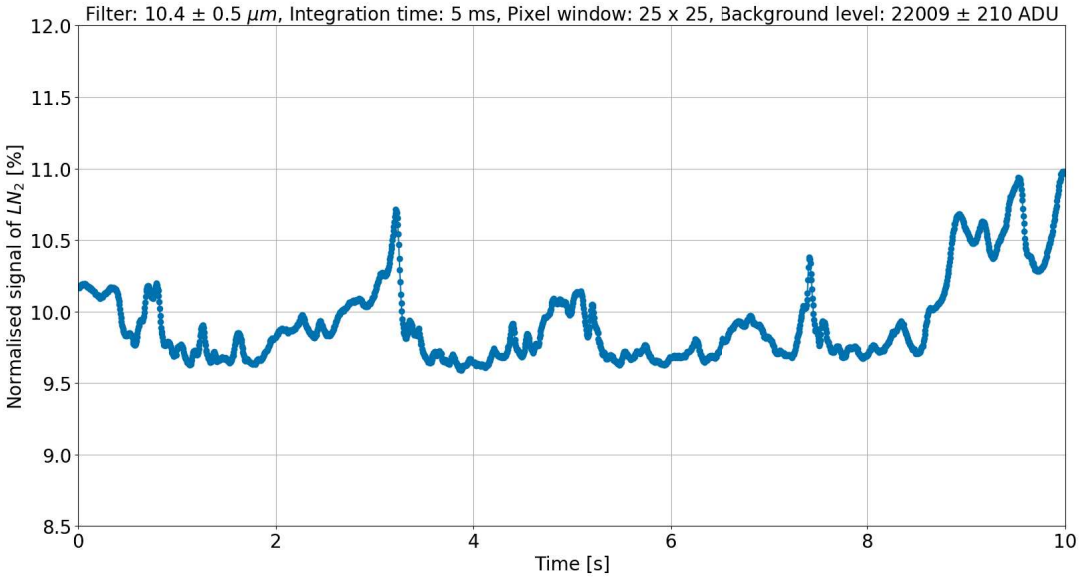

Figure 3.19: Variation of the flux level produced by the LN_2 normalised to the thermal radiation of the laboratory. The curve corresponds to the average signal value calculated at different time and was derived from a sequence of 2000 frames, each having $5\,ms$ of integration time. All frames were dark corrected, and only a square window of 25×25 pixels was considered. The background level was calculated by averaging 2000 frames, each having $5\,ms$ of integration time, while for the dark level 100 frames were averaged.

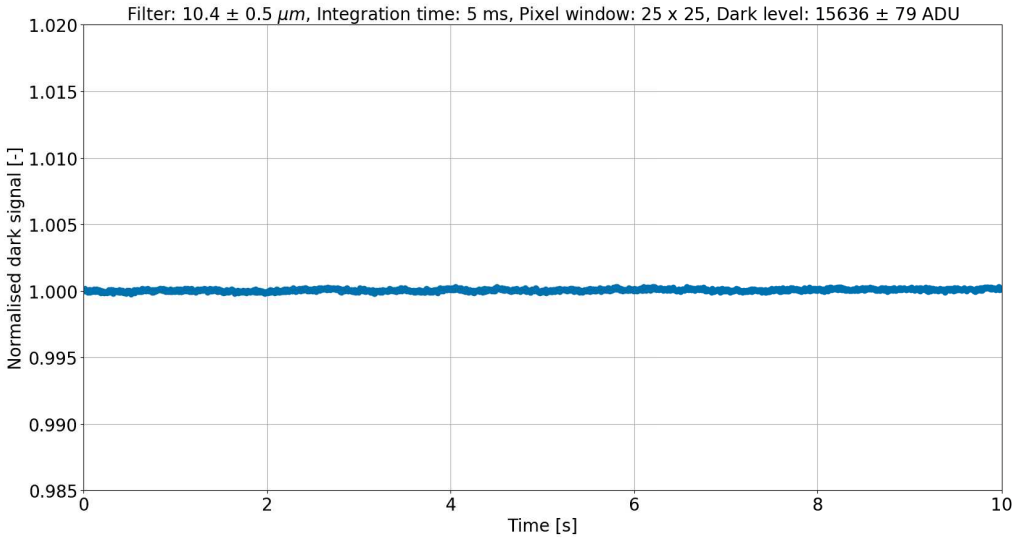

Figure 3.20: Variation of the dark level measured by the detector. The curve corresponds to the average signal value calculated at different time and was derived from a sequence of 2000 frames, each having $5\,ms$ of integration time, for which only a square window of 25×25 pixels was considered. Each data point of the graph was normalised with respect to the first frame of the sequence.

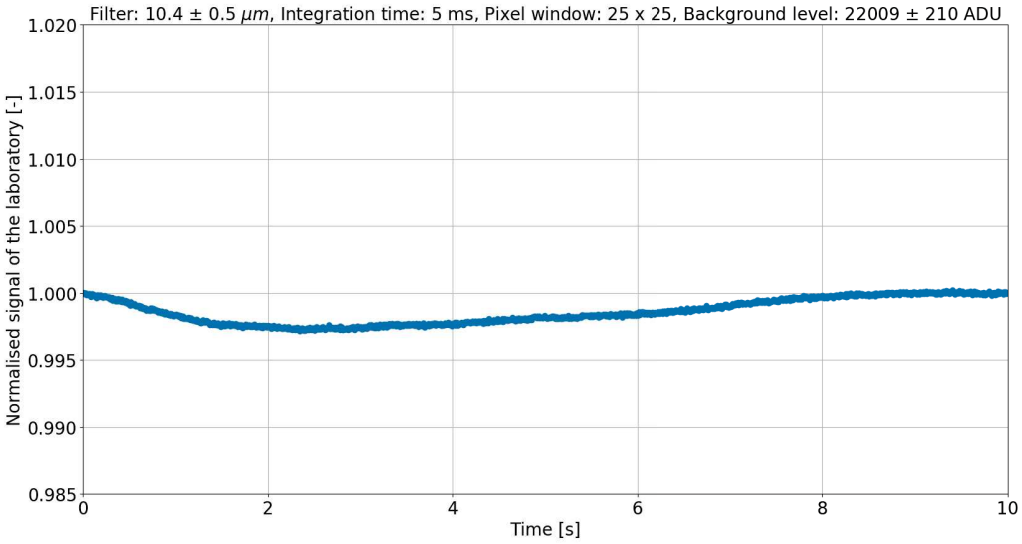

Figure 3.21: Variation of the flux level produced by the laboratory. The curve corresponds to the average signal value calculated at different time and was derived from a sequence of 2000 frames, each having $5\,ms$ of integration time. All frames were dark corrected, and only a square window of 25×25 pixels was considered. Each data point of the graph was normalised with respect to the first frame of the sequence. The dark level was calculated by averaging 100 frames.

While for LN_2 the flux level shows variation of more than 1% in $\sim 1\,s$, both dark and background levels are more stable, with the latter one varying slower than LN_2. In Section 3.5.6 it is shown that for the BBU a variation of 1-1.5% of its emitted flux level corresponds to a change of its temperature between 10 and 20 K. As already mentioned in Section 3.2.3, the performance of the Dicke-switch shall be assessed also in terms of its ability to mitigate the ELFN when there is an offset between the sky background and the BBU emissions. For this reason, it was therefore decided to keep one of the two considered flux level stable, in this case the artificial sky, varying only the one of the BBU in a controlled way.

Based on the need to have a stable radiometric source colder than the laboratory, it was decided to place a flat mirror in front of the dichroic window of the VOU to make TIMMI2 looking back into itself taking advantage of the fact that it is cooled down to cryogenic temperatures and it is very stable over long periods of time, as shown in Table 3.2.

With this solution, shown in Figure 3.22, the signal impinging on the detector was formed by different contributions: twice the emission of the dichroic window, emission of the flat mirror, emission coming from TIMMI2 and reflected back by the flat mirror and also some residual parasitic light, discussed more in details in Section 3.5.3. The minimum flux level achievable in this configuration was $\sim 7\%$ of the laboratory emission. By placing in front of the dichroic window some plastic foils mounted on a frame, it was also possible to increase the signal in a controlled way, as shown later in Section 3.5.6. Figure 3.23 shows the stability of the artificial sky flux level over a period of about 10 minutes.

Table 3.2: Average temperature of the subsystems of TIMMI2 calculated over a period of five days. For each set of data, also the one standard deviation value is included.

Temperatures TIMMI2 [K]	
Structure 1	60.34 ± 0.20
Structure 2	66.08 ± 0.22
Lens wheel	56.68 ± 0.15
Collimator	59.26 ± 0.21
Cold stop	59.31 ± 0.18
Main shield	90.52 ± 0.48
Cold head stg.1	41.39 ± 0.08

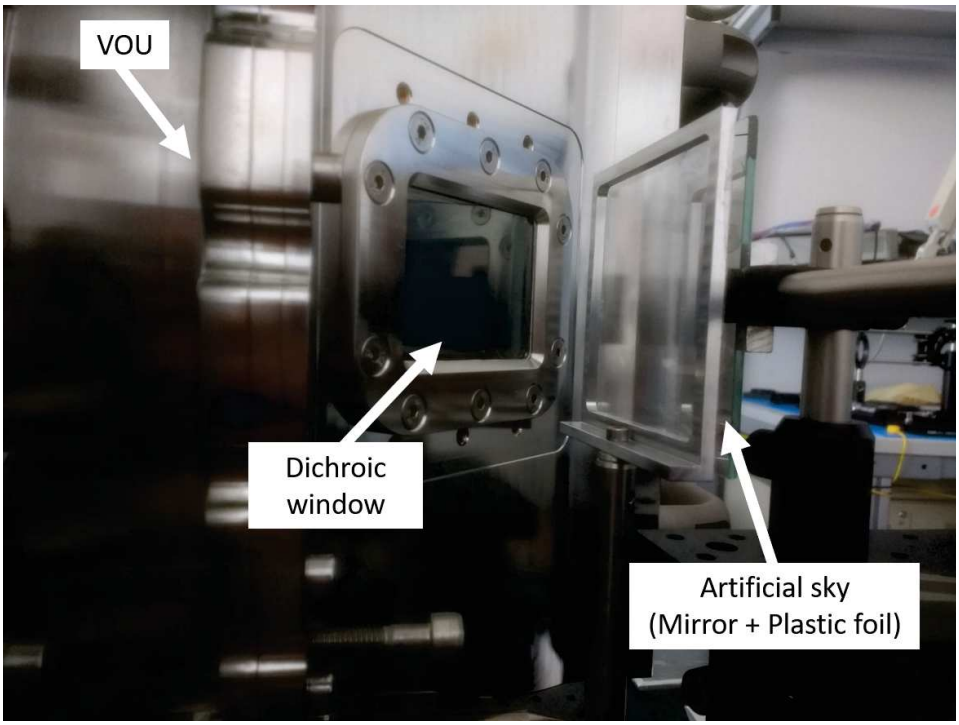

Figure 3.22: Artificial sky used to reproduce in the laboratory the background level typical at the VLT.

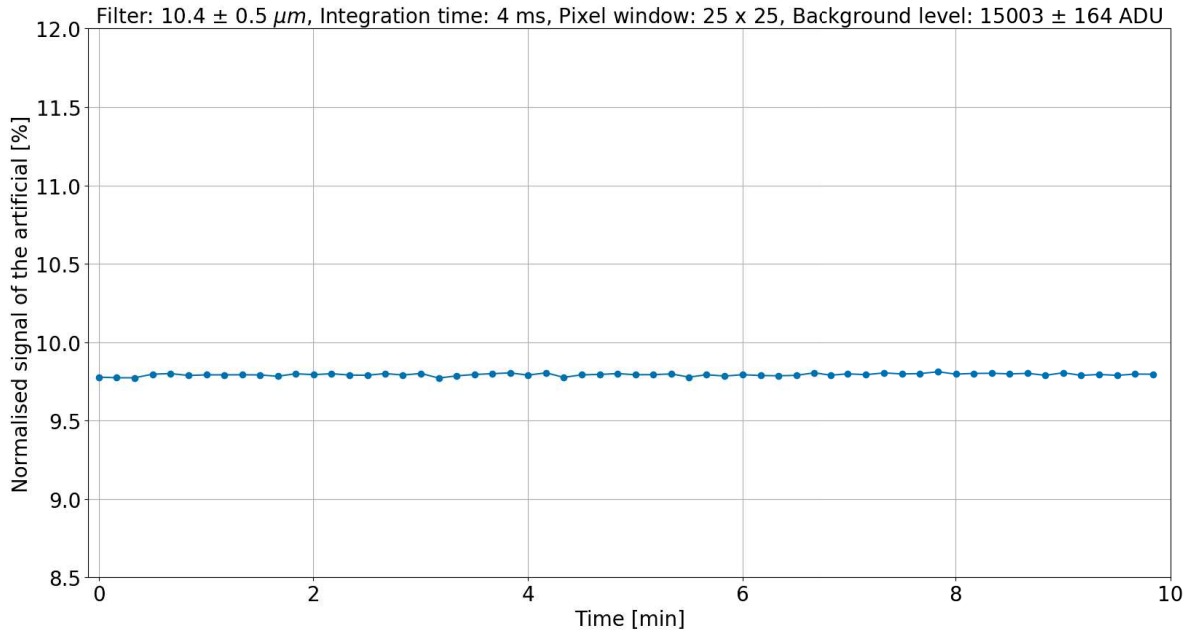

Figure 3.23: Variation of the flux level produced by the artificial sky in the configuration with a single layer of plastic foil normalised to the thermal radiation of the laboratory. The curve corresponds to the average signal value calculated at different time and was derived from a sequence of 60 images, recorded after averaging 250 frames each having $4\,ms$ of integration time. All frames were dark corrected, and only a square window of 25×25 pixels was considered. Both background and dark level were recorded after averaging 250 frames, each having $4\,ms$ integration time.

3.5.3. Parasitic light caused by reflections of internal and external thermal radiation

During the first characterisation of the artificial sky, it was noted that the signal impinging on the detector with the D-shape mirror in open position, i.e. not reflecting the emission from the BBU, but allowing the one coming from outside the VOU to reach the detector, the field was uneven. Figure 3.24 shows a view of the detector when looking into a container filled with LN_2 and a linecut of this uneven field to show the intensity variation, normalised to the background flux level of the laboratory. The fact that the non-flatness of the field was $\sim 3\%$ of the laboratory flux level suggested that this could have actually been caused by some background emissions reflected towards the detector by the back side of the dichroic window, which indeed has a reflectivity of $\sim 3\%$ at $10.4\,\mu m$. Straylight simulations made by KTO confirmed that the non-flatness of the field was caused by internal and external background thermal radiation, produced respectively by the warm components of the VOU and the laboratory, reflected by the D-shape mirror onto the backside of the dichroic window and then towards the detector. This is schematised in Figure 3.25.

Two new modifications were therefore needed to mitigate these effects:

- A new D-shape mirror with a sharp edge was manufactured to minimise the reflection of the external radiation
- A new baffle was added at the level of the dichroic window in order to block the internal radiation reflected by the top, curved edge of the D-shape mirror.

An extension baffle was also added between the entrance window of TIMMI2 and the baffle of the BBU in order to reduce straylight effects due to light reflections between the lower part of the VOU vacuum housing and the interface plate of TIMMI2 (see Figure 3.15).

Figures 3.26 shows the field produced by the artificial sky described in Section 3.5.2 after the implementation of the new baffle and D-shape mirror and a linecut of the field to show the residual parasitic light. The non-flatness of the sky was reduced from the initial 3-3.5% to about 1-1.5%.

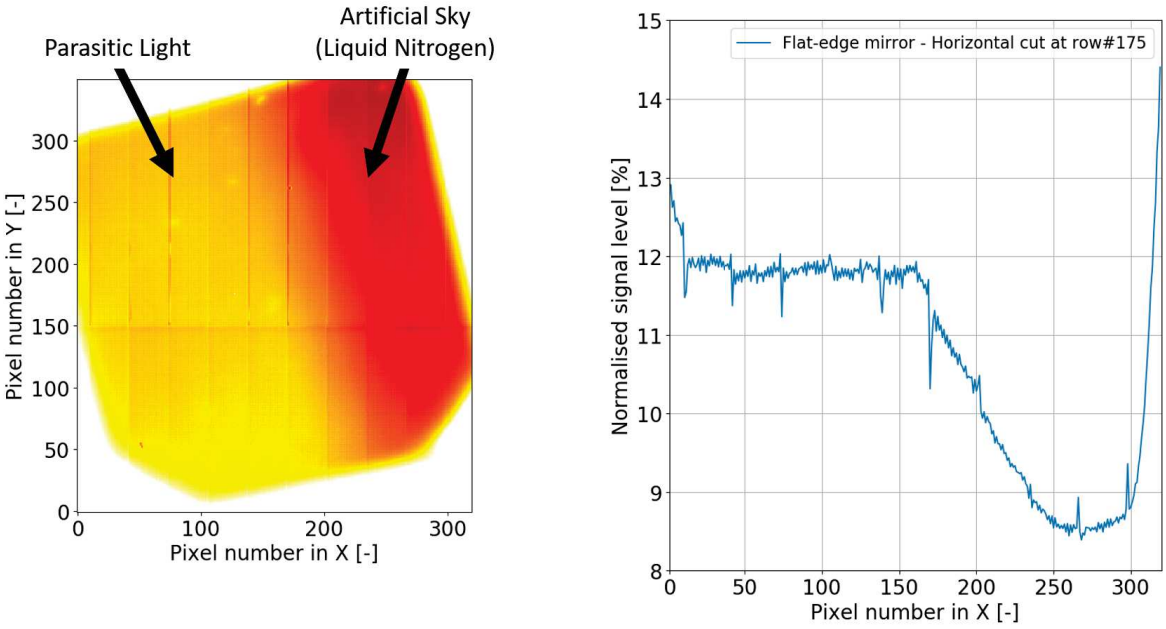

Figure 3.24: Left: view of the detector when looking into a container filled with LN_2. Right: linecut of the uneven field seen by the detector when looking into a container filled with LN_2 normalised to the thermal radiation of the laboratory. Both background level and artificial sky images were dark corrected, and all frames were recorded after averaging 100 frames, each having 10 ms integration time. The images were recorded in June 2018.

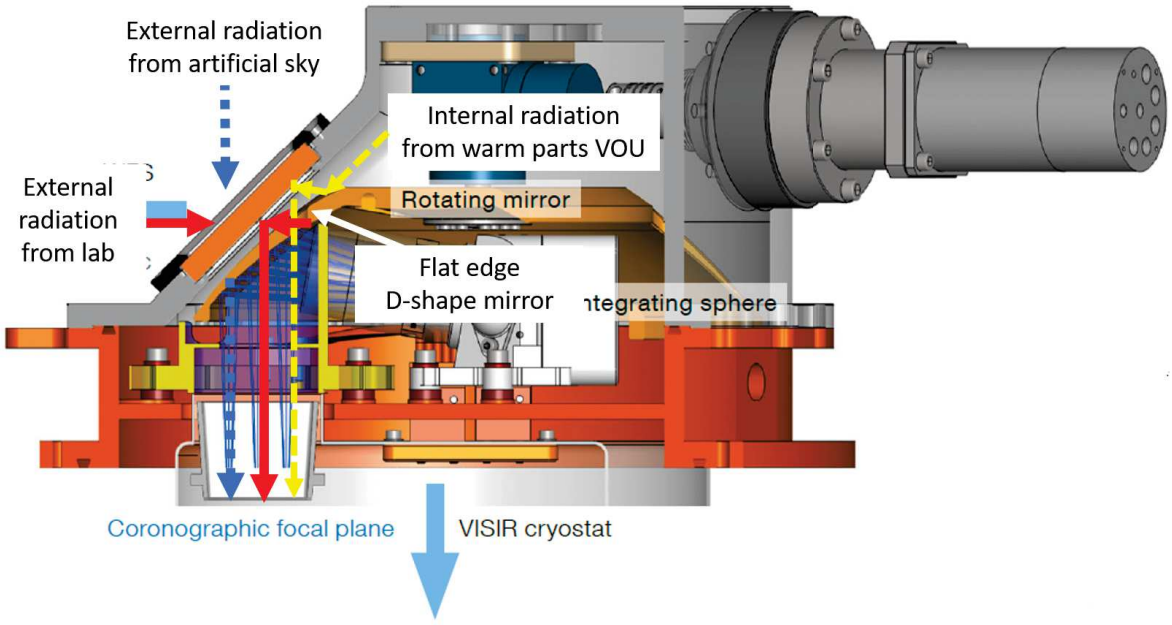

Figure 3.25: Schematisation of the reflections of internal and external thermal radiation which caused the non-flatness of the field seen by the detector, adapted from [5].

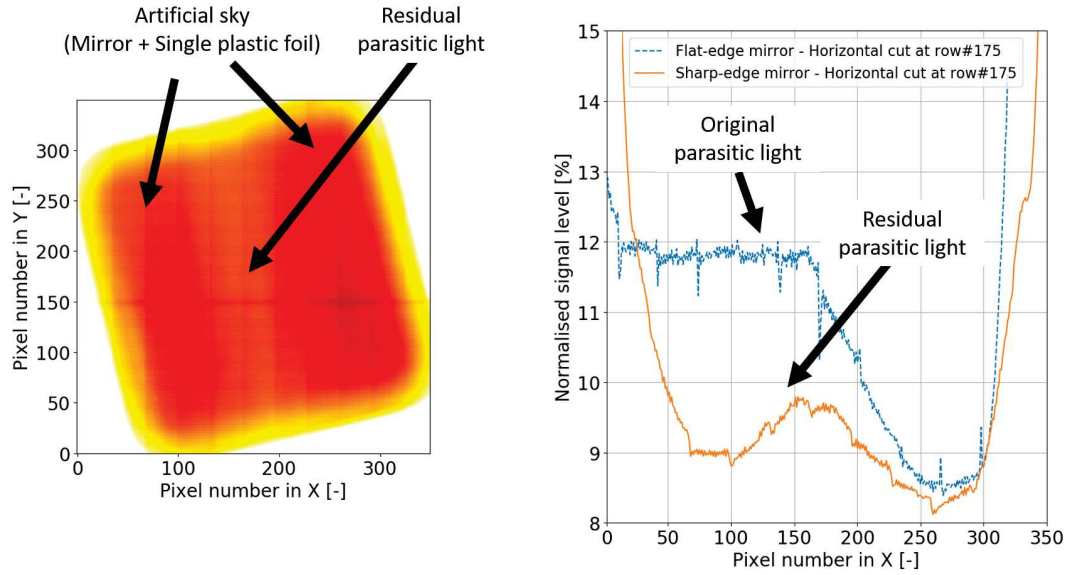

Figure 3.26: Left: artificial sky with single plastic foil as seen by the detector after the implementation of the new baffle and D-shape mirror to mitigate parasitic light effects. Right: comparison of the linecuts of the field seen by the detector when looking at the artifcial sky through one layer of plastic foil after the implementation of the new baffle and D-shape mirror to mitigate parasitic light effects (orange continue curve) and into a container filled with LN_2 before the modifications (blue dash curve). Both background level and artificial sky images were dark corrected, and all frames that shows the residual parasitic light level were recorded after averaging 250 frames, each having $4\,ms$ integration time. The images showing the effects of the implemented modifications were recorded in August 2018

3.5.4. Internal blackbody flux level

Due to the fact that the radiation shield of TIMMI2 is $\sim 30\,K$ warmer than the one of VISIR when the VOU is not mounted, since the beginning it was expected that the BBU would have not reached temperature levels as low as in VISIR ($\sim 128\,K$, see Section 3.3.3). However, after the first cool down the temperature of the BBU was only $239\,K$, not cold enough to produce the required flux level. Few changes to the thermal interface between TIMMI2 and the VOU were needed to bring the BBU to lower temperatures. Yet, as discussed later in Section 3.5.6, the required flux level of $\sim 7.8\%$ of the laboratory background is not achievable without any major intervention on TIMMI2. More details about the single steps of this iterative process are reported in Table 3.3. After iteration #2, even though the flux level was still higher than required, it was considered acceptable to start the characterisation of the BBU, at least for the first tests. However, due to the parasitic light effects already discussed in Section 3.5.3, it was necessary to implement additional baffles in both TIMMI2 and VOU, and that is why iterations #3 and #4 were needed.

Repeatability and stability of the BBU flux level were also measured. The D-shape mirror was oriented in the closed position, so that the thermal emission of the BBU was reflected towards the detector, and its temperature was varied in a controlled way. Figure 3.27 shows the intensity of the total thermal radiation emitted by the BBU at different temperature. The two curves were plotted with data collected in consecutive measurements and performed with the same conditions. What shall be noticed is that the two curves do not overlap even though for each data point the BBU was set at the same temperature. This is due to the fact that the thermal interface between the BBU and TIMMI2 does not allow a fast cooling of the IR source, which as already described in Section 3.3.3 is thermally connected to the blackbody housing and cooled down passively by means of thermal conduction. This is also shown in Figure 3.28, which reports the variation over time of the flux level emitted by the BBU at a constant temperature of $223\,K$. As it can be noticed, the temperature of the IR source cannot in fact be kept constant over time, and therefore the measured flux level increases.

Table 3.3: Summary of the temperature levels of the BBU after each modification of the thermal interface between TIMMI2 and the VOU. In the calculation of the flux levels, both images of BBU and laboratory thermal radiation were dark corrected. The normalisation was done with respect to the laboratory flux level.

Iteration	**Modification**	**Minimum blackbody temperature [K]**	**Minimum baffle temperature [K]**	**Minimum normalised flux level [%]**
0	Same thermal interface as in VISIR	239	261	~ 50
1	Thermal washers with larger inner diameter and slits to half the contact surface with BBU and vacuum housing. Additional copper thermal straps between the BBU and the thermal interface of TIMMI2.	233	240	~ 35
2	Stainless steel screws and washers of the TIMMI2 thermal interface replaced with brass screws and copper berillium wave washers. Thermal sensor added to the thermal interface of TIMMI2 where the copper thermal straps of the BBU are connected.	197	205	~ 11
3	Additional extension baffle at the level of the TIMMI2 entrance baffle. Brass screws and copper berillium wave washers of the TIMMI2 thermal interface replaced with copper screws and washers.	185	195	~ 8
4	Additional baffle at the level of the dichroic window of the VOU.	196	205	~ 9

As shown later in Section 3.5.6, a variation of $\sim 1\%$ in the required flux level corresponds to a temperature difference between $10\,K$ and $20\,K$ for the BBU, which implies that its temperature has to be frequently regulated, at least during long tests with TIMMI2. Because of the lower temperature of the cold shield of VISIR , during on-sky operations it is expected that this instability of the BBU thermal radiation will not occur. In any case, during observations at the telescope a software demon will tune the BBU temperature with a frequency of typically $0.3 - 0.5\,Hz$ to match its flux to the background level.

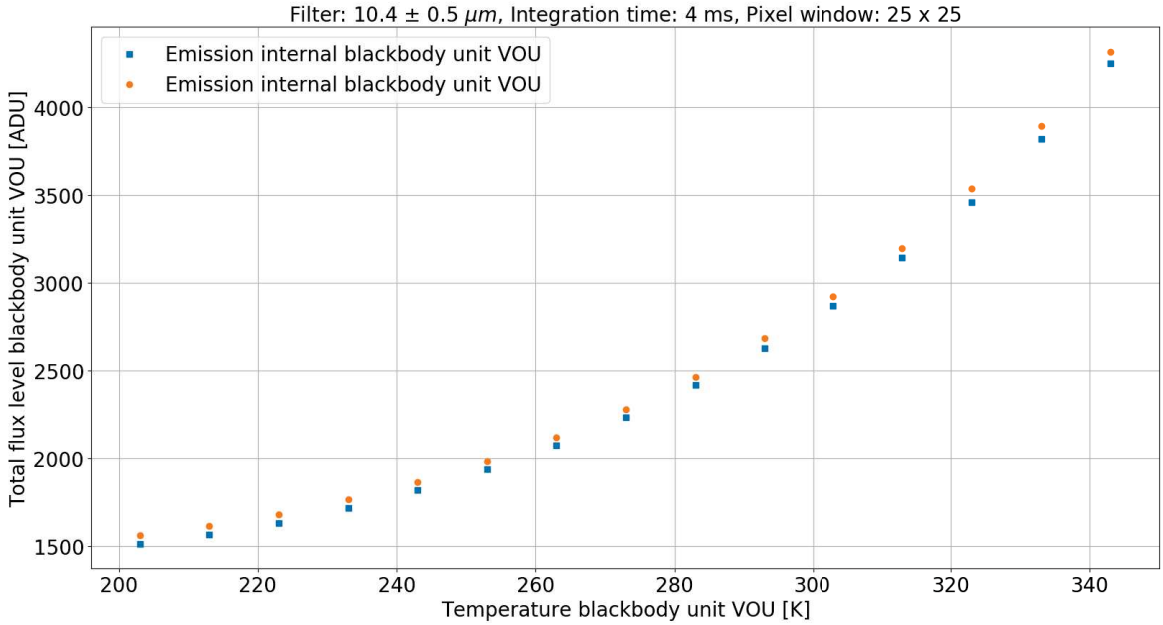

Figure 3.27: Total intensity of the thermal radiation for different temperature of the BBU, calculated for a square window of 25 × 25 pixels. Both background level and artificial sky images were dark corrected, and all frames were recorded after averaging 250 frames, each having 4 ms integration time. The positive offset between the curves plotted with data from the first and second tests is caused by a temperature increment of the IR source, which in TIMMI2 cannot be cooled down rapidly by the blackbody housing.

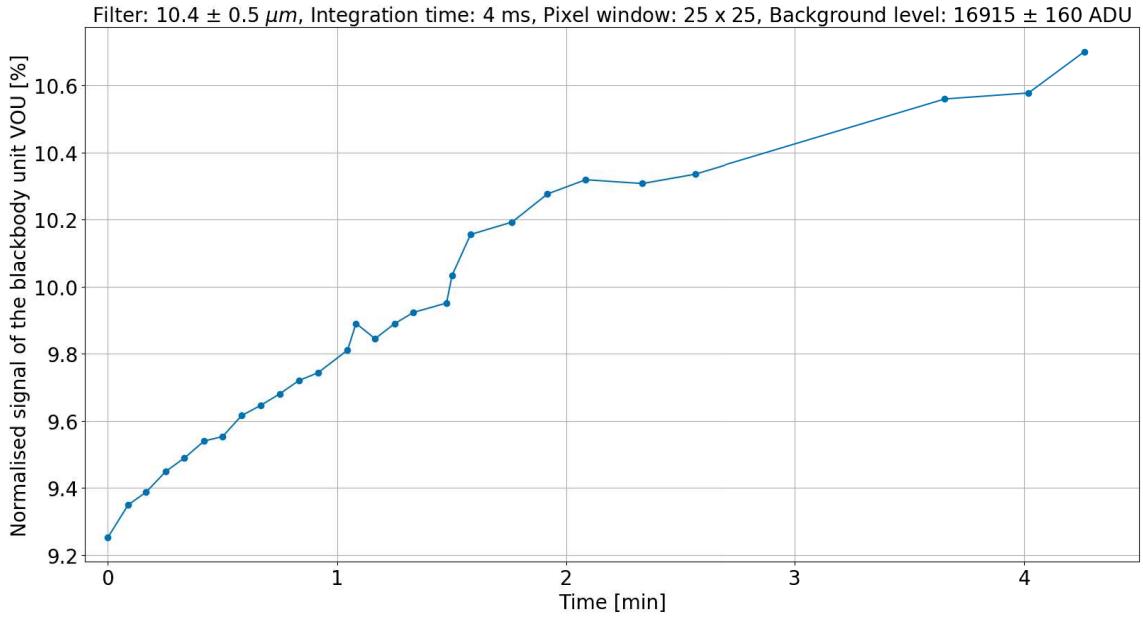

Figure 3.28: Variation of the flux level of the BBU at 223 K normalised to the thermal radiation of the laboratory, calculated for a square window of 25 × 25 pixels. Both background level and BBU images were dark corrected, and all frames were recorded after averaging 250 frames, each having 4 ms integration time.

3.5.5. Internal blackbody uniformity

Besides matching the background level, the flux produced by the BBU shall also be uniform to not add external noise to the measurement. Figure 3.29 compares the raw signal level measured by the detector when illuminated by BBU at 223 K and artificial sky through a double layer of plastic foil. It can be noticed that in both cases the signal has a similar pattern, which is introduced by the spatial fixed pattern produced by the detector. This pattern, however, is nulled in observations due to the chopping and nodding process. The two areas on the sides of the linecut of the artificial sky image are produced by the thermal emission of the baffle of the VOU implemented to mitigate the parasitic light (see Section 3.5.3).

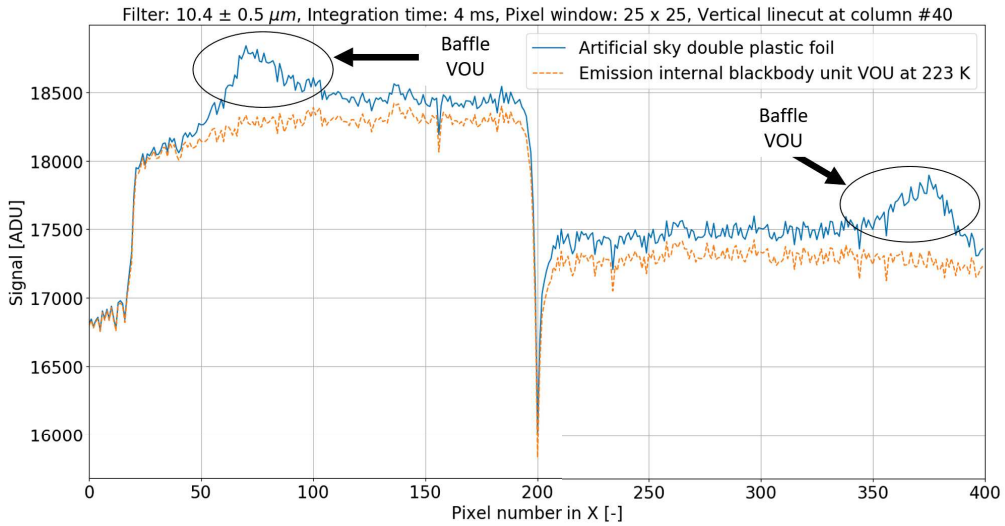

Figure 3.29: Raw linecut of the field seen by the detector when looking at the artificial sky with double plastic foil (blue, continue curve) and at the BBU at a temperature of 223 K (orange, dash curve). Both frames were recorded after averaging 250 frames, each having 4 ms integration time. The large offset in the central part is due to the fixed pattern produced by the detector.

3.5.6. Overall radiometric flux level

Figure 3.30 shows the overall radiometric flux level of the BBU of the VOU and artificial sky. The images were recorded in August 2018, with the VOU not yet in its final configuration. Indeed, the new D-shape mirror required to mitigate the parasitic light produced by the warm parts of the VOU and by reflections of external radiation was not manufactured yet. More details can be found in Section 3.5.3. At the time of this test, the new baffle of the VOU was implemented, as well as the new extension baffle of TIMMI2, but the D-shape mirror was only a test part not gold coated. This implies that the background radiation of the mirror was larger than in the final configuration, while its reflectivity was lower. The radiometric test will be repeated once that the VOU is in its final configuration, but it is expected that the results presented here will not differ significantly.

As already discussed in Section 3.5.4, the fact that TIMMI2 has a warmer radiation shield than VISIR does not allow to achieve the required flux level of $\sim$ 7.8% of the laboratory thermal radiation. To further reduce the temperature levels, a main modification of the thermal interface would have been required, and therefore it was decided to perform the test for the mitigation of the ELFN for a larger value of the background level. Considering that the difference is only of few percentages, it is expected that results and conclusions of the tests will not be affected. Since the ELFN increases with the flux level, the residual ELFN measured on VISIR will be actually lower than what was measured with TIMMI2. In any case, once implemented with VISIR, the temperature of the BBU will be low enough to achieve the required radiometric level to simulate the background radiation at Paranal.

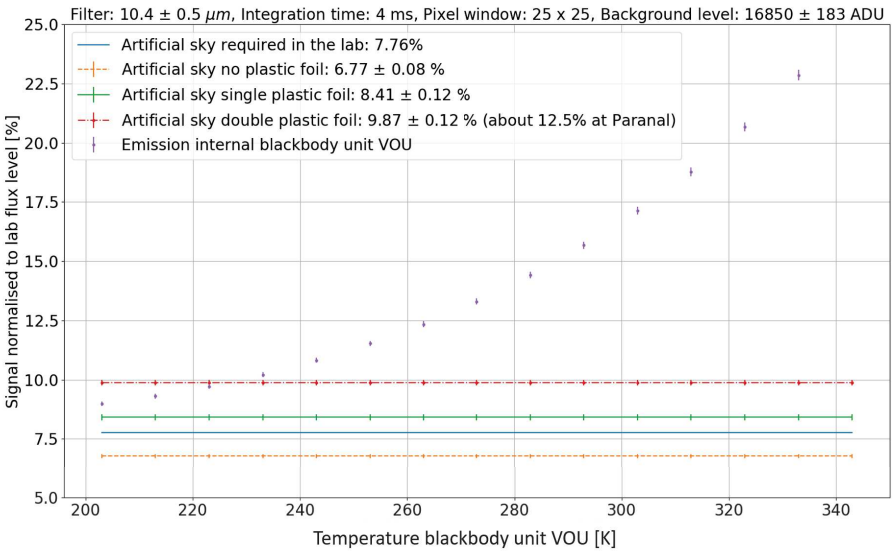

Figure 3.30: Overall radiometric flux level of internal blackbody of the VOU and artificial sky, measured with the VOU not in its final configuration (as of August 2018). All images were recorded after averaging 250 frames, each having 4 ms integration time. Before the normalisation, all images were dark corrected. For each data point, also the one standard deviation value is included.

3.6. Synchronisation of VOU and detector readout controller to perform ELFN noise measurements in chopping mode

While the radiometric measurements described in the previous sections were performed in staring mode, for the ELFN measurements chopping was required. The chopping scheme implemented in the detector readout controller to be used in observations with the VOU is schematised in Figure 3.31.

Each chop cycle starts when the readout controller receives a trigger signal, which is given when the motor driving the D-shape mirror passes through the homing position. For each half-cycle, the number of frames skipped and integrated shall be specified depending on the chop frequency needed. The frames skipped are needed at the beginning of each half cycle to give enough time to the D-shape mirror to completely close or open the FoV of the instrument. All the integrated frames of the first half chop cycle, assumed to contain only background signal from the BBU, are then subtracted to the ones of the second half cycle, which contain sky background and also the source to be observed. A specified number of chop cycles are then integrated to obtain a background corrected image.

An image is correctly chopped when integration time of each single frame (t_{int}), number of frames skipped (N_{skip}) and integrated (N_{int}) for each half cycle and chop frequency (f_{chop}) satisfy the following relation

$$f_{chop} = \frac{1}{2t_{int}(N_{int} + N_{skip})} \tag{3.5}$$

In addition, the frames of each half cycle shall all be recorded with the detector looking in the same region, either containing only background signal or also the source to be observed. If this is not the case, when the integrated frames of each half cycle are subtracted to each other, frames containing the science source cancel out and signal is lost. This happen when the D-shape mirror is not correctly oriented with the motor in homing position. Indeed, based on the scheme of Figure 3.31, for the first half-cycle the D-shape mirror shall be in the closed position to reflect the thermal radiation from the BBU, while for the other half it shall be in open position to allow the external signal to reach the detector. Because of that, the D-shape mirror shall be oriented so that when the motor passes through

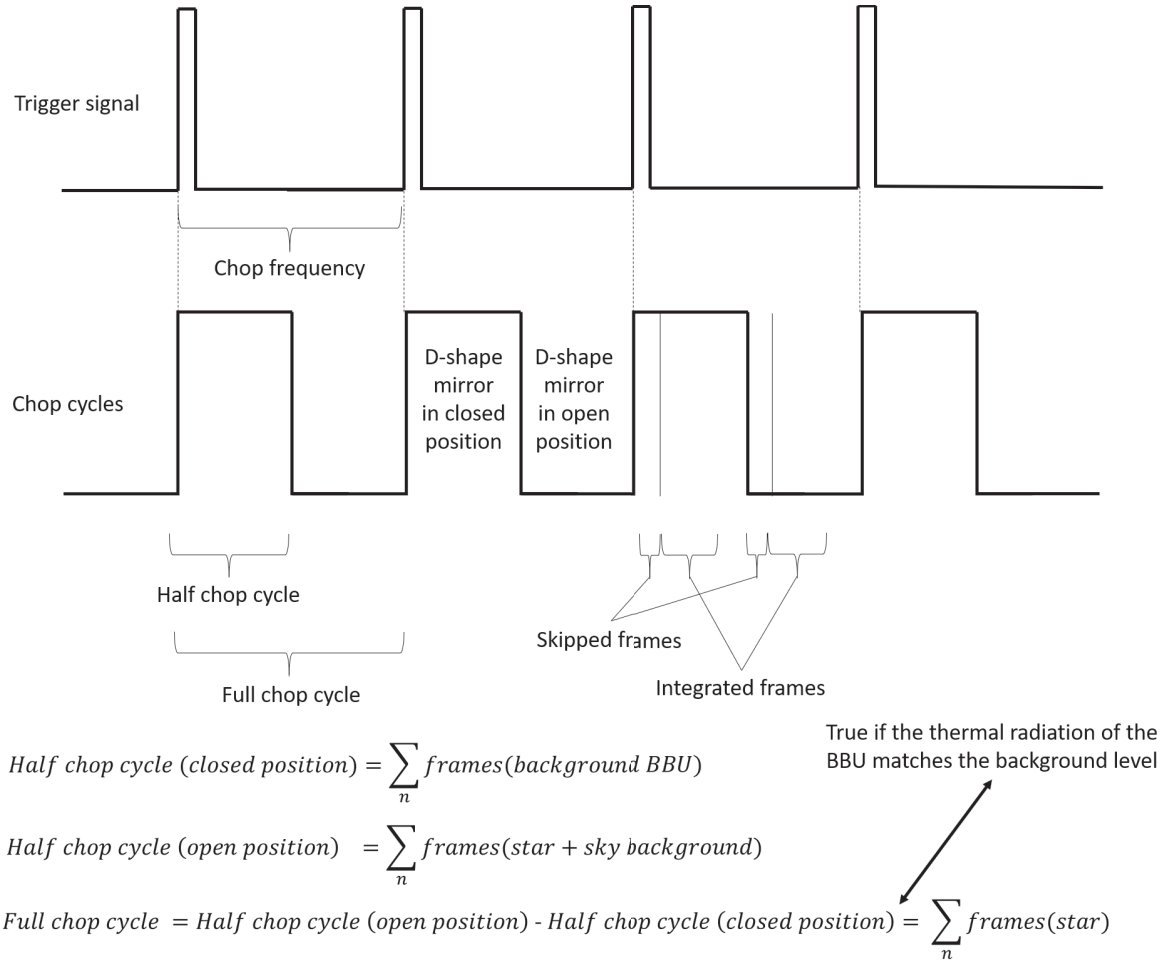

Figure 3.31: Schematisation of the chopping scheme implemented in the detector readout controller. During the ELFN measurements, the VOU was connected to the readout controller and the trigger signal was given when the motor driving the D-shape mirror was passing through the homing position. The D-shape mirror was manually oriented so that when the motor was passing through the homing position, the D-shape mirror was starting to close the FoV of the instrument, allowing for correct integration of chopped images.

the homing position, the D-shape mirror is starting to close the FoV of the instrument. The correct alignment of the D-shape mirror with the homing position of the motor was done manually before the start of the tests for the final validation of the system.

3.7. Test methodologies for the ELFN measurements

Two different kind of chopping measurements were performed in order to validate the ability of the VOU to remove sky backgorund noise and mitigate the ELFN: real chopping using the VOU, and pseudo-chopping simulating the chop frequency with an external pulse generator.

In both cases, the setup used was the same as the one described in Section 3.5.2, since the only external radiating element needed was indeed the artificial sky. The BBU temperature was set to a value that allowed to match the flux level of the artificial sky. After that, chopped images were recorded for different values of the chop frequency.

The difference in the two measurements is that for real chopping, the detector readout controller was trigger directly by the VOU when the motor driving the D-shape mirror was passing through the homing position. On the contrary, in pseudo-chopping the D-shape mirror was stopped and set in open position to allow the detector to see only the artificial sky. The detector readout controller was then trigger using an external pulse generator to simulate different chop frequency.

It is also noteworthy that for real chopping, a minimum of two images per chop frequency was required. They had to be subtracted from each other before calculating the noise in order to simulate a nodding correction and mitigate the residual spatial noise due to a different path of the beam, depending on whether the signal was coming from the artificial sky or from the BBU (see Section 3.2.1). The ELFN was then determined from the standard deviation of each frame, limiting the calculation to a window size of 25×25 pixels. It is also noteworthy that the noise is measured as a pixel-to-pixel variation, and not as repeatability of a single pixel value.

3.8. Test results of the ELFN measurements

The images for the ELFN measurements were recorded with the detector in high gain mode. The BBU temperature was set to $\sim 220\,K$, while the artificial sky was used in the configuration with a double layer of plastic foil. To avoid the risk of saturation and non-linear detector responsivity, the integration time of each frame was limited to $4\,ms$. Number of frames skipped and integrated during each half cycle and chop frequency were then chosen in order to satisfy Equation (3.5). The options chosen for the data presented here are reported in Table 3.4.

Since the number of integrated chop cycles was the same for each set of data, integrated images measured at different chopped frequency had also different total integration time. However, since the noise scales with the square root of the integration time, data recorded at different chop frequency can be compared by multiplying the calculated noise by the square root of the number of total integrated frames.

Results of the ELFN measurements performed with pseudo- and real chopping are reported in Figure 3.33. For each case, the ELFN was calculated in two different regions of the detector with size of 25×25 pixels. They are illustrated in Figure 3.32, which shows also the residual null balance, i.e. the residual intensity of the final integrated image, on two frames recorded at a chop frequency of $9.6\,Hz$ respectively in pseudo- and real chopping mode. What shall be noticed is that while in pseudo-chopping the residual intensity is almost null, on the frame recorded in real chopping mode the intensity residual is of the order of $10^3\,ADU$ and varies across the field. This is a consequence of the fact that the field seen by the detector when looking at the artificial sky is not flat (see Section 3.5.3). In addition, the intensity of the flux level emitted by the blackbody is not constant with time, and therefore the null balance in real chopping mode varies also during each single measurement (see Section 3.5.4).

Table 3.4: List of parameters chosen to record the various images depending of the chop frequency used.

List of parameters used to record chopped images					
Chop frequency	$[Hz]$	1.2	2.4	4.8	9.6
Integration time	$[ms]$	4	4	4	4
Skipped frames per half cycle	$[-]$	16	8	4	2
Integrated frames per half cycle	$[-]$	88	44	22	11
Number of chop cycles	$[-]$	50	50	50	50
Total number of integrated frames	$[-]$	4400	2200	1100	550

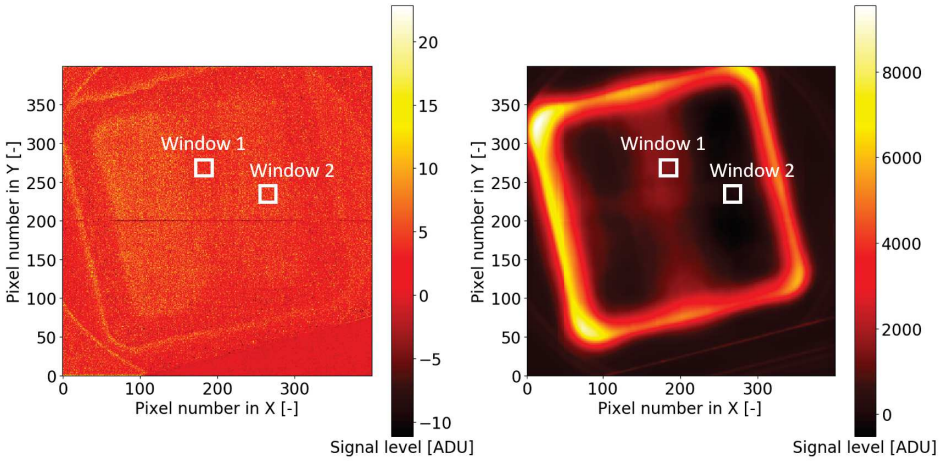

Figure 3.32: Left: image recorded at 9.6 Hz in pseudo-chopping mode. Right: image recorded at 9.6 Hz in real-chopping mode.

Despite of that, in both pseudo- and real chop measurements, the ELFN reduces at high frequency, with measurements at 9.6 Hz more than 50% lower than at 1.2 Hz, validating the ability of the Dicke-switch chopper system to mitigate background level and ELFN. An important aspect is that this is also true for large values of the residual null balance in the real chopped images. Figure 3.34 shows that in the case of measurements performed with real chopping, if two images recorded at the same chop frequency are not subtracted from each other in order to simulate nodding corrections, the residual noise in the image is much larger due to the difference in path between the signal coming from the BBU and from the artificial sky (see Section 3.2.1). More details about the single data points illustrated in the graphs of Figures 3.33 and 3.34 are reported in Table 3.5.

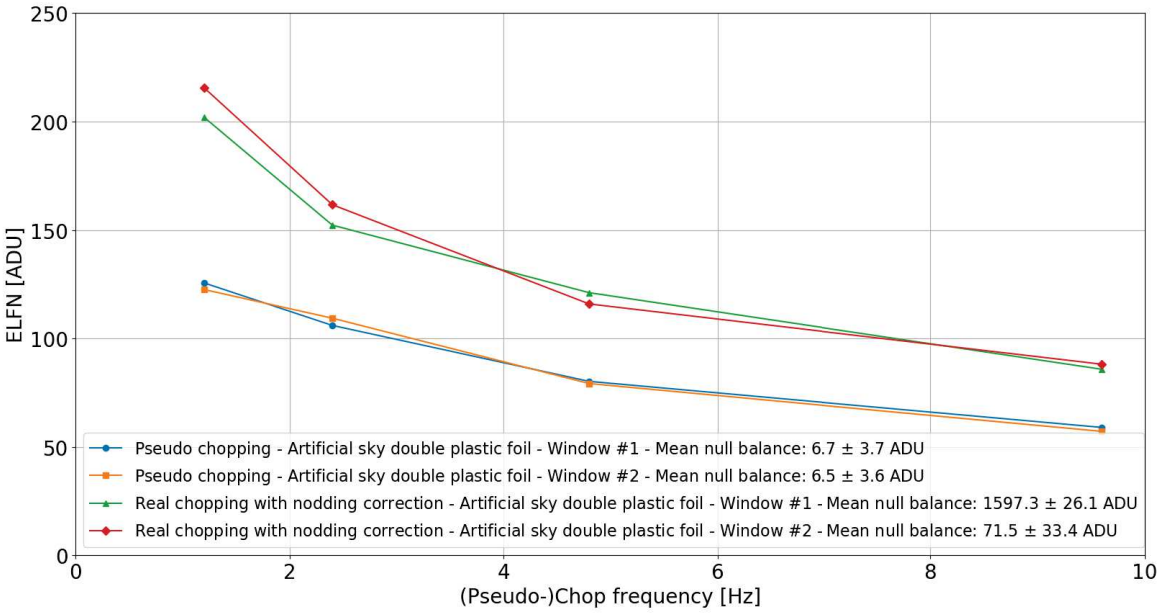

Figure 3.33: ELFN measurements in pseudo- and real-chopping mode. Data point collected in real chopping mode were plotted after nodding correction. It is important to note that measurements performed in pseudo- and real chopping are almost identical, as to validate the ability of the VOU to mitigate the ELFN of the AQUARIUS detector.

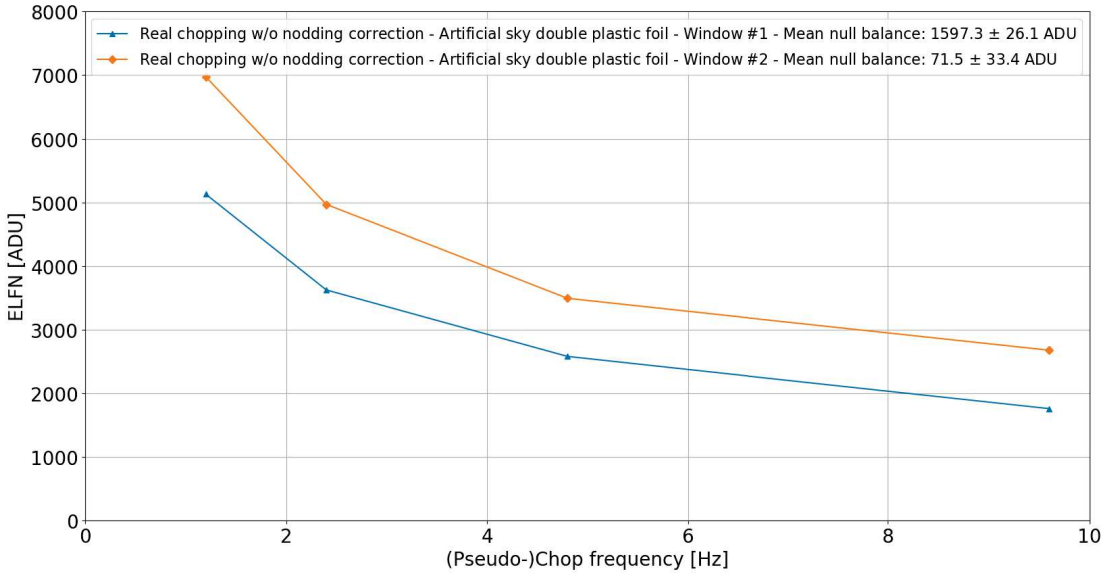

Figure 3.34: ELFN measurements in real-chopping mode without nodding correction.

Table 3.5: ELFN measurements in pseudo- and real chopping mode for two different regions of the detector of size 25×25 pixels. It is important to note that measurements performed in pseudo- and real chopping are almost identical, as to validate the ability of the VOU to mitigate the ELFN of the AQUARIUS detector. For real chopping, ELFN measurements without nodding correction are also reported.

Pseudo-chopping - Window #1					
Chop frequency	$[Hz]$	1.2	2.4	4.8	9.6
Mean null balance	$[ADU]$	13.07	5.39	4.57	3.82
Noise	$[ADU]$	126	106	80.2	59.0
Pseudo-chopping - Window #2					
Chop frequency	$[Hz]$	1.2	2.4	4.8	9.6
Mean null balance	$[ADU]$	12.8	4.9	4.3	4.2
Noise	$[ADU]$	123	109	79.2	57.2
Real-chopping - Window #1					
Chop frequency	$[Hz]$	1.2	2.4	4.8	9.6
Mean null balance	$[ADU]$	1608	1620	1608	1553
Noise w/o nodding correction	$[ADU]$	5132	3626	2582	1761
Noise after nodding correction	$[ADU]$	202	152	121	85.8
Real-chopping - Window #2					
Chop frequency	$[Hz]$	1.2	2.4	4.8	9.6
Mean null balance	$[ADU]$	44.8	69.3	45.2	126.8
Noise w/o nodding correction	$[ADU]$	6976	4971	3495	2679
Noise after nodding correction	$[ADU]$	216	162	116	88.1

4

Characterisation of the AGPM for high contrast imaging: laboratory tests and results

As already mentioned in Section 2.2.1, for the detection of Earth-like planets in the Alpha Centauri region a contrast of $\sim 6 \cdot 10^{-7}$ at angular separations between 2.8 and 3.8 λ/D, or $0.8''$ and $1.1''$, is required. In its present state, VISIR includes an AGPM coronagraph optimised for observations between 11 and 13.1 μm [45], but the achievable contrast is limited to only $\sim 10^{-5}$ at $\sim 1''$.

For this reason, a new AGPM coronagraph optimised for the N-band was designed and manufactured. Two components, named AGPM-BT1 and AGPM-BT2, have already been delivered to ESO for testing, while a third one is being manufactured. An additional coronagraph, referred to as AGPM-N3, was also sent to ESO. It is basically a spare of the one currently implemented in VISIR, thus it is optimised for wavelength between 11 and 13.1 μm. This chapter discusses the laboratory characterisation of AGPM-BT1, AGPM-BT2 and AGPM-N3. After a brief overview on the working principle of an AGPM coronagraph in Section 4.1, Section 4.2 describes the laboratory setup designed to perform the coronagraphic tests, but also alignment procedure and verification of the optical quality of the beam. Centring of Lyot stop and AGPM coronagraph are discussed separately in Section 4.3. Test methodologies, data analysis for the evaluation of the coronagraphic performance and final results are reported respectively in Sections 4.4, 4.5 and 4.6.

4.1. AGPM coronagraph: theoretical background, working principle and manufacturing

The classic Lyot coronagraph [46], an amplitude mask coronagraph, consists of an opaque circular spot which occults the light produced by the star up to few λ/D, and therefore presents the potential risk of blocking light also coming from faint sources orbiting in the circumstellar environment. More in general, low throughput and inner working angle are the major limitations of amplitude mask coronagraphs. Phase mask coronagraphs are based on a different working principle. They induce a differential phase shift between the local polarisation components of the incident light, without blocking the light physically. Similar to other coronagraphs, the diffracted starlight is then stopped by a diaphragm located in the relayed pupil plane downstream [47, 48].

The AGPM is a variation of vector vortex coronagraph and basically consists of rotationally symmetric subwavelength grating [5, 47]. The typical geometry of an AGPM is shown in Figure 4.1 and is defined by the following parameters: depth of the grooves h, period of the grooves Λ and filling factor F, defined as the ratio of the width of the grooves over their period. Due to the difficulties in manufacturing grooves with exactly a rectangular section, in addition to the parameters mentioned above also the slope a of the walls shall be considered to properly characterise the geometry of the grating [48]. For values of the grating period Λ smaller than the wavelength of the incident light, diffraction effects typical of classic spectroscopic gratings do not take place. What happens is that the incident light is forced to propagate in the zeroth order, avoiding any further aberration of the wave front [47].

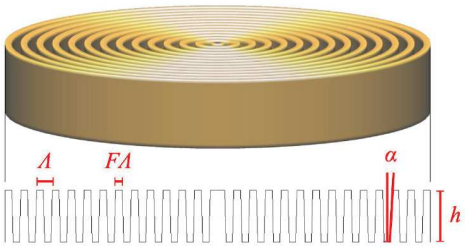

Figure 4.1: Typical geometry of an AGPM coronapgraph, for which the following parameters are defined: depth of the grooves h, period of the grooves Λ, filling factor F, defined as the ratio of the width of the grooves over their period, and slope of the walls a [48].

The working principle of the AGPM is shown in Figure 4.2. The light coming from the circular entrance pupil of the telescope is focused on the image plane where the AGPM is located, which induces a vectorial optical vortex in the light. This means that the phase-shift varies azimuthally around the centre [48]. The central phase singularity causes a total destructive interference of the intensity, creating a dark central core in the PSF which propagates and is conserved along the optical axis. By adjusting the geometrical parameters of the AGPM, it is possible to achromatise the phase shift over a certain range of wavelengths [47]. This effect occurs only for light coming from sources aligned on-axis with the centre of the AGPM, while off-axis beams propagate normally [49]. Before focusing the light on the detector to obtain the coronagraphic image, the beam is collimated so that the diffracted light can be blocked by a Lyot stop placed after the coronagraphic plane and slightly undersized compared to the entrance pupil [48]. It is important to remind that the AGPM works only because in the diffraction limit the wave front is planar. This planar wave is spatially modulated with the Airy pattern and shall be positioned symmetrically on the mask to get the best extinction.

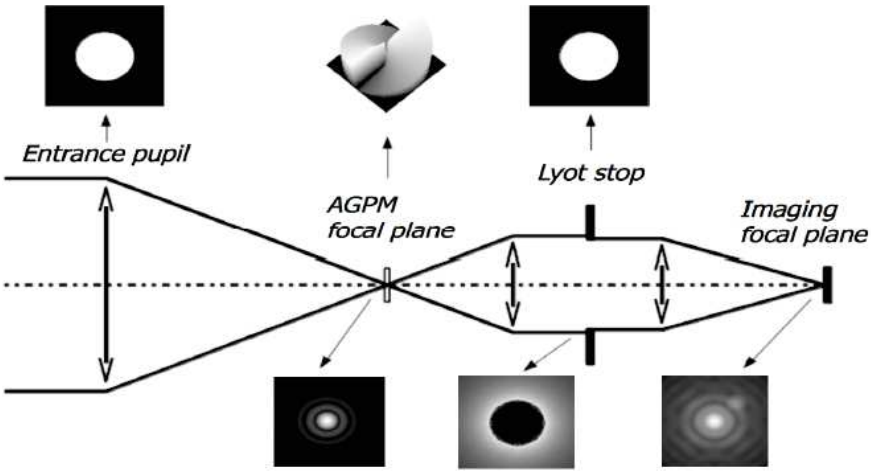

Figure 4.2: Optical scheme of the AGPM coronagraph. The image contains the results of numerical simulations from [47] to show the effects of the AGPM coronagraph [48].

AGPM coronagraphs for applications in the N-band are typically manufacture on diamond substrates with nano-imprint lithography and reactive ion etching [48]. Diamond has a refractive index of ~ 2.38 between 3 and 13 μm, and substrates made from this material have numerous advantages compared to others: wide transmission window, outstanding mechanical properties, especially in terms of low density, very high hardness, and very high elasticity, excellent thermal conduction, and resistance to many usual chemicals [45].

The natural reflection of diamond in the range of wavelength specified above is

$$R = \left(\frac{1-n}{1+n}\right)^2 \sim 17\%$$

The implementation of an anti-reflective grating on the back side of the AGPM coronagraph allows to reduce the intensity of the optical ghosts of the image providing an improved contrast [5, 50]. Moreover, it was proven that between 11.5 and 13 μm the circular diffraction grating on the front side acts as an anti-reflective grating, contributing to reduce even more incoherent reflection which may degrade the coronagraphic performance of the AGPM [50]. Figures 4.3, 4.4, 4.5 and 4.6 show front and back sides of AGPM-BT1.

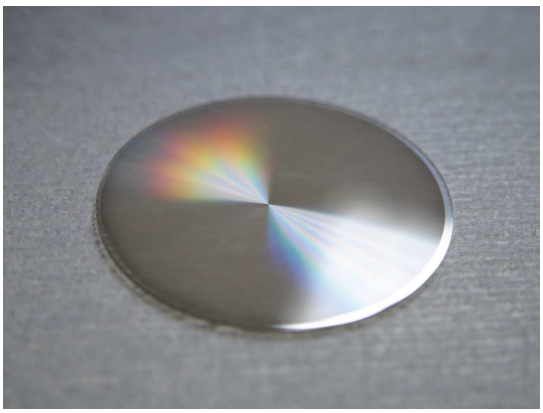

Figure 4.3: AGPM-BT1 coronagraph for the NEAR experiment [Picture from M. Karlsson, University of Uppsala].

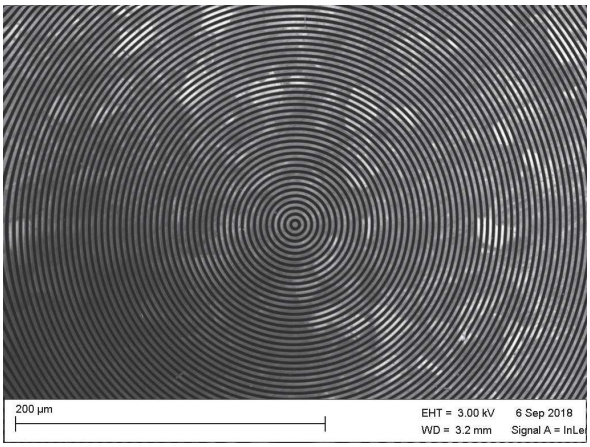

Figure 4.4: Front side of the AGPM-BT1, where the rotationally symmetric subwavelength grating was produced [Picture from M. Karlsson, University of Uppsala].

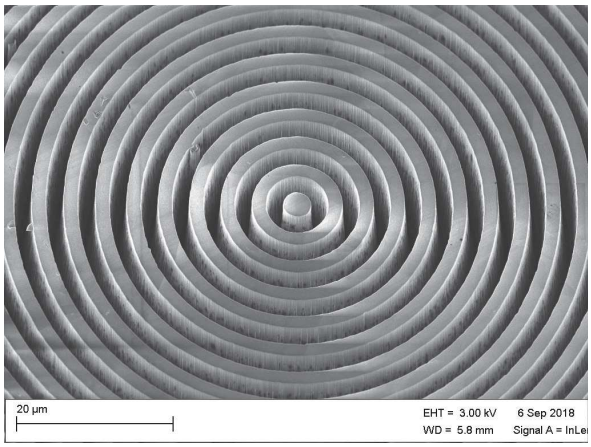

Figure 4.5: Detailed view of the central core of the rotationally symmetric subwavelength grating of AGPM-BT1 [Picture from M. Karlsson, University of Uppsala].

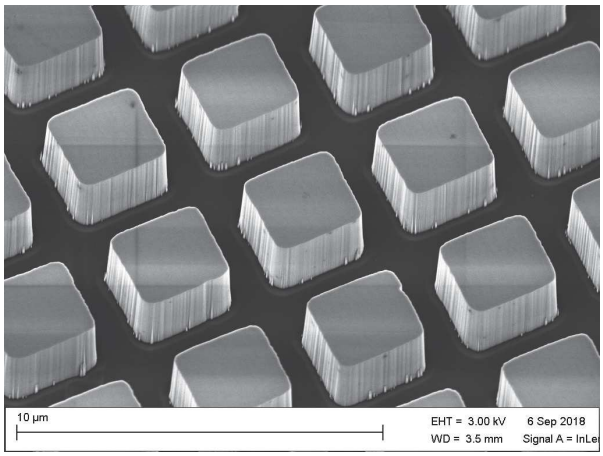

Figure 4.6: Back side of the AGPM-BT1, where the anti-reflective grating was produced. Due to a bit of astigmatism in the laser writer, the anti-reflective grating etched on the back side of the component has rectangular asperities (instead of square). This gives slightly different transmissions for different polarizations of light [Picture and text from M. Karlsson, University of Uppsala].

4.2. Laboratory setup for the coronographic measurements

The optical setup designed to test the AGPMs received is formed by two main parts. The front-end is reported in Figure 4.7 and is based on the optical layout already shown in Figure 4.2. An elliptical mirror focuses a light source, which consists of a $20\,\mu m$ diameter pinhole illuminated by a CO_2 laser, onto the image plane where the AGPM is located. Thanks to an adjustable aperture stop located immediately after the elliptical mirror, the beam is sized to $F_{\#} = 14.3$. After the coronagraphic plane, the beam is collimated towards the pupil plane where the Lyot stop needed to block the diffracted light is positioned. For this reason, the planes containing aperture and Lyot stops are conjugated.

Figure 4.8 shows the back-end part of the setup, which allows to switch between the classic and the pupil imaging mode: the former allows to create an image of the coronagraphic plane onto the TIMMI2 detector, while the second one creates an image of the pupil. This is easily achieved by repositioning a lens mounted on a kinematic base.

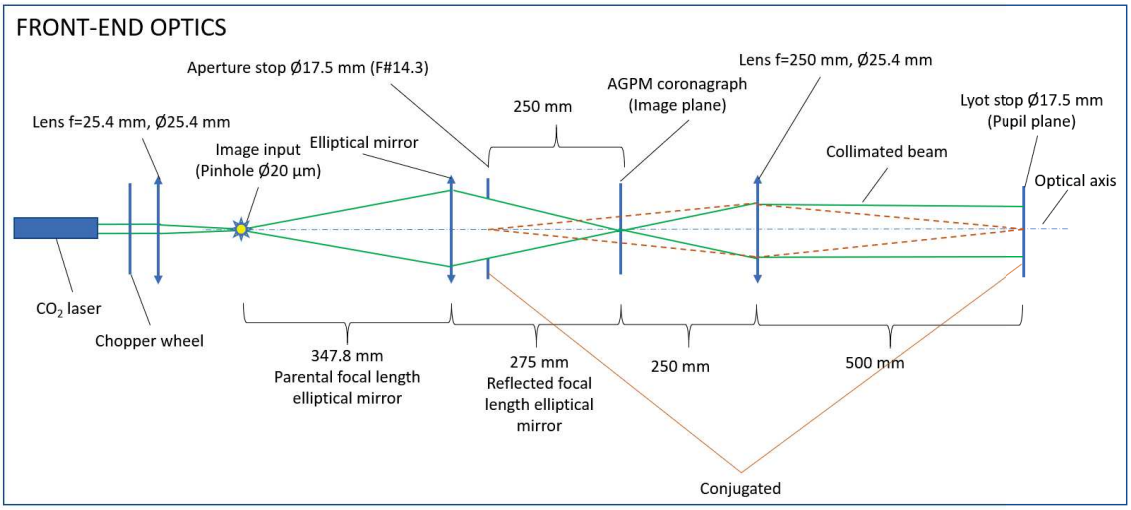

Figure 4.7: Front-end optics of the laboratory setup designed to test the AGPM coronagraphs.

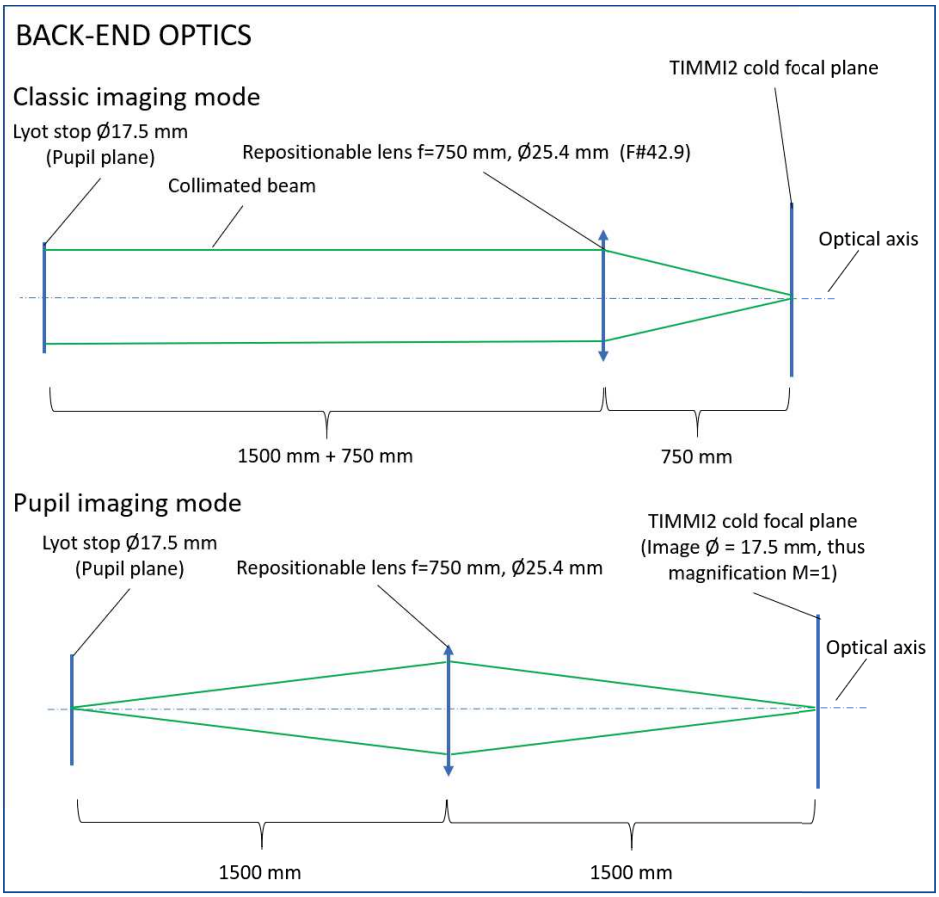

Figure 4.8: Back-end optics of the laboratory setup designed to test the AGPM coronagraphs.

Additional considerations about the optical layout of the setup are reported below:

- The CO_2 laser as light source was needed in order to overcome the background level produced by the laboratory at a wavelength of about $10\,\mu m$. In the shot noise regime, to obtain a peak rejection of 1000 with a S/N of 100 in $10\,s$ of integration time, assuming that the $QE = 1$, 10 000 photons have to be collected after the AGPM, which corresponds to 10 000 000 photons before the coronagraph. Generating $10^6\,ph/s$ above the background level of $\sim 10^8 - 10^9\,ph/s$ photons using a thermal source behind a point like diaphragm, i.e. the $20\,\mu m$ input pinhole, is not easy. Hence, the need of a CO_2 laser. The one used is the L4G model from Access Laser [51]. It provides a beam power of the order of $\sim 100\,mW$ at $\sim 10\,\mu m$ and the wavelength can be selected in the range from 9.3 to 10.7 μm. The calibration provided by the manufacturer was checked with a monochromator. Considering that at $\sim 10\,\mu m$ $1\,mW \simeq 5 \cdot 10^{16}\,ph/s$, the laser is therefore able to provide a beam with enough power for the coronagraphic tests. The beam was focused on the $20\mu m$ pinhole by using an off-the-shelves (OTS) $f = 25.4\,mm$ Ge lens, and the input power was regulated by defocusing the lens with respect to the pinhole

- The beam emitted by the CO_2 laser was chopped to correct the background flux level. To also suppress the ELFN noise, a chop frequency of $10\,Hz$ was used, as also confirmed by the conclusion of Chapter 3. The configuration of the chopping scheme used was analogous to the one described in Section 3.6. A pulse generator was used to generate a pulse with a frequency of $10\,Hz$ in order to trigger the detector readout controller and a mechanical chopper wheel. In addition to that, an oscilloscope was used to manually adjust the phase of the mechanical chopper to maximise the flux integrated on the chopped image, and therefore avoiding self-subtraction of frames containing the light source

- The choice of a pinhole with diameter of $20\mu m$ was driven by the need to have a light source smaller than the diffraction limit of an $F_{\#} = 20$ beam, the one associated with the parental focal length of the elliptical mirror, as well as to limit the power of the CO_2 laser focused on the TIMMI2 detector, which if excessively large may cause permanent damages

- Leakage intensity increases proportional to the square of the centring error in units of λ/D [52], thus to have a null-depth of 10^{-3} the AGPM shall be centred in the focus with a positioning accuracy of $\sim 1/30\,\lambda/D$ in X and Y, assumed to be respectively the horizontal and vertical direction, which for the chosen setup corresponds to $\sim 5\mu m$. The AGPM was therefore placed on a XY translation mount with differential drives which provided fine positioning control of $0.5\,\mu m$. Moreover, the achromatic elliptical mirror allowed to accurately focus the pinhole onto the image plane using using a red optical beam at $\sim 650\,nm$ generated by a Helium-Neon (HeNe) LED source. The optical quality at the coronagraphic plane was then checked with a CCD camera. More details about the alignment procedure are given in Section 4.2.1

- Since the performance of the AGPM does not depend on the $F_{\#}$ of the incident beam, it was decided to use a larger $F_{\#}$ than the 13.4 of VISIR in order to easily image the aperture stop onto the pupil plane with an image magnification of 1:1 by using an OTS $f = 250\,mm$ Ge lens, given a pupil diameter in the Lyot plane of $17.5\,mm$

- Considering that TIMMI2 accepts a beam with minimum focal ratio of $F_{\#} = 35$, a minimum focal length of $612.5\,mm$ was required to avoid vignetting after focusing the $17.5\,mm$ collimated beam in the classic imaging mode. For this reason, an OTS Ge lens with focal length $f = 750\,mm$ was chosen

- The same $f = 750\,mm$ Ge lens used for the classic imaging mode was also used to image the pupil plane. This choice was driven by the limited availability of OTS IR lenses, especially considering the relatively large $F_{\#} = 35$ beam accepted by TIMMI2, but also by the fact that the image magnification had to be smaller than 2. Indeed, the limiting aperture at the TIMMI2 cold focal plane was the $35\,mm \times 35\,mm$ aperture of the VOU vacuum housing (see Figure 3.17), while as mentioned above the pupil had a diameter of $17.5\,mm$. It was therefore decided to limit the image to a 1:1 magnification

- From Figure 4.9, which shows the real optical setup, it can be noticed that numerous folding mirrors were included. This is again a consequence of the limiting $F_{\#} = 35$ beam of TIMMI2, which requires a relatively large optical path, especially in the pupil imaging mode. Indeed, in order to image the pupil with a magnification of 1:1 with an $f = 750\,mm$ lens, object and image planes had to be $1500\,mm$ far from the lens itself, for a total of $3\,m$ optical path only for the back-end optics, plus the almost $1.5\,m$ for the front-end part of the setup

4.2.1. Alignment of the optical setup using optical light

The procedure followed to align the optical setup described in the Section 4.2 included four main steps, listed below and described more in details in the next paragraphs:

1. Alignment of an optical beam with the optical axis of TIMMI2

2. Alignment of the optical components from the $f = 750\,mm$ Ge lens placed as in the classic imaging mode to the $20\,\mu m$ input pinhole, thus in the reverse order with respect to the path of the IR beam

3. Alignment of the IR beam emitted by the CO_2 laser with the $20\,\mu m$ input pinhole

4. Determination of the optimal X and Y positions of the $20\,\mu m$ input pinhole in order to ensure a good optical quality at the coronagraphic image plane

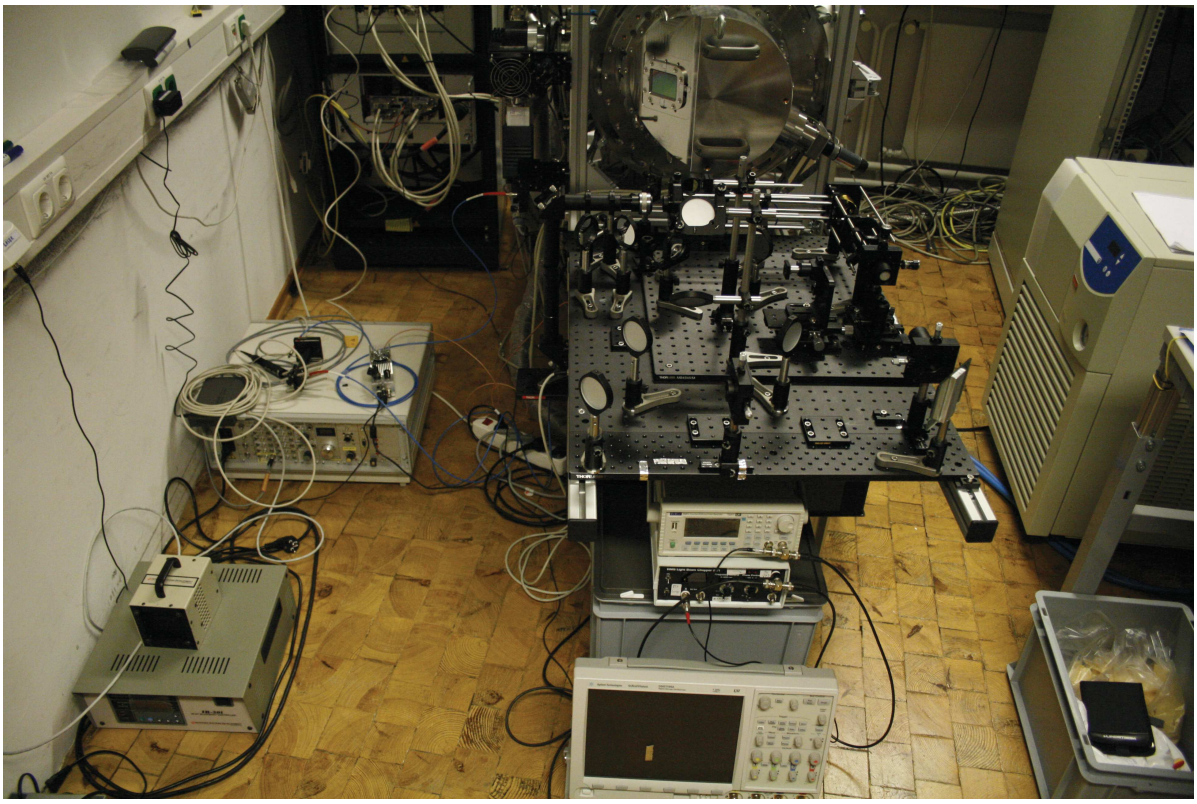

Figure 4.9: Laboratory setup designed to characterise the AGPM coronagraph.

Determination of the optical axis of TIMMI2

At the time of the AGPMs characterisation, the VOU was still mounted on TIMMI2 since the gold coated D-shape mirror with the sharp edge was not yet delivered to ESO for the final tests. It was therefore possible to take advantage of the dichroic window of the VOU to reflect towards the optical setup an optical beam coming from one side of TIMMI2 and then align it with its optical axis.

First of all, the optical axis of TIMMI2 was determined at IR wavelengths. Figure 4.10 illustrates a schematisation of the setup used. A flat mirror was mounted in front of the $f = 750\,mm$ Ge lens, which was placed at the position of the classic imaging mode, thus at a distance of $750\,mm$ from the cold focal plane of TIMMI2. This was done in order to obtain a flux level lower than the background level of the laboratory, and therefore clearly visible on the detector. Similarly to what was already explained in Section 3.5.2, the signal impinging on the detector was therefore formed by different contribution: twice the emission of the dichroic window, twice the emission of the Ge lens, emission of the flat mirror, emission coming from TIMMI2 and reflected back by the flat mirror and also the residual parasitic light discussed in Section 3.5.3. In this configuration, the detector was therefore looking at the flat mirror through the Ge lens, as shown in Figure 4.11. The image of the flat mirror was then centred with the the FoV of TIMMI2, and by ensuring that it had a circular shape and minimising its flux level, the system formed by Ge lens and flat mirror could be considered aligned with the optical axis.

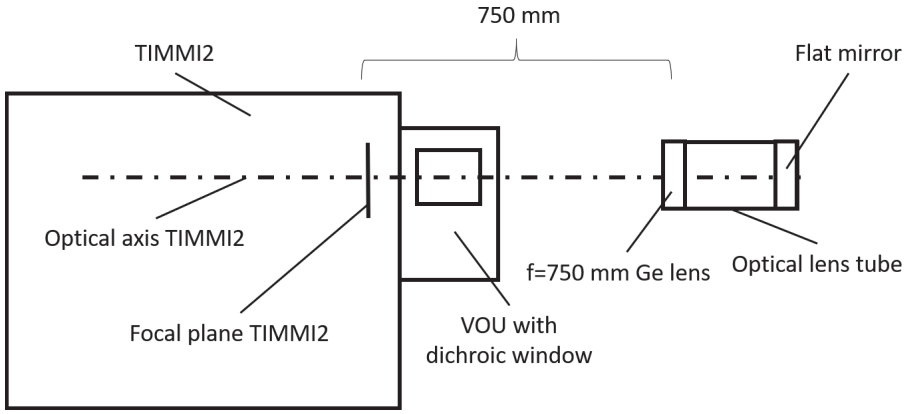

Figure 4.10: Schematisation of the setup used to determine the optical axis of TIMMI2 at IR wavelengths. The $f = 750\,mm$ Ge lens is positioned as in the classic imaging mode of the optical setup designed to characterise the AGPM coronagraphs.

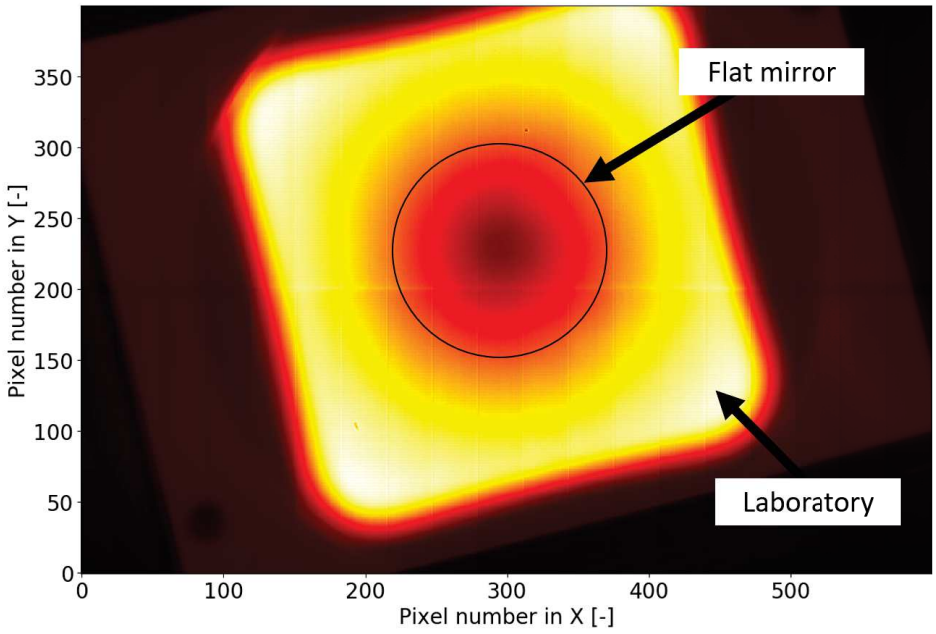

Figure 4.11: View of the TIMMI2 detector when looking at the flat mirror through the $f = 750\,mm$ Ge lens after its alignment with the optical axis. The region labelled *flat mirror* is the sum of different contribution that together generate a signal lower than the background level of the *laboratory*, and therefore clearly visible on the detector.

After this, the optical axis of TIMMI2 was also determined physically by cutting the field in both vertical and horizontal directions by using two paper strips placed in front of the VOU dichroic window. Figure 4.12 shows the cut field as seen by the detector.

This physical reference was needed to align the optical beam emitted by the HeNe LED source with the optical axis. The source of the optical beam was located on the side of TIMMI2, and two folding mirrors placed on kinematic mounts were used to adjust tip-tilt directions, as shown in Figure 4.13. The optical beam was then reflected towards the optical setup by the dichroic window of the VOU, coated to transmit light only at wavelengths between 10 and 12.5 μm.

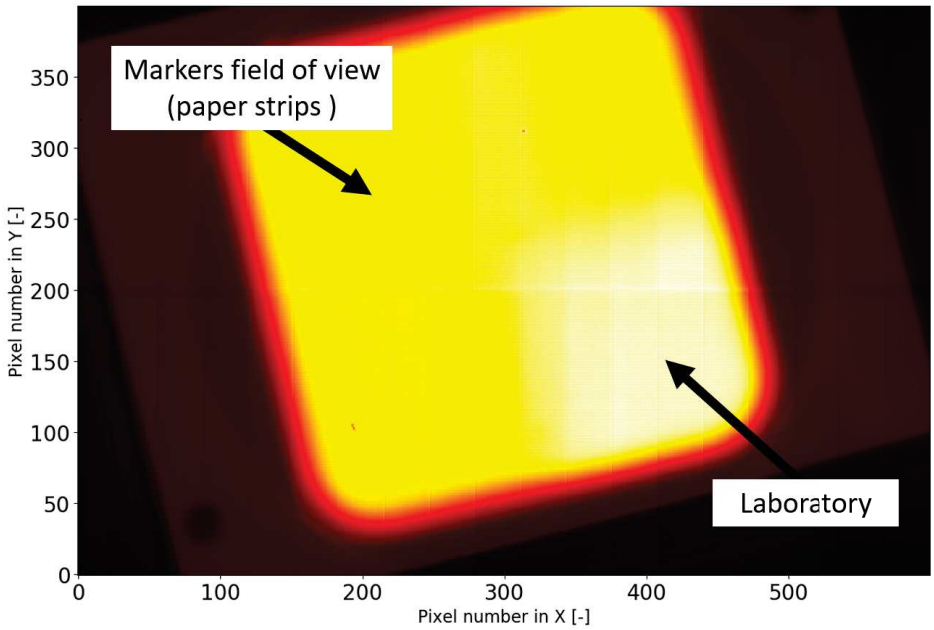

Figure 4.12: View of the TIMMI2 detector when looking at the laboratory after that two paper strips were placed in front of the dichroic window of the VOU in order to physically determine the optical axis.

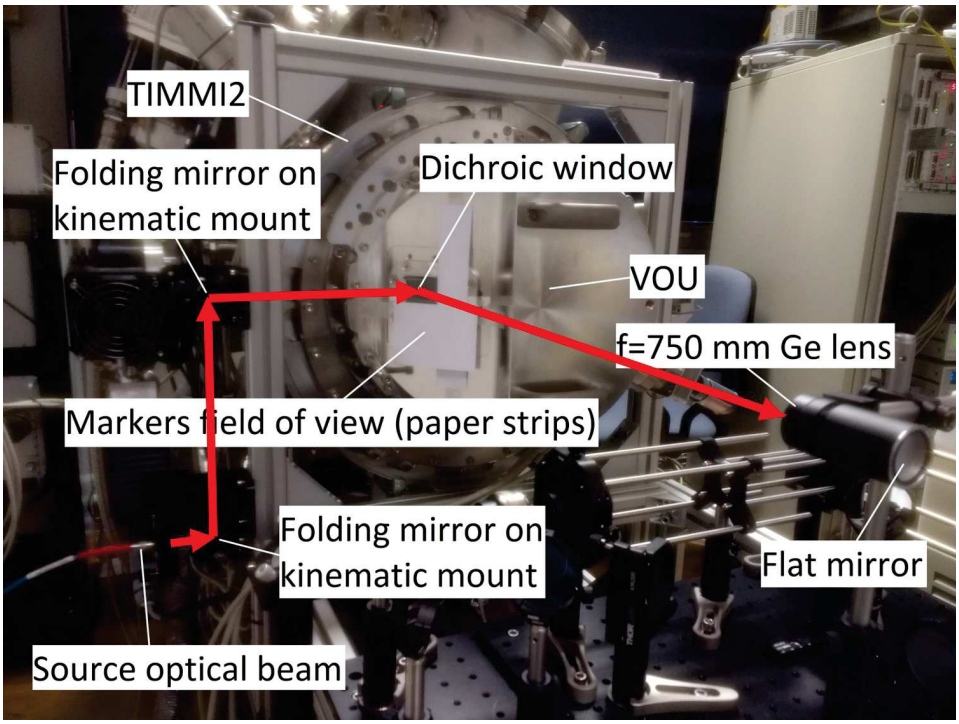

Figure 4.13: Two paper strips were used to cut the FoV of TIMMI2 both horizontally and vertically in order to physically determine its optical axis. The source of the optical beam was directed towards the dichroic window of the VOU by using two folding mirrors, and then reflected back towards the setup. The path of the optical beam is shown in red. The image illustrates also the $f = 750\,mm$ Ge lens, positioned as in the classic imaging mode of the optical setup, and the flat mirror used to determine the optical axis at IR wavelengths.

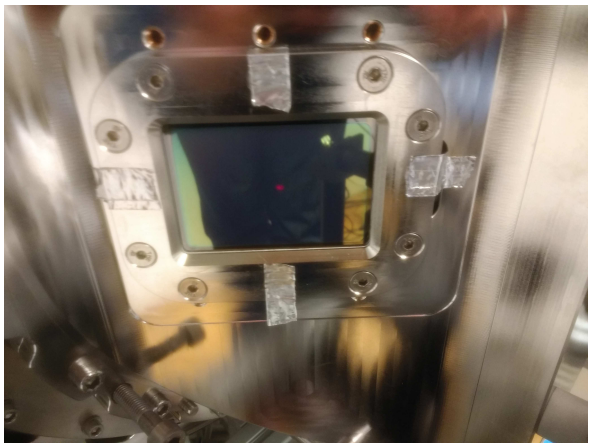

Figure 4.14: The optical beam had to be reflected back by the flat mirror at exact the same location on the dichroic window to ensure that it was parallel to the optical axis of TIMMI2.

Figure 4.15: To ensure that the optical beam reflected by the dichroic window was aligned with the optical axis, it had also to pass through the centre of the $f = 750\,mm$ Ge lens, already aligned with the optical axis, which for convenience was replaced with a $\sim 1\,mm$ circular aperture.

These two folding mirrors were indeed adjusted in such a way to direct the optical beam close to the centre of the dichroic window of the VOU, based on the marks used to physically determine the optical axis of TIMMI2. Two conditions had to be verified to ensure a correct alignment with the optical axis. First, the optical beam had to be reflected by the flat mirror at exact the same location on the dichroic window of the VOU, in order to have a beam parallel to the optical axis (see Figure 4.14). Second, the optical beam had to hit the $f = 750\,mm$ Ge lens at its centre, already aligned with the optical axis of TIMMI2, which for convenience was replaced with a $\sim 1\,mm$ circular aperture (see Figure 4.15). Once that these two conditions were satisfied, the optical beam could be considered aligned with the optical axis of TIMMI2.

Alignment of all the optical components

Once that the direction of the optical axis was known, all the other components were mounted at the required distance (see Figures 4.7 and 4.8) and then aligned with the optical beam. In doing so, the folding mirrors were oriented to ensure that the beam hit all the components in their centre, while since Ge is not transparent at optical wavelengths, the lenses were replaced with circular apertures of diameter $\sim 1\,mm$ and adjusted in X and Y to make sure that the beam was correctly centred. Two of the folding mirrors were placed on a kinematic mount to allow the adjustment of tip-tilt directions of the beam, and a $\sim 1\,mm$ circular aperture was moved along the beam direction to verify that it was kept parallel to the optical table.

Alignment of the IR beam emitted by the CO_2 laser

The optical resonator of the CO_2 laser, where the amplitude of the beam is amplified, includes the so called output coupler, which is basically a partially reflective mirror located close to the output port of the laser. Based on this consideration, two conditions needed to be satisfied in order to guarantee a correct alignment: the incoming optical beam emitted by the HeNe LED source had to hit the laser at its circular output port, and its reflection had to be centred with the $20\,\mu m$ input pinhole. For this purpose, the input pinhole was replaced with a $\sim 1\,mm$ circular aperture to increase the intensity of the optical beam, which otherwise would have not been visible with naked eyes. Again, two folding mirrors on kinematic mounts allowed tip-tilt adjustments of the beam direction.

Determination of the optimal X and Y positions of the 20 μm input pinhole

As already mentioned in Section 4.2, to obtain a null depth of 10^{-3}, the AGPM shall be aligned with a positioning accuracy of $1/30\,\lambda/D$, thus $\sim 5\,\mu m$. On one hand, using an elliptical mirror to image the $20\,\mu m$ input pinhole onto the coronagraphic plane has the advantage that the alignment can be done using optical light. On the other hand, the elliptical mirror has a quite reduced FoV which is free from aberrations, as shown in Table 4.1. This implies that the input pinhole shall be adjusted with micrometer accuracy in order to achieve a good image quality at the AGPM location. However, once that good optical quality is achieved with optical light, this would be even better at IR wavelength. Indeed, at $650\,nm$ the Rayleigh criterion is satisfied if the WFE peak-to-valley is smaller than $\lambda/4 = 162.5\,nm$, which corresponds to an optical quality of $\sim \lambda/65$ at an IR wavelength of $10.5\,\mu m$.

To verify the optical quality of the beam at the AGPM locations, a CCD camera was placed in the coronagraphic plane, and the $20\,\mu m$ input pinhole was illuminated with the red optical light of the HeNe LED source ($\sim 650\,nm$). To obtain a diffracted limited image, the CCD camera was moved along the optical axis in the best focus position, while the pinhole was adjusted along the X and Y directions. In order to avoid under-sampling of the full-width-half-maximum (FWHM), the aperture size was reduced to have an $F_{\#}$ larger than the design value of 14.3. Indeed, the CCD camera used has a pixel pitch of $5.5\,\mu m$, and therefore, considering thatb the $FWHM \simeq \lambda F_{\#}$, at $650\,nm$ and $F_{\#} = 14.3$ it extends over ~ 2 pixels, while at at $650\,nm$ and $F_{\#} \simeq 30$ it extends over ~ 4 pixels. The resulted image for an $F_{\#} \simeq 30$ beam is reported in Figure 4.16.

Table 4.1: Simulation of the RMS WFE induced by the chosen elliptical mirror for a beam size of $F_{\#} = 13.4$ (simulation made by J. Kosmalski, ESO).

Off-axis Field [mm]	**RMS WFE [mm]**
0.2	100
0.4	200
0.6	300

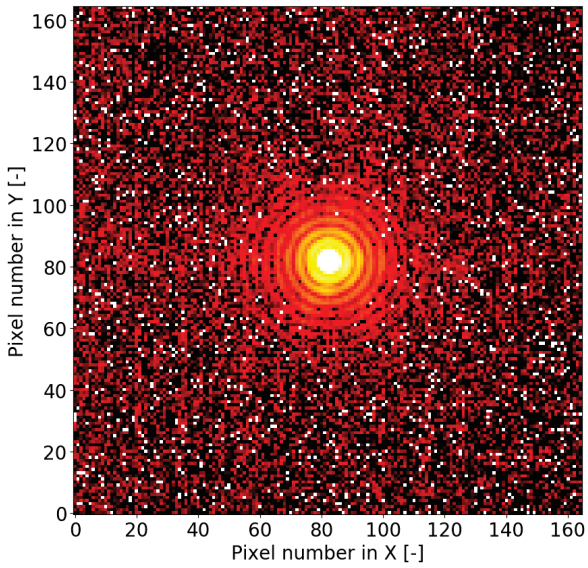

Figure 4.16: PSF at the level of the coronagraphic plane at optical light $\sim 650\,nm$ for an $F_{\#} \simeq 30$ beam imaged with a CCD camera.

4.2.2. Verification of the alignment with the IR beam

Once that the alignment using the optical beam was completed, the CO_2 laser was switched on to verify that in fact both PSF and pupil images had good optical quality also at IR wavelengths, and that vignetting was not occurring. While the PSF looked diffraction-limited, the pupil had a quite poor image quality, as clearly visible from Figure 4.17.

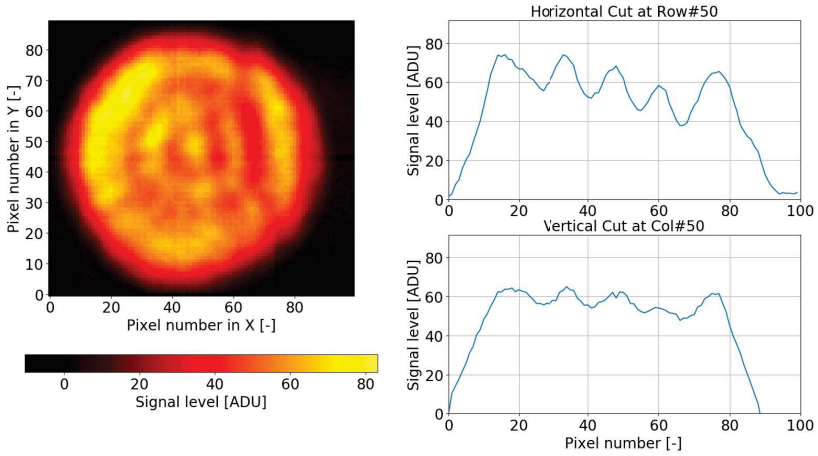

Figure 4.17: Pupil image for a 17.5 mm aperture stop at 10.5 μm. Right: horizontal (up) and vertical (bottom) cut levels of the pupil image.

It was therefore decided to start an investigation in order to understand the origin of the circular pattern that was creating intensity fluctuations over the whole pupil. It is noteworthy that the investigation was limited to the front-end part of the setup (see Figure 4.7). Indeed, if an AGPM performs as expected, the IR light redistributed away from the optical axis is then blocked by the Lyot stop, after which there is no light left, and thus the components of the back-end part of the setup do not affect the performance of the coronagraph.

Based on this consideration, three main reasons were identified as possible causes of the poor pupil image quality: fringing caused by the monochromatic light of the CO_2 laser, aberrations due to the elliptical mirror and ghosts caused by the anti-reflective coating of the re-imaging $f = 250\,mm$ Ge lens. Few tests were performed in order to evaluate separately their effects on the pupil image quality. In order to limit additional degradation caused by aberrations and vignetting, it was decided to reduce the aperture stop to 10 mm (see Figure 4.7).

Monochromatic CO_2 laser: images perturbed by fringing

The 20 μm input pinhole was replaced with a 500 μm one, which is still smaller than the diffraction limit for the about $F_{\#} \simeq 30$ beam associated with the parental focal length of the elliptical mirror, at least when considering a 10 mm aperture stop. Instead of using the CO_2 laser as monochromatic IR light source, the light of an external blackbody, set at a temperature of $\sim 110°C$, was focused on the new larger input pinhole thanks to an $f = 200\,mm$ Ge lens. The wavelength of the beam were limited between 9.9 and 10.9 μm. Despite these changes, the circular patterns were still visible, with same intensity fluctuations as in the nominal configuration with the pinhole illuminated by the CO_2 laser, a fact which suggests that indeed it was not cause of the problem (see Figure 4.18).

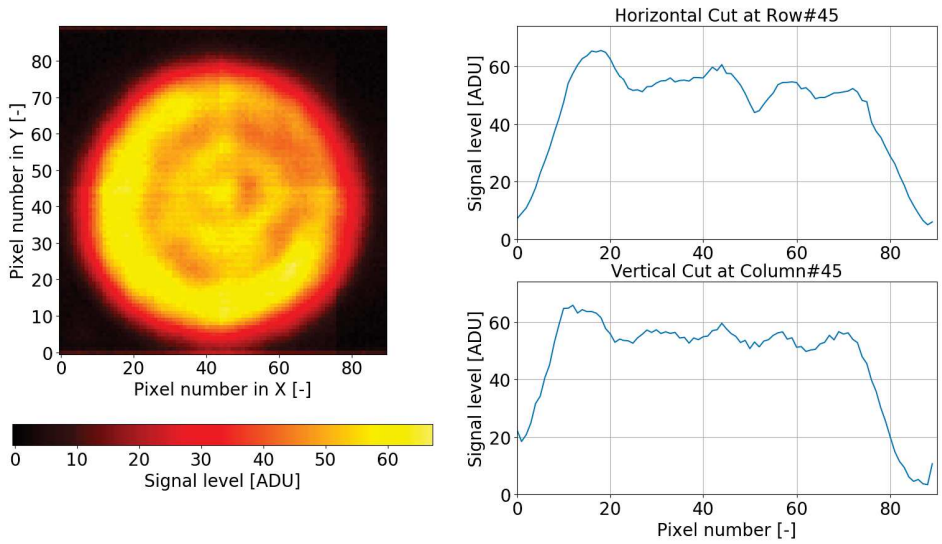

Figure 4.18: Left: pupil image for a $10\,mm$ aperture stop when illuminating a $500\,\mu m$ input pinhole using an external blackbody set at $110\,°C$. Right: horizontal (up) and vertical (bottom) cut levels of the pupil image.

Residual aberrations of the elliptical mirror

The $20\,\mu m$ input pinhole was placed at the coronagraphic image plane, thus after the elliptical mirror, and was illuminated with the CO_2 laser. Even in this case, the circular pattern was still visible, which implies that it is also not caused by the elliptical mirror (see Figure 4.19)

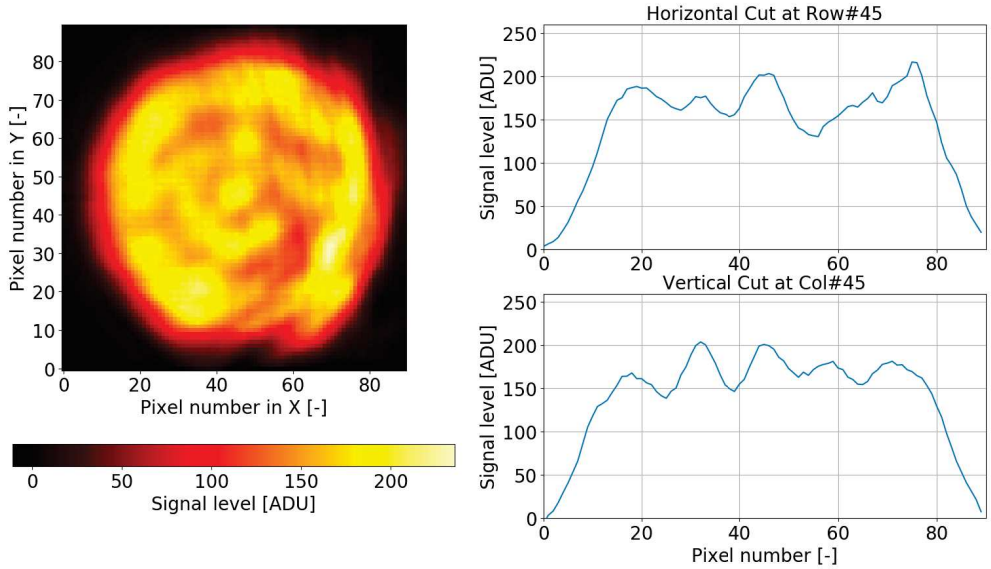

Figure 4.19: Left: pupil image for a $10\,mm$ aperture stop when illuminating the $20\,\mu m$ input pinhole located at the coronagraphic image plane with the CO_2 laser. Right: horizontal (up) and vertical (bottom) cut levels of the pupil image.

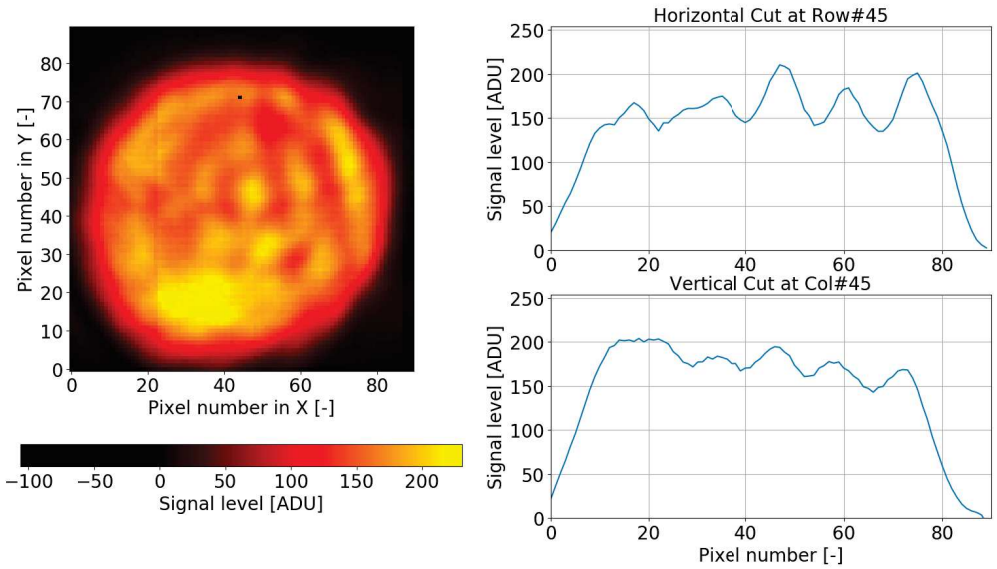

Figure 4.20: Left: pupil image for a $10\,mm$ aperture stop when illuminating the $20\,\mu m$ input pinhole located at the AGPM location with the CO_2 laser and collimating the beam with a re-imaging $f = 200\,mm$ Ge lens. Right: horizontal (up) and vertical (bottom) cut levels of the pupil image.

Ghosts of the re-imaging $f = 250\,mm$ Ge lens

Still in the configuration with the $20\,\mu m$ input pinhole placed at the coronagraphic image plane and illuminated with the CO_2 laser, the re-imaging $f = 250\,mm$ Ge lens was replaced with an $f = 200\,mm$ Ge lens. However, also with the new lens the circular patterns were still present, thus they were not caused by the re-imaging $f = 250\,mm$ Ge lens (see Figure 4.20)

Conclusion about the investigation on the degraded pupil image quality

In conclusion, all the tests performed confirmed that the circular pattern that degrades the pupil image quality originates after the Lyot stops, and therefore does not affect the coronagraphic performance of the AGPM. This fringing is most likely a problem of the filters in TIMMI2 and will be addressed in the future.

Moreover, it was noted that when using a re-imaging lens with focal length $f = 200\,mm$, the outer edge of the pupil was much less defocused. As a matter of fact, after checking again the distances of the components of the back-end optics of the setup, it was realised that few centimetres were missing in order to correctly focus the pupil image on the TIMMI2 focal plane. In order to limit the modifications to the setup, it was therefore decided to replace the $f = 250\,mm$ Ge lens with an $f = 200\,mm$ ZnSe lens. The components of the back-end part of the setup were then repositioned according to Figure 4.8, while the front-end part was modified as illustrated in Figure 4.21. It was also decided to reduce the diameter of the collimated beam to $10\,mm$ in order to reduce the risk of vignetting and possible residual aberrations. With this change, the beam focused on the coronagraphic image plane was reduce to $F_{\#} = 20$.

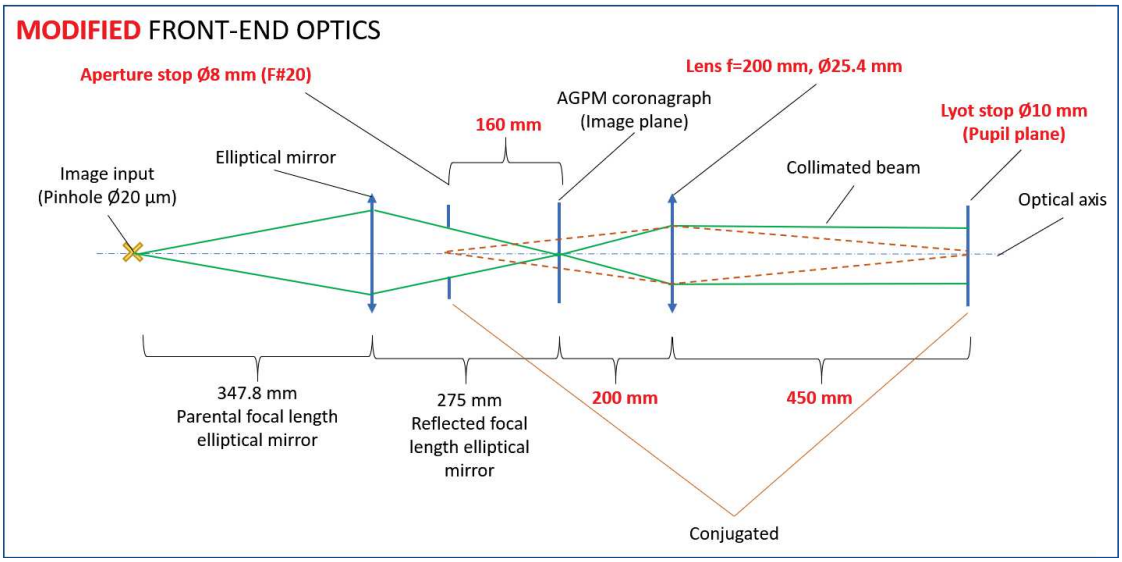

Figure 4.21: Modified front-end optics of the laboratory setup designed to test the AGPM coronagraph after the replacement of the re-imaging $f = 250\,mm$ Ge lens with an $f = 200\,mm$ ZnSe lens. In order to limit degrading effects due to aberrations and vignetting, the beam was reduced to an $F_{\#} = 20$. All the modifications done are indicated by red bold labels.

4.3. Alignment of AGPM coronagraph and Lyot stop

The AGPM was placed on an XY translation mount with differential drives which allowed fine positioning control of $0.5\,\mu m$ in order to minimise the flux level of the coronagraphic PSF, still maintaining a symmetric shape. These are two indicators of the fact that the AGPM is well centred [49]. Figure 4.22 illustrates non-coronagraphic and coronagraphic PSFs.

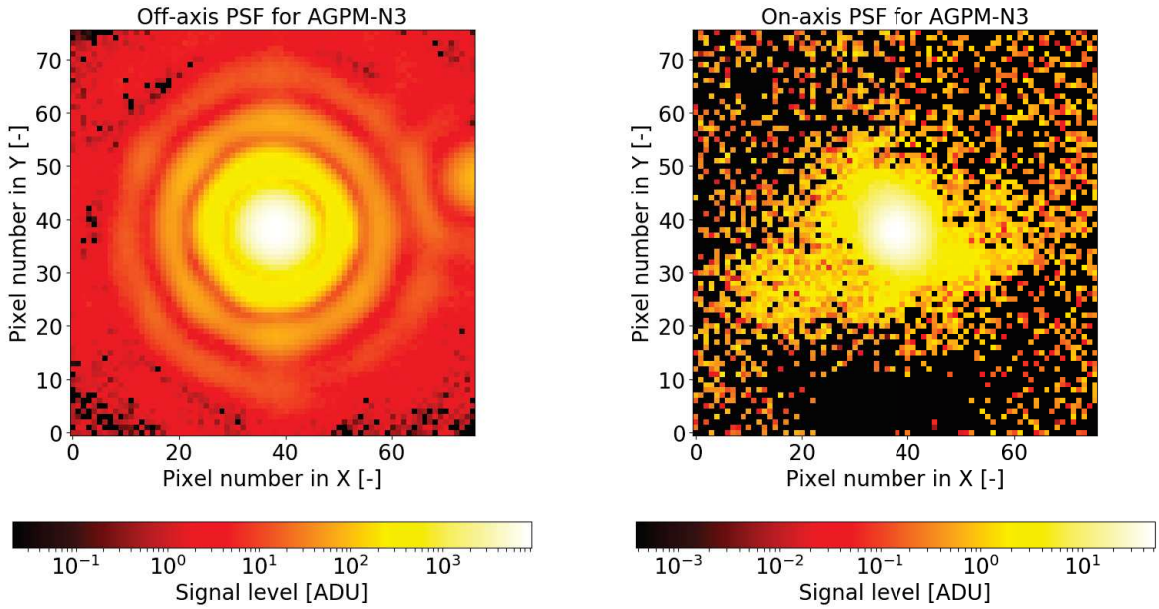

Figure 4.22: Left: PSF recorded at $10.220\,\mu m$ after decentring AGPM-N3 of $\sim 3\,mm$ ($> 10\lambda/D$). The second peak on the right side of the image is most likely a filter ghost in TIMMI2. Right: coronagraphic PSF recorded at $10.220\,\mu m$ with AGPM-N3, obtained by minimising the flux and keeping a symmetric circular shape.

The focus position along the Z axis was determined so that the flux level reaching the detector was minimised [49]. Figure 4.23 shows the pupil image for different positions of the AGPM along the optical axis. As it can be seen, leakages due to defocus errors exhibit with the shape of two lobes, which rotates of $\sim 90°$ depending on whether the AGPM is locate before or after the best focus position.

After minimising the intensity of the coronagraphic PSF, the setup was switched to the pupil imaging mode to centre the Lyot stop with the aperture stop. The Lyot stop was moved along the X and Y directions in order to obtain a symmetric coronagraphic pupil image, which, as already shown in Figure 4.2, has an annular shape. To do so, the diameter of the adjustable aperture stop was reduced to show the annular region and slowly increased again in order to reduce its thickness and allow the correct centring of the Lyot stop. Figure 4.24 shows a sequence of coronagraphic pupil images recorded during this procedure.

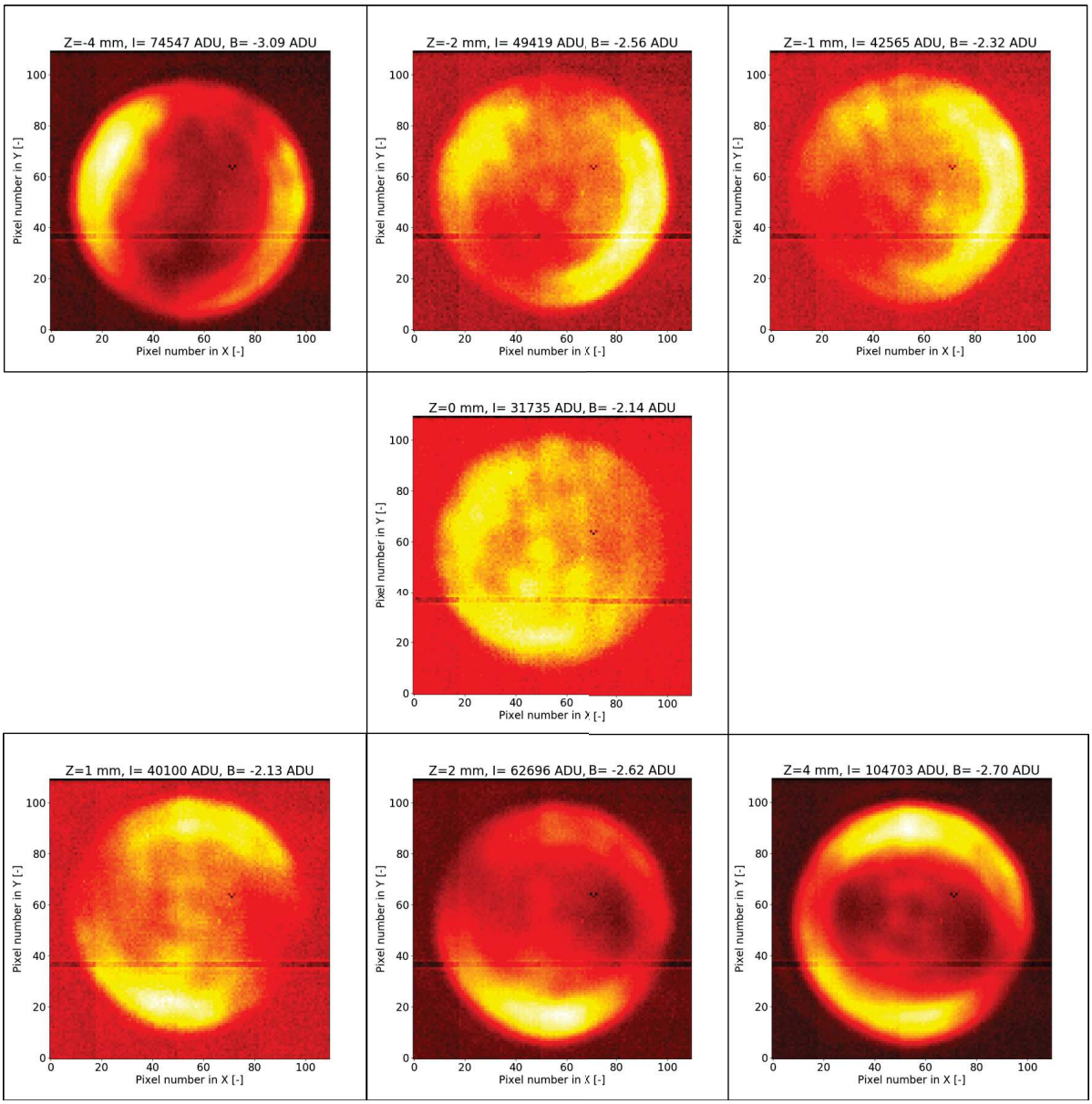

Figure 4.23: Pupil image for different axial position of AGPM-BT1. The image in the centre is the closest to the best focus, while top-left and bottom-right are respectively $4\,mm$ before and after it. Offset position with respect to the best focus (Z), residual total intensity of the pupil (I) and background level subtracted (B) are listed on top of each image.

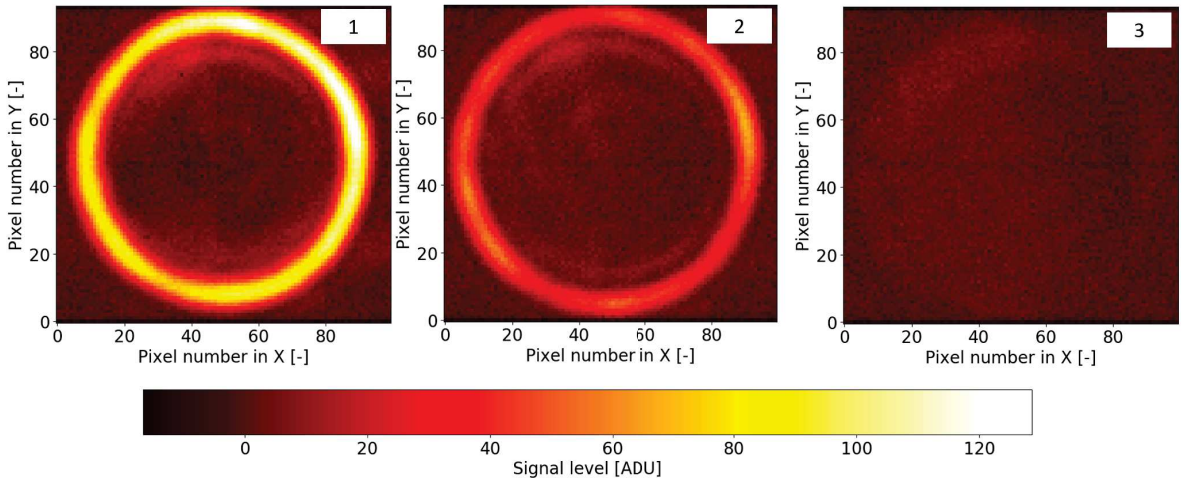

Figure 4.24: Sequence of coronagraphic pupil images recorded for AGPM-N3 during the centring of the Lyot stop with the aperture stop. Left: the aperture stop was reduced in size to clearly show the annular region. Centre: the aperture stop diameter was slowly increased again and the Lyot stop was adjusted in X and Y in order to obtain a symmetric image. Right: the aperture stop was further enlarged, and slightly oversized with respect to the 10 mm Lyot stop, to completely block the light of the annular region.

4.4. Test methodologies for the coronagraphic measurements

Before explaining the actual test procedure, it is noteworthy to emphasise that the CO_2 laser used as light source was affected by fast intensity variation of the order of few seconds in the worst cases, as shown in Figure 4.25. Because of that, it was not possible to record images with integration time longer than $\sim 10\,s$ in order to limit the influence of intensity fluctuations during each measurement. For the same reason, also the centring of the AGPM was not always a straightforward task, since the achievable minimum total intensity of the PSF core was in most of the cases changing from one measurement to the next one, all performed with the same conditions.

Another limiting factor encountered during tests was that the phase lock loop of the commercial mechanical chopper used was susceptible to glitches, which similarly did not allow for long integration time. This is again shown in Figure 4.25 at 10.551 and 10.675 μm in the two regions between 2.5 and 3.5 min, where both curves show a very steep variation caused by the phase shift. The phase stability was monitored with an oscilloscope, so that measurements with a wrong phase could be rejected. Indeed, a phase shift between the mechanical chopper and the detector readout controller implies a self-subtraction of the images containing the PSF, with a consequence reduction in the total flux integrated in the chopped image.

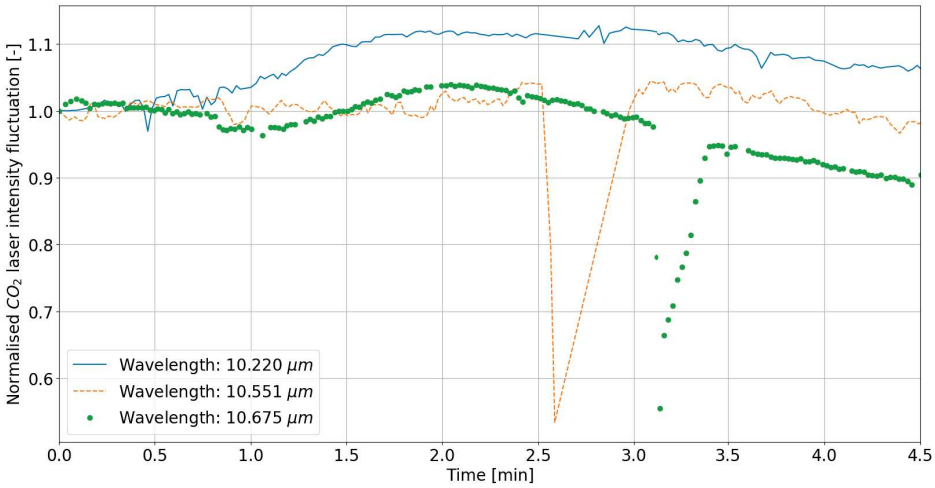

Figure 4.25: Fluctuation of the CO_2 laser intensity over a period of 4.5 min for three different wavelengths. The total intensity was calculated for pixels located within the FWHM of each PSF. Each curve was normalised with respect to the first measured value of the series. The two regions at 10.551 and 10.675 μm between 2.5 and 3.5 min where both curves shows a very steep variation are caused by the phase shift between the mechanical chopper and the detector readout controller.

4.4.1. Measurements of null depth and contrast profile

For each measurement, three different images were recorded. First, the AGPM was centred on-axis, following the procedure described in Section 4.3, and an image of the coronagraphic PSF, also referred to as on-axis PSF, was recorded. Second, the AGPM was shifted horizontally of about 3 mm ($> 10\lambda/D$) to record an image of the off-axis PSF, which is basically a non-coronagraphic PSF, which includes the effects of the propagation through the diamond substrate [49]. Figure 4.26 shows that for distances from the centre $> 3\lambda/D$, the AGPM does not have any attenuation effect on the PSF, except of course for the reduction due to the transmissivity of diamond. Third, the AGPM was removed and a PSF without coronagraph was recorded. Once again, the integration time of each separate frame was limited to $\sim 10\,s$ to contain the effects of the laser intensity fluctuation and phase shift between mechanical chopper and detector readout controller. It is also noteworthy that each of the frame recorded was already chopped for background removal.

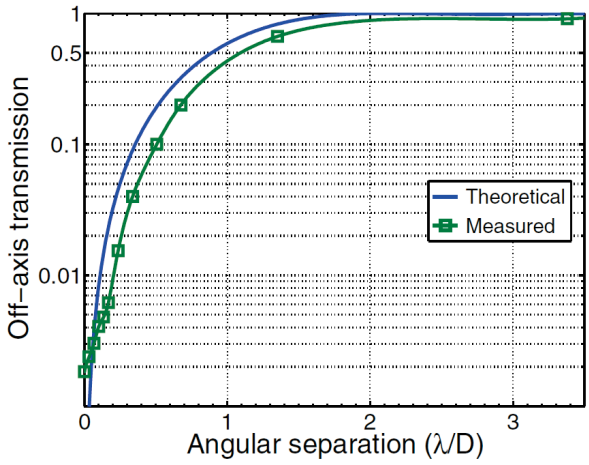

Figure 4.26: Theoretical and measured off-axis transmission of an AGPM as a function of the angular separation between the optical axis and the centre of an AGPM, expressed in units of λ/D [49].

4.4.2. Measurements of the transmission

The intensity fluctuation of the CO_2 laser did not allow to perform measurements of the AGPM transmission as a function of the angular separation similar to the one of Figure 4.26. Only off-axis measurements for decentring of the AGPM $> 5\lambda/D$ were recorded. Each of the AGPM was shifted laterally and two images of the PSF were recorded, one with the AGPM insert in the mount, and a second one without the AGPM. This procedure was repeated for four different directions, two horizontal (left and right) and two vertical (up and down).

4.5. Data analysis

4.5.1. Background substraction and determination of the PSF's centre

As already mentioned in Section 4.2, the test setup included a mechanical chopper to automatically subtract the background noise from the recorded images. Background residuals due to a non perfect match between the flux level of the mechanical chopper wheel and the one of the laboratory were then removed in post processing. The residual background level was estimated as the median value of the image, calculated excluding pixels whose intensity value was above 3σ, where σ is the standard deviation.

After that, the centre of each PSF was determined by fitting a two-dimensional Gaussian curve to the background corrected images. The centre calculated by the fitting was used as a reference for further analysis, like for example calculation of azimuthal median and FWHM. Before doing so, each of the PSF images was cropped around the centre calculated from the fitting, and all the frames for each category of measurements (on-axis, off-axis and without AGPM) recorded at the same wavelength were then stacked together in order to improve the S/N ratio.

4.5.2. Null depth

A robust metric to assess the performance of an AGPM in attenuating the intensity of the star's PSF is the null depth N_{AGPM}, defined as the ratio of the intensity of the coronagraphic PSF's core over the off-axis one [49]. This is expressed as

$$N_{AGPM} = \frac{\int_0^{FWHM} \int_0^{2\pi} I_{coro}(r,\theta)\, r\, dr\, d\theta}{\int_0^{FWHM} \int_0^{2\pi} I_{off}(r,\theta)\, r\, dr\, d\theta} \tag{4.1}$$

where I_{coro} and I_{off} are respectively the intensity of the coronagraphic and off-axis PSFs.

4.5.3. Contrast profile

The performance of an AGPM is also evaluated based on its ability to provide high contrast regions at small angular resolution from the PSF's peak. The contrast profile of the off-axis and on-axis PSF is calculated by normalising the azimuthal median of each PSF with respect to the peak value of the off-axis PSF. The azimuthal median is defined as the median intensity value of the pixels at the same radial distance from the PSF's centre. The contrast profile is then plotted as a function of the angular separation from the PSF's peak expressed in terms of λ/D values.

4.5.4. Off-axis transmission and stability of the CO_2 laser intensity

The transmission T_{AGPM} of each AGPM was calculated as the ratio of the total intensity in the off-axis PSF's core over the one of the PSF's recorded without the AGPM. This can be expressed, similar to Equation (4.1), as

$$T_{AGPM} = \frac{\int_0^{FWHM} \int_0^{2\pi} I_{off}(r,\theta)\, r\, dr\, d\theta}{\int_0^{FWHM} \int_0^{2\pi} I_{w/o\,AGPM}(r,\theta)\, r\, dr\, d\theta} \tag{4.2}$$

where I_{off} and $I_{w/o\,AGPM}$ are respectively the intensity of the off-axis PSF and of the one without the AGPM.

Besides providing information on the AGPM itself, the measured transmission allows also to keep track of the laser fluctuations during each measurement. Indeed, as already reported in Section 4.1, the expected transmission of the AGPM is at least $> 83\%$, which is the transmission of diamond at $\sim 10\,\mu m$, therefore values that significantly differ from it, or values larger than 100%, may be probably caused by fast variations of the laser intensity. Similarly, the total flux of the PSF's core recorded without the AGPM can be used to keep track of the laser intensity fluctuation from one measurement to the next one, in order to determine the intensity variation on a longer time scale.

4.6. Results of the tests for the coronagraphic measurements

The results of the tests performed to characterise the candidate AGPMs for the NEAR experiment are discussed in the next sections. Accoding to the requirements of the NEAR campaign, AGPM-BT1 and AGPM-BT2 shall provide a raw contrast level of 10^{-5} at $3\lambda/D$ and a null depth of 10^{-3}. When available, measurements of null depth and transmission are also compared with the expected values. AGPM-BT1, AGPM-BT2, and AGPM-N3 were tested at three different wavelengths of the CO_2 laser, which were mainly chosen depending on their intensity. Again, larger intensities of the laser were preferred in order to allow shorter integration time and limit the influence of intensity fluctuation and phase shift. For each component, during the coronagraphic measurements five sets of three frames (on-axis, off-axis and without AGPM) were recorded at each of the three tested wavelength, and as already described in Section 4.5.1, similar frames were reduced separately and then stacked together to improve the S/N. For all the measurements presented below, data for which the calculated transmissivity of the AGPMs resulted in values lower than 83%, the transmission of diamond at $\sim 10\,\mu m$, or larger than 100% were excluded since they were out of the physically acceptable boundaries, and therefore most probably caused by fast intensity fluctuations of the CO_2 laser. The results are presented depending on the wavelength at which they were recorded.

4.6.1. Overall results of the transmission measurements

As mentioned in Section 4.5.4, determining the transmission of the AGPMs can help to keep track of the laser fluctuation within each coronagraphic measurement. Table 4.2 reports the results obtained based on the test described in Section 4.4.2. For each AGPM, and at each wavelength tested, five sets of frames (off-axis and without AGPM) were recorded for each of the four directions along which the coronagraph was shifted (left-right and top-down). Figures 4.27 and 4.28 reports simulation of the expected value of the transmission respectively for AGPM-BT2 and AGPM-N3 at different wavelengths. As it can be noticed, the measured values are in accordance with the predicted results.

Table 4.2: Transmission of the three AGPMs at the different wavelengths tested. Results are expressed in terms of mean and one standard deviation value.

Transmissivity AGPMs			
	$10.220\,\mu m$	$10.551\,\mu m$	$10.675\,\mu m$
AGPM-BT1	91.90 ± 2.97	95.11 ± 3.19	93.48 ± 3.80
AGPM-BT2	92.75 ± 4.06	93.12 ± 1.81	92.93 ± 3.69
AGPM-N3	90.82 ± 3.89	93.39 ± 2.91	92.74 ± 3.78

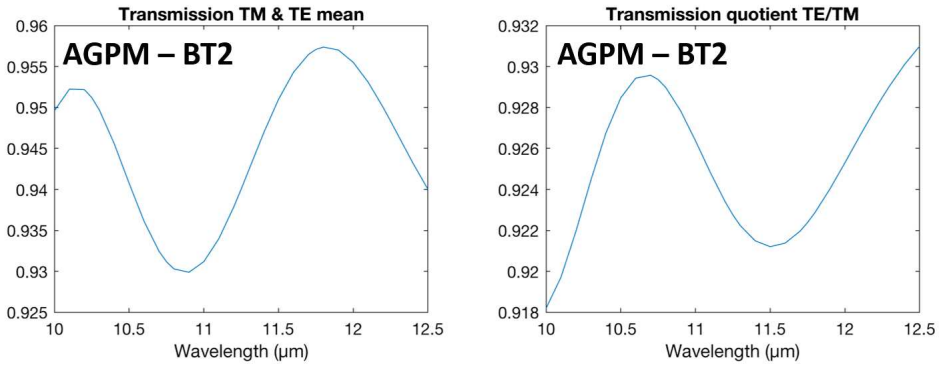

Figure 4.27: Theoretical transmission of AGPM-BT2 [simulation made by M. Karlsson, University of Uppsala].

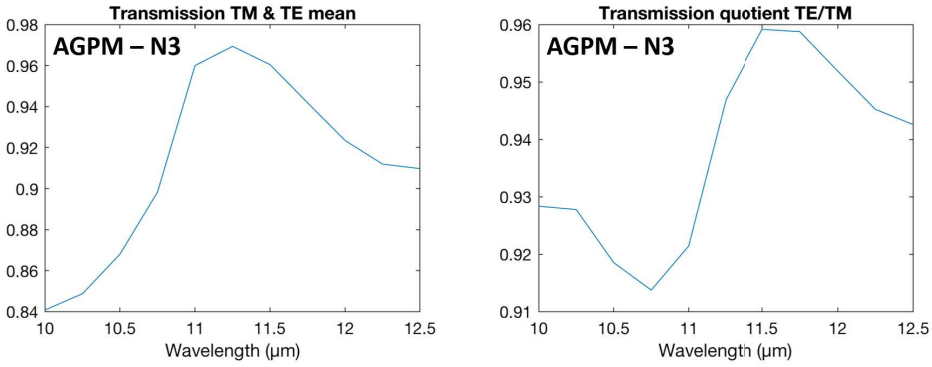

Figure 4.28: Theoretical transmission of AGPM-N3 [simulation made by M. Karlsson, University of Uppsala].

4.6.2. Results of the coronagraphic measurements

Figures 4.29, 4.30 and 4.31 summarise the results of the tests made to determine null depth and contrast profile of the three AGPMs, grouped based on the wavelength considered. Each figure contains three graphs of the contrast profiles, one for each coronagraph, and one graph that shows the variation of the laser intensity during the measurements considered. Details of each measurement are reported separately on top of each graph. Figures 4.32 and 4.33 compares the theoretical and measured values of the null depth respectively for AGPM-BT2 and AGPM-N3.

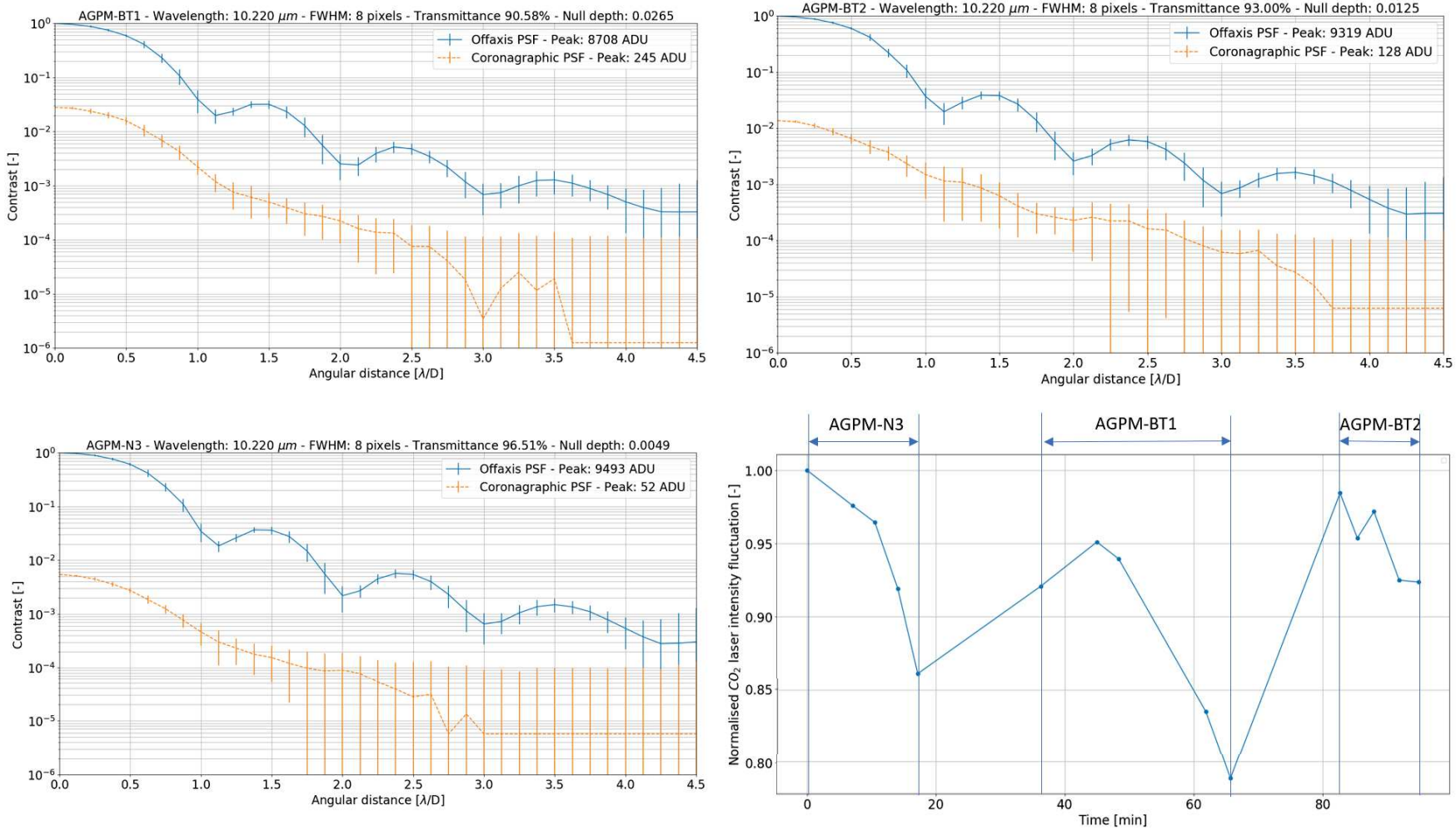

Figure 4.29: Coronagraphic performance of the three AGPMs measured at a wavelength of 10.220 μm. The error bars in the contrast profiles represent one standard deviation.

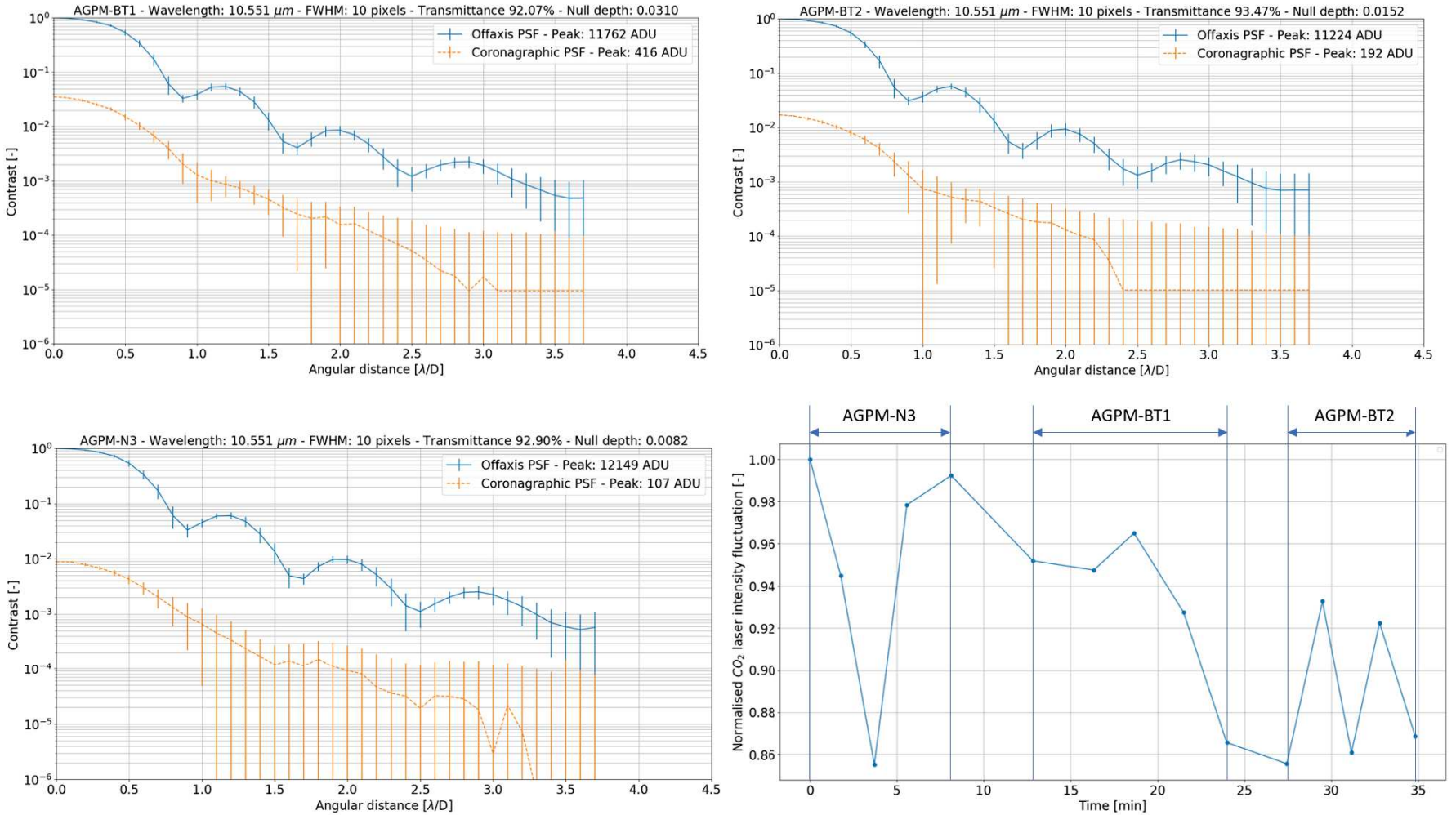

Figure 4.30: Coronagraphic performance of the three AGPMs measured at a wavelength of 10.551 μm. The error bars in the contrast profiles represent one standard deviation.

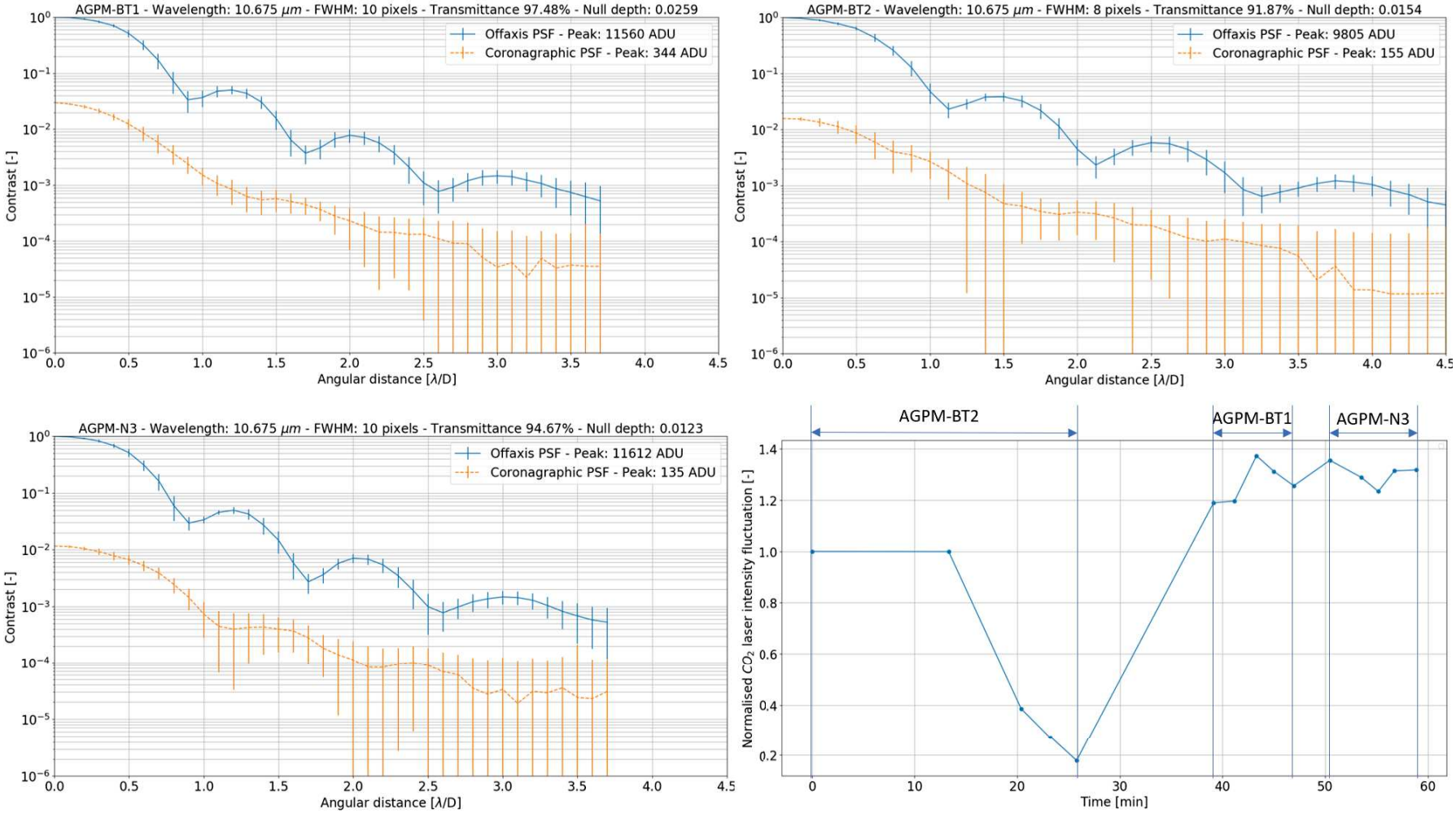

Figure 4.31: Coronagraphic performance of the three AGPMs measured at a wavelength of 10.675 μm. The error bars in the contrast profiles represent one standard deviation.

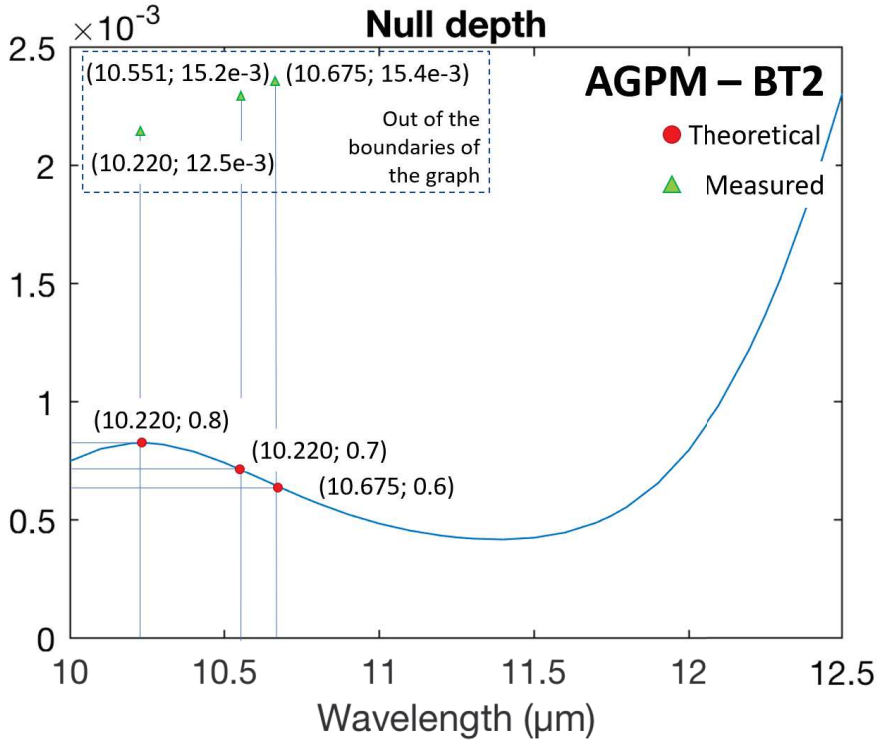

Figure 4.32: Comparison between the theoretical and measured null depth for AGPM-BT2 [theoretical values simulated by M. Karlsson, University of Uppsala].

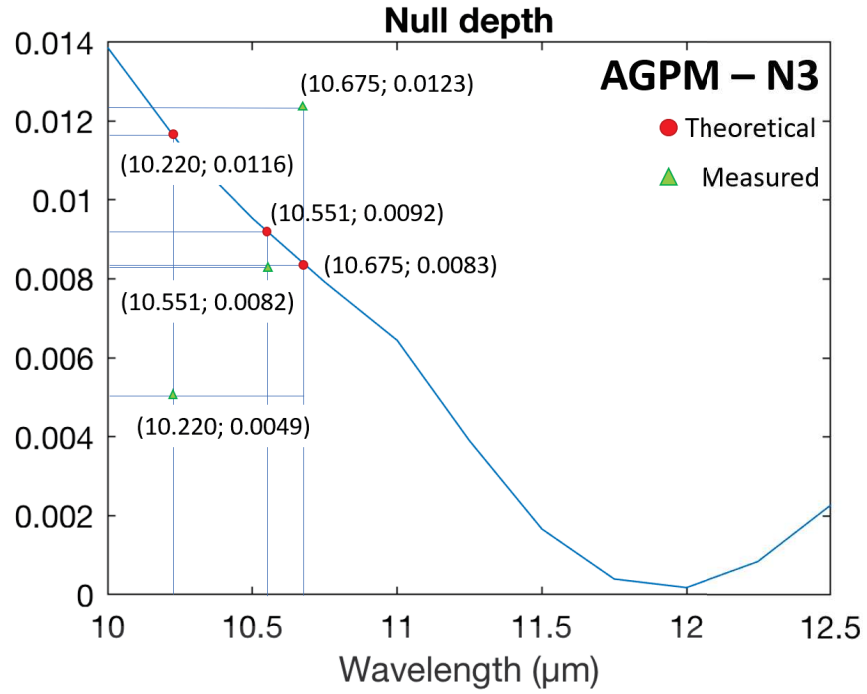

Figure 4.33: Comparison between the theoretical and measured null depth for AGPM-N3 [theoretical values simulated by M. Karlsson, University of Uppsala].

Before any consideration on the results reported in the figures above, it is noteworthy to draw the attention on the fluctuation of the laser intensity during each set of measurements. As it can be noticed, while at 10.220 and 10.551 μm the fluctuations were limited within 20% of the initial intensity, at 10.675 μm the intensity dropped of $\sim$ 80% in about ten minutes, making the measurements less reliable, and also the centring of the AGPM more difficult, since the minimum value achievable was constantly changing.

By simply looking at the peak rejection in the contrast profiles, it is immediately clear that AGPM-N3 has the best performance for all the three wavelengths tested, with values between 86 and 183. This is also confirmed when referring to the calculated values of the null depth, which at 10.551 μm is $4.9 \cdot 10^{-3}$, more than twice better than AGPM-BT2.

In terms of contrast level, from all the graphs it can be noticed that below 10^{-4} the uncertainties in the measurements, expressed in terms of one standard deviation value, increases as a consequence of the reduced S/N. However, even looking at values $> 10^{-4}$, AGPM-N3 again is the one that performs best at all wavelength.

Figures 4.32 and 4.33 reports a comparison between theoretical and measured value of the null depth for AGPM-BT2 and AGPM-N3. Two aspects shall be noticed. First, the measured values for AGPM-BT2 are above the limit reported in the graph, and indeed its performance is worse than expected, while for AGPM-N3 the measured values are in accordance with the predictions, at least in terms of order of magnitude. Second, for both cases the trend in the variation of null depth with the considered wavelength seems to be opposite with respect to the predicted one. Indeed, according to the theoretical prediction, between $\sim$ 10.2 and $\sim$ 10.7 μm the null depth shall decrease in value, and therefore get better, while according to the measurements the trend is opposite.

5

Summary and conclusions of the results of the laboratory tests

Final considerations on the validation of the Dicke-switch chopper system and characterisation of the AGPM coronagraph based on the laboratory tests discussed in this report are reported in this chapter.

5.1. Conclusions on the validation of the Dicke-switch chopper system

Chapter 3 discussed in details the complete laboratory characterisation of the Dicke-switch chopper system which will be implemented in VISIR as part of the NEAR experiment for background removal and suppression of the ELFN to achieve the sensitivity of $\sim 70\mu Jy$ ($5\,\sigma$/100h) required for the detection of potentially habitable planets in the Alpha centauri region.

The first part of the laboratory characterisation focused on the verification of the radiometric flux level achievable by the BBU of the VOU in order to match the background level typical at the VLT, where the combined sky and telescope thermal radiation is the same as the one of a greybody at $280\,K$ and 10% emissivity. Unfortunately, due space constraints in TIMMI2, it was not possible to cool down the BBU enough to reach the required radiometric level. Indeed, even though the temperature of the radiation shield of TIMMI2 is $90\,K$ when the VOU is mounted, the thermal bracket where the BBU is connected has a temperature $> 178K$, thus more than four times warmer then the cold shield of VISIR. However, since the reached flux level was marginally compliant with the required one, it was decided to avoid any main modification of the thermal interface between TIMMI2 and the VOU, which would have required a considerable effort for its implementation.

Besides of that, a second external blackbody to reproduce the background level typical at Paranal, also referred to as artificial sky, had to be characterised. This was done by placing a flat mirror in front of the field of TIMMI2, taking advantage of the fact that the instrument is cooled down at cryogenic temperature and is stable over long period of times. The flux level was increased in a controlled way by adding in front of the mirror a single or double layer of plastic foil. During this phase, it was noted that due to reflection of internal and external radiation the field seen by the detector when looking towards the artificial sky had intensity variation of $\sim$ 3.5%. After straylight analyses performed by KTO, the external contractor responsible for the design of the VOU, a new D-shape mirror was designed and manufactured to mitigate the parasitic light effects caused by reflection of the external radiation. Similarly, an additional baffle was mounted behind the dichroic window to block the radiation coming from the internal warm components of the VOU. The residual parasitic light has an intensity of $\sim$ 1%.

After the completion of the radiometric tests and the mitigation of parasitic light, the tests to valide the ability of the Dicke-switch chopper system to remove background level and suppress the ELFN started. A comparison between pseudo- and real chop measurements confirmed that indeed the Dicke-switch is able to mitigate the ELFN. A reduction $> 50\%$ was measured after increasing the chop frequency from ~ 1 to $\sim 10\,Hz$. Moreover, it was confirmed that the ELFN is suppressed also for large offsets between the flux level of BBU and artificial sky, up to at least $\sim 1600\,ADU$. This fact allows a relaxation in the time constant with which the BBU temperature has to be varied in order to match the background level.

Additional considerations on how representatives the tests and the results obtained with TIMMI2 are for VISIR are listed below:

- The defocus of the D-shape mirror with respect to the cold focal plane of TIMMI2 has no impact on the results, since the BBU produces only a flat field
- Simulations made by KTO showed that with the $F_{\#} = 13.4$ of VISIR the residual $\sim 1\%$ non flatness of the field measured with TIMMI2 at $F_{\#} = 35$ will be further diluted

Despite the successful validation of the Dicke-switch chopper system, its observing efficiency is limited only to 50%. For this reason, chopping with the secondary mirror of the UT4 remains the baseline for the observing campaign of the NEAR experiment. However, once that VISIR moves back to the UT3 the Dicke-switch chopper system will be regularly used for observations of extended objects, for which chopping with the secondary mirror is not feasible.

5.1.1. Future tests with the Dicke-switch chopper system

Radiometric tests and ELFN measurements were performed with the VOU not in its final configuration. Indeed, since at the time of the tests the new D-shape mirror designed to mitigate the parasitic light effects was not yet manufactured, a test part was implemented in the VOU. Since it was not gold coated, the produced background level was larger than expected, while the reflectivity was lower. However, it is expected that the results will not be affected significantly. Indeed, the ELFN increases with the intensity of the signal impinging on the detector, and therefore after the implementation of the final D-shape mirror the residual noise shall be even lower than the one measured with the test part. In any case, the tests will be repeated once that the final D-shape mirror is delivered to ESO, especially to measure the intensity of the residual parasitic light. If time allows, the tests will be also repeated after replacing the dichroic of the VOU with a flat window, as in the configuration that will be used after the observing campaign of the NEAR experiment when VISIR will be mounted back to the UT3.

5.2. Conclusions on the characterisation of the AGPM coronagraphs

The laboratory characterisation of the candidate AGPM coronagraphs for the NEAR experiment were extensively presented in Chapter 4.

First of all, the optical setup was carefully aligned, and the optical quality was measured both at optical and IR wavelengths. A CCD camera was placed at the level of the coranagraphic plane and illuminated with red optical light. The image recorded was a diffraction-limited PSF. At IR wavelengthts, the setup is characterised by a poor pupil image quality. After few additional tests it was concluded that the pupil image is degraded after the Lyot stop, and therefore the coronagraphic performance of the AGPM are not affected. This is most likely a problem with the filters of TIMMI2, and will be addressed in the future.

The results of the coronagrapic measurements revealed that both AGPM-BT1 and AGPM-BT2, whose designed was optimised for observations in the N-band, do not provide the required contrast of 10^{-5} at an angular separation of $3\lambda/D$, nor the predicted null depth of 10^{-3}. A comparison between the two shows that AGPM-BT2 performs better than AGPM-BT1, with a measured null depth twice better at 10.220 and 10.551 μm. Sample AGPM-N3 performs better than the other two coronagraphs at any of the three wavelengths tested, with a measured null depth of $4.9 \cdot 10^{-3}$ at $10.220\,\mu m$, twice as better as AGPM-BT2.

Unfortunately, the S/N ratio of the recorded data was not enough to measure contrast levels below 10^{-4} with a good confidence interval. However, when looking at an angular separation of $3\lambda/D$, none of the three coronagraphs seem to provide the required level of 10^{-5}. Nonetheless, according to the measurements the three AGPMs are marginally compliant with the requirement, in the sense that they provide a contrast level $< 10^{-4}$ at $3\lambda/D$. In future measurements, larger numbers of data set shall be recorded in order to improve the S/N ratio and achieve good confidence intervals below 10^{-4}.

The fact that AGPM-N3 performed better than AGPM-BT1 and AGPM-BT2 was quite an unexpected result for mainly two reason. First, the design of AGPM-N3 was optimised for observation between 11 and 13.1 μm, which is out of the range of the wavelengths tested. Second, it was manufactured in 2012, and at that time the manufacturing process was not as advanced as now, thus the optical quality is worse than AGPM-BT1 and AGPM-BT2.

After a long test campaign, all three components were sent back to the University of Uppsala for a visual inspection which aims at identifying the cause of the lower performance of AGPM-BT1 and AGPM-BT2. As of 28$^{\text{th}}$ November 2018, the investigation of the problem is still on going, and based on the tests performed, AGPM-N3 is the new baseline for the NEAR experiment, at least until further development. If the investigation does not reach any conclusion, during commissioning also the AGPM currently mounted in VISIR will be tested in order to compare its performance with AGPM-N3.

5.2.1. Future work on the laboratory setup for the coronagraphic measurements

Proposed improvements of the laboratory setup designed to test AGPM coronagraphs are listed below:

- Before being focused on the $20\,\mu m$ input pinhole, the IR beam of the CO_2 laser could be split and redirected to have a parallel path into TIMMI2 in order to constantly measure the intensity fluctuations
- Faster chop frequencies could stabilise the phase lock between the mechanical chopper wheel and the trigger signal provided by the pulse generator
- A motorised translation mount for the alignment of the AGPM would improve the positioning accuracy, and therefore also the repeatability of the measurements

Bibliography

[1] Breakthrough Initiatives. *Breakthrough Initiatives*. https://breakthroughinitiatives.org/. [accessed 2018-10-23].

[2] European Southern Observatory. *ESO at a glance*. https://www.eso.org/public/unitedkingdom/about-eso/esoglance/. [accessed 2017-11-07].

[3] European Southern Observatory. *VLT to Search for Planets in Alpha Centauri System (eso1702 - Organisation Release)*. https://www.eso.org/public/unitedkingdom/news/eso1702/. [accessed 2017-11-07].

[4] European Southern Observatory. *VISIR - VLT Imager and Spectrometer for mid Infrared*. https://www.eso.org/sci/facilities/paranal/instruments/visir.html. [accessed 2017-11-29].

[5] Kasper et al. NEAR: Low-mass Planets in α Cen with VISIR. *The Messenger*, 169:16–20, September 2017.

[6] M. Kasper and R. Arsenault. *VISIRAO Trade-off and Analysis Report*. European Southern Observatory.

[7] M.G. Stapelbroek et al. Origin of Excess Low Frequency Noise at Intermediate Infrared Backgrounds in BIB Detectors. *Proc. IRIS Detector*, (2), 1984.

[8] Breakthrough Initiatives. *Breakthrough Watch*. https://breakthroughinitiatives.org/initiative/4. [accessed 2018-12-02].

[9] M. Perryman. *The Exoplanet Handbook*. Cambridge University Press, 2011.

[10] National Aeronautics and Space Administration. *Exoplanet Exploration*. https://exoplanets.nasa.gov/. [accessed 2018-10-22].

[11] NASA Exoplanet Science Institute. *NASA Exoplanet Archive*. https://exoplanetarchive.ipac.caltech.edu. [accessed 2018-10-22].

[12] European Southern Observatory. *Exoplanets Press Kit*. https://www.eso.org/public/unitedkingdom/products/presskits/presskit_0005/. [accessed 2017-11-29].

[13] D.J. Des Marais et al. Remote Sensing of Planetary Properties and Biosignatures on Extrasolar Terrestrial Planets. *Astrobiology*, 2(2):153–181, 2002.

[14] S. Seager. Exoplanet Habitability. *Science*, 340:577–581, May 2013.

[15] National Aeronautics and Space Administration. *Exoplanet Exploration*. https://science.nasa.gov/about-us/smd-programs/ExEP. [accessed 2017-11-27].

[16] European Southern Observatory. *A Family Portrait of the Alpha Centauri System (eso0307 - Science Release)*. http://www.eso.org/public/unitedkingdom/news/eso0307/, March 2003. [accessed 2017-11-07].

[17] G. Anglada-Escudé et al. A Terrestrial Planet Candidate in a Temperate Orbit Around Proxima Centauri. *Nature*, 536:437–440, August 2016.

[18] European Southern Observatory. *ALMA Discovers Cold Dust Around Nearest Star (eso1735 - Science Release)*. https://www.eso.org/public/unitedkingdom/news/eso1735/, November 2017. [accessed 2017-11-07].

[19] K. Tristram et al. *Very Large Telescope - Paranal Science Operations - VISIR User Manual*. European Southern Observatory, September 2016.

[20] P.O. Lagage et al. The Final Design of VISIR: the Mid-Infrared Imager and Spectrometer for the VLT. In *Optical and IR Telescope Instrumentation and Detectors*, volume 4008. Proc.SPIE, 2000.

[21] P.O. Lagage et al. Successful Commissioning of VISIR: The Mid-Infrared VLT Instrument. *The Messenger*, 117:12–16, September 2004.

[22] European Southern Observatory. *Paranal Instruments Summary Table*. `https://www.eso.org/sci/facilities/paranal/cfp/cfp100/instrument_summary.html`. [accessed 2017-11-28].

[23] F. Kerber et al. Upgrade of VISIR the Mid-Infrared Instrument at the VLT. In *Ground-based and Airborne Instrumentation for Astronomy III*, volume 7735,77357R. Proc.SPIE, 2010.

[24] C. Marois et al. Angular Differential Imaging: a Powerful High-Contrast Imaging Technique. *The Astrophysical Journal*, 641:556–564, April 2006.

[25] D. Ives et al. AQUARIUS: the Next Generation Mid-IR Detector for Ground Based Astronomy, an update. In *High Energy, Optical, and Infrared Detectors for Astronomy VI*, volume 9154,91541J. Proc.SPIE, 2014.

[26] M. Downing et al. Detector Developments at ESO to Prepare for the E-ELT Era. In *High Energy, Optical, and Infrared Detectors for Astronomy VI*, volume 9154,915404. Proc.SPIE, 2014.

[27] K.R.W. Tristram. Challenges of Calibrations in the Mid-Infrared with VISIR. In *ESO Calibration Workshop: The Second Generation VLT Instruments and Friends*, 2017.

[28] S. Gutruf et al. *VISIR Flange Module - Design Description*. Kampf Telescope Optics, April 2017.

[29] A.J. Claret et al. Calibration of VISIR, the VLT Mid-Infrared Imager/Spectrometer. In *Instrument Design and Performance for Optical/Infrared Ground-based Telescopes*. Proc.SPIE, 2003.

[30] H.G. Reimann et al. TIMMI2: a New Multimode Mid-Infrared Instrument for the ESO 3.6-m Telescope. In *Optical and IR Telescope Instrumentation and Detectors*, volume 4008. Proc.SPIE, 2000.

[31] F. Kerber et al. VISIR Upgrade Overview and Status. In *Ground-based and Airborne Instrumentation for Astronomy V*, volume 9147,91470C. Proc.SPIE, 2014.

[32] G.H. Rieke. *Detection of Light: from the Ultraviolet to the Submillimeter*. Cambridge University Press, 2003.

[33] D. Ives et al. AQUARIUS: the Next Generation Mid-IR Detector for Ground Based Astronomy. In *High Energy, Optical, and Infrared Detectors for Astronomy V*, volume 8453,845312. Proc.SPIE, 2012.

[34] G.H. Rieke. Infrared Detector Arrays for Astronomy. *Annu. Rev. Astron. Astrophys.*, 45:77–115, 2007.

[35] B. Starr et al. RVS Large Format Arrays for Astronomy. In *High Energy, Optical, and Infrared Detectors for Astronomy VII*, volume 9915,99152X. Proc.SPIE, 2016.

[36] K. Volk. *Chopping and Nodding for Mid-Infrared Astronomy*. `http://www.gemini.edu/sciops/instruments/mir/chopnod.pdf`. [accessed 2017-12-01].

[37] European Southern Observatory. *The Secondary Mirror, M2 Unit*. `https://www.eso.org/sci/facilities/paranal/telescopes/ut/m2unit.html`. [accessed 2017-12-01].

[38] S. Heikamp et al. Drift Scanning Technique for Mid-Infrared Background Subtraction. In *Ground-based and Airborne Instrumentation for Astronomy V*, volume 9147,91479T. Proc.SPIE, 2014.

[39] W. Happer and J. Peebles. Robert Henry Dicke. *Physics Today*, 50(9):92–94, 1997.

[40] R.H. Dicke. The Measurement of Thermal Radiation at Microwave Frequencies. In *Classics in Radio Astronomy*, pages 106–113. Springer, 1946.

[41] D.F. Wait. The Sensitivity of the Dicke Radiometer. *Journal of Research of the National Bureau Standards*, 71C(2):127–152, 1967.

[42] D. Deming et al. Infrared Helioseismology: Detection of the Chromospheric Mode. *Nature*, 322(6076):232, 1986.

[43] D.A. Glenar et al. Infrared Heterodyne Spectroscopy: A Tool for Helioseismology. In *Advances in Helio-and Asteroseismology*, pages 481–484. Springer, 1988.

[44] S. Gutruf et al. *VISIR Flange Module - Compliance and Verification Matrix*. Kampf Telescope Optics, July 2017.

[45] C. Delacroix et al. A Diamond AGPM Coronagraph for VISIR. In *Ground-based and Airborne Instrumentation for Astronomy IV*, volume 8446'84468K. Proc.SPIE, 2012.

[46] B. Lyot. The Study of the Solar Corona and Prominences without Eclipses (George Darwin Lecture, 1939). *Monthly Notices of the Royal Astronomical Society*, 99:580, 1939.

[47] D. Mawet et al. Annular Groove Phase Mask Coronagraph. *The Astrophysical Journal*, 633:1191–1200, 2005.

[48] C. Delacroix et al. Annular Groove Phase Mask Coronagraph in Diamond for Mid-IR Wavelengths: Manufacturing Assessment and Performance Analysis. In *Space Telescopes and Instrumentation 2010: Optical, Infrared, and Millimeter Wave*, volume 7731,77314W. Proc.SPIE, 2010.

[49] C. Delacroix et al. Laboratory Demonstration of a Mid-Infrared AGPM Vector Vortex Coronagraph. *Astronomy & Astrophysics*, 553:A98, 2013.

[50] C. Delacroix et al. Design, Manufacturing, and Performance Analysis of Mid-Infrared Achromatic Half-Wave Plates with Diamond Subwavelength Gratings. *Applied optics*, 51(24):5897–5902, 2012.

[51] Access Laser. *L4 Family*. `https://www.accesslaser.com/portfolio/l4-family-2/`. [accessed 2018-12-05].

[52] C. Jenkins. Optical Vortex Coronagraphs on Ground-Based Telescopes. *Monthly Notices of the Royal Astronomical Society*, 384(2):515–524, 2008.